

Earth observation-driven analysis of flood extent in mangrove areas under tropical storms

MSc Thesis Hydraulic Engineering

J.M.R. van Aken

Earth observation-driven analysis of flood extent in mangrove areas under tropical storms

MSc Thesis Hydraulic Engineering

by

J.M.R. van Aken

to obtain the degree of Master of Science
at the Delft University of Technology

Supervisors:

Dr. Ir. S.G. Pearson
Dr. Ir. J. Timmermans
Ir. V.T.M. van Zelst
Ir. A. Cado van der Lelij

TU Delft
TU Delft
Deltares, TU Delft
Van Oord

Project Duration:
Faculty:

November, 2024 – May, 2025
Faculty of Civil Engineering and Geosciences, TU Delft

Cover: Environmental Monitor, Mangroves in Los Haitises National Park in the Dominican Republic.
(Credit: Anton Bielousov / CC BY-SA 3.0)

Preface

This thesis marks the final step of my Master's in Hydraulic Engineering and the completion of my journey through Civil Engineering at TU Delft. As a young girl walking through Madurodam, I was amazed by how it showcases what a small country can be great in: keeping dry feet below sea level. That moment sparked my passion for civil engineering, and looking back, I am proud of the path I have taken.

Throughout this process, I have grown both professionally and personally and feel privileged to have been a part of the field of hydraulic engineering. My interest in mangroves was sparked when visiting Demak, Indonesia, during the Hydraulic Study Tour in 2024. Seeing firsthand the role of mangroves in flood protection, their social and ecological value, and the urgency of alternative solutions, reinforced my belief that integrating nature into engineering is necessary in a world facing climate challenges.

I became fascinated by remote sensing during my bachelor thesis in Ghana, where I explored satellite imagery for monitoring water reservoirs. The ability to extract insights from satellite data, particularly in data-scarce regions, is something I find incredibly powerful. The combination of nature-based solutions and remote sensing is meaningful to me, it represents innovation and equity in engineering.

I am very grateful to those who have supported me along this journey. A special thanks to Amrit Cado van der Lelij for his enthusiasm and weekly guidance at Van Oord, as well as the Environmental Engineering team for making me feel welcome and opening my eyes to the possibilities in this field. I also sincerely thank my TU Delft supervisors: Stuart Pearson, Joris Timmermans, and Vincent van Zelst, for their expertise and encouragement throughout the research process. Their genuine passion for the subject made this process very enjoyable, something I truly appreciate.

Finally, I would like to thank my family and friends. My parents and brothers, for the brainstorming sessions at the kitchen table and for always believing in me. Willem, my housemates, and my study friends, for making this thesis journey fun, even during some stressful moments, and for even acting as my practice audience.

*J.M.R. van Aken
Delft, May 2025*

Abstract

Mangrove forests are coastal ecosystems that provide a wide range of ecosystem services. Among these, their role in coastal protection is especially relevant, as mangroves have the potential to reduce storm-driven flooding by slowing down surge, dissipating short-wave energy, and retaining water. With tropical storms intensifying due to climate change and mangrove ecosystems being increasingly under threat, understanding the capacity of mangroves to reduce flood extent under tropical storms has gained greater urgency. Yet, the complex interactions between ecological, geomorphological, and hydrodynamic variables that shape the capacity of mangroves to reduce flood extent make this difficult to assess. Hydrodynamic flood models face challenges in incorporating such complexity and are often constrained in their validation by the scarcity of observational flood data in tropical regions where mangroves are most prevalent. Remote sensing presents a promising yet underutilized opportunity to improve understanding of mangrove flood attenuation and support the validation of hydrodynamic models.

This research presents a novel approach consisting of (i) a conceptual guideline that structures the key variables influencing mangrove-induced flood attenuation and (ii) a remote sensing tool that maps flood extent using Sentinel-1 SAR C-band data in Google Earth Engine and visualizes relevant variables. Together, they form an approach that not only maps flood extent in mangrove areas following tropical storms, but also integrates key ecological, geomorphological, and hydrodynamic variables to contextualize the factors influencing flood attenuation by mangroves.

The approach was applied to a case study of Hurricane Irma (2017) in the mangrove region of the Everglades National Park, where the remote sensing tool detected a flood extent of 168,811 hectares, showing spatial resemblance to flood maps reported in literature. The flood detection model and its settings were refined through dry tests and a threshold sensitivity analysis. Applying the conceptual guideline to the case study area, guided by the outputs of the remote sensing tool, provided insights into elements affecting flood attenuation by mangroves in the region, including mangrove extent, storm track, precipitation, elevation, mangrove biomass and zonation, and channel patterns. Furthermore, comparing the flood extent derived from the remote sensing tool with that of a bathtub inundation model enabled the identification of a high-potential area where mangrove impact on flood extent appears most likely, providing a targeted basis for future research.

These results highlight the value of remote sensing as an accessible and globally applicable tool for generating flood extent maps and identifying areas with high potential for flood reduction by mangroves following tropical storms. The developed remote sensing tool represents a first step toward demonstrating how remote sensing can strengthen the validation of hydrodynamic flood models. Since such models can isolate the influence of mangroves on flooding, integrating remote sensing-derived flood extents as validation can enhance their accuracy and support future research into the flood attenuation capacity of mangroves. Ultimately, combined with the insights provided by the conceptual guideline, this can contribute to the wider goal of improving the understanding of the role of mangroves in coastal flood protection during tropical storms in the face of climate change.

Contents

Preface	i
Summary	ii
Nomenclature	v
1 Introduction	1
1.1 Research context	1
1.2 Problem description	1
1.3 Research gap	2
1.4 Research objectives	3
1.5 Research questions	3
1.6 Research structure	3
2 Theory	5
2.1 Mangroves	6
2.2 Tropical storms	8
2.3 Coastal flooding	10
2.3.1 Coastal flooding without mangroves	10
2.3.2 Coastal flooding with mangroves	12
2.4 Conceptual guideline	18
3 Method	20
3.1 Methodological requirements	21
3.1.1 User requirements	21
3.1.2 Technical requirements	21
3.2 Remote sensing tool	22
3.2.1 SAR Sentinel-1 C-band	22
3.2.2 Change detection	22
3.2.3 Google Earth Engine	23
3.2.4 Methodological framework	23
4 Case study	25
4.1 Study area: The Everglades National Park	26
4.2 Context: Hurricane Irma	28
4.3 Model testing and qualitative validation	29
4.3.1 Pre-storm time stack	29
4.3.2 Dry tests	30
4.3.3 Specific model settings	33
4.3.4 Qualitative validation	35
4.4 Application of conceptual guideline and remote sensing tool	38
4.4.1 Step 0: Flood extent	38
4.4.2 Step 1: Identification of the coastal type	39
4.4.3 Step 2: Determination of the dominant hydrodynamic forcing	39
4.4.4 Step 3A: Hydrodynamic variables	44
4.4.5 Step 4A: Ecological variables	44
4.4.6 Step 5A: Geomorphological variables	46
4.5 Case study interpretation	46
5 Discussion	49
5.1 Causal relation between flood extent and mangroves	50
5.1.1 Comparison SAR- and bathtub model flood	50

5.1.2	Control area	51
5.1.3	Integration with hydrodynamic models	51
5.2	Flood detection method	52
5.2.1	Satellite repeat cycle	52
5.2.2	Change detection limitations	52
5.2.3	Threshold sensitivity	52
5.2.4	Model choices	53
5.2.5	Validation	53
5.3	Conceptual guideline	53
5.3.1	Long-term impact of mangroves on flood extent	54
5.3.2	Wave set-up	54
5.3.3	Water storage function	54
5.3.4	Flood depth vs. flood extent	54
5.3.5	Interdependency between variables	55
5.4	Wider contribution	55
6	Conclusion	57
7	Recommendations	59
	References	63
A	Additional theory	72
A.1	Mangroves	72
A.1.1	Distribution	72
A.1.2	Classification	72
A.1.3	Ecosystem services	73
A.1.4	Threats	74
A.2	Tropical storms	75
A.2.1	Physical conditions	76
A.2.2	Classification of tropical storms	76
A.2.3	Consequences of tropical storms	77
A.2.4	Flood types	77
A.3	Coastal flooding	78
A.3.1	Coastal flooding without mangroves	78
A.3.2	Coastal flooding with mangroves	80
A.4	Variables included in conceptual guideline	84
A.5	Conceptual guideline	85
B	Additional remote sensing information	88
B.1	Optical remote sensing	88
B.2	Radar remote sensing	89
B.3	Sentinel-1 mission	90
B.4	Observable metrics of variables	91
B.5	Stepwise explanation of methodological flowchart	96
B.6	Earth Observation datasets in remote sensing tool	101
C	Additional case study data	102
C.1	Case study maps	102
C.2	Sentinel-1A SAR imagery footprints and information	105

Nomenclature

Abbreviations

Abbreviation	Definition
MSL	Mean Sea Level
SLR	Sea-Level Rise
TWL	Total Water Level
EO	Earth Observation
VV	Vertical transmit, Vertical receive (SAR polarization)
VH	Vertical transmit, Horizontal receive (SAR polarization)
GEE	Google Earth Engine
SAR	Synthetic Aperture Radar
InSAR	Interferometric Synthetic Aperture Radar
RI	Ratio Image
DEM	Digital Elevation Model
DTM	Digital Terrain Model
NDWI	Normalized Difference Water Index
MNDWI	Modified Normalized Difference Water Index
NDVI	Normalized Difference Vegetation Index
GRD	Ground Range Detected (Sentinel-1 product level)
AOI	Area of Interest
NLCD	National Land Cover Database
CHIRPS	Climate Hazards Group InfraRed Precipitation with Station data
SRTM	Shuttle Radar Topography Mission
IBTrACS	International Best Track Archive for Climate Stewardship
GMW	Global Mangrove Watch
WCA	Water Conservation Area
VIIRS	Visible Infrared Imaging Radiometer Suite
ABI	Advanced Baseline Imager
NOAA	National Oceanic and Atmospheric Administration
ESA	European Space Agency
USGS	United States Geological Survey

Symbols

Symbol	Definition	Unit
D	Diffusion coefficient	[m ² /s]
u	Horizontal velocity of wave-induced flow	[m/s]
H_{rms}	Root-mean-square wave height	[m]
H	Wave height	[m]
t	Time	[s]
x	Horizontal distance	[m]
g	Gravitational acceleration	[m/s ²]
k	Wave number	[rad/m]
h	Water depth	[m]
a_v	Vegetation frontal area density	[m ⁻¹]
C_c	Channel drag coefficient	[-]

Symbol	Definition	Unit
a_c	Vegetation frontal area density in channels	$[\text{m}^{-1}]$
C_v	Vegetation drag coefficient	$[-]$
D_s	Stem diameter	$[\text{m}]$
N	Number of stems per unit area	$[\text{m}^{-2}]$
$\left \frac{\partial \eta}{\partial x} \right $	Sea surface slope	$[-]$
ρ	Water density	$[\text{kg}/\text{m}^3]$
E	Wave energy	$[\text{J}/\text{m}^2]$
η	Water surface elevation	$[\text{m}]$
η_c	Channel water depth	$[\text{m}]$
η_v	Forest water depth	$[\text{m}]$
σ	Angular wave frequency	$[\text{rad}/\text{s}]$
ϵ_v	Vegetation-induced dissipation of wave energy	$[\text{W}/\text{m}^2]$
α	Relative height of the vegetation	$[-]$
C_D	Drag coefficient	$[-]$
b_v	Mangrove stem width	$[\text{m}]$
σ_{after}^0	Backscatter coefficient (post-flood image)	$[-]$
σ_{before}^0	Backscatter coefficient (pre-flood image)	$[-]$
RI	Ratio image of post- to pre-flood backscatter coefficient	$[-]$
T	Threshold for classifying flooded pixels	$[-]$

Introduction

1.1. Research context

Mangrove forests are coastal ecosystems located in tropical and subtropical regions, where they thrive in the intertidal zone between land and sea (Giri et al., 2011). Facilitated by their subaerial root systems, mangroves have the ability to dissipate wave energy and reduce storm surge, offering protective benefits to low-lying tropical coastlines (Sheng and Zou, 2017). In addition, mangroves provide a wide array of further ecosystem services, including carbon sequestration, serving as habitats for marine life, and providing timber for local communities (Sheng and Zou, 2017). They also hold cultural significance, supporting rituals and livelihoods throughout coastal societies (Ihinegbu et al., 2023).

The increasing pressure from anthropogenic activities, such as coastal population growth, agricultural expansion, and the exploitation of mangrove areas, is heightening the vulnerability to flooding of low-lying coastlines (Giri et al., 2011). With the rise in intensity of tropical storms, driven by global climate change, enhancing the understanding of flood hazard reduction by mangroves during extreme weather events has become increasingly urgent (Van Coppenolle et al., 2018). A more comprehensive evaluation of the role of mangroves in flood extent reduction under tropical storms is essential for their effective integration into adaptive flood management strategies (Gijsman et al., 2021).

1.2. Problem description

Despite the acknowledged importance of mangroves in coastal protection, there remains much uncertainty surrounding their contribution to flood extent reduction during extreme events (Gijsman et al., 2021, Krauss et al., 2009, Mclvor et al., 2015). During a tropical storm, not only short-period wind waves are generated but also longer-period waves, such as wave set-up and storm surges, emerge as important drivers to flood hazard. Gijsman et al. (2021) highlight that “although field evidence for the attenuation of shorter-period waves is increasing, field evidence is still limited for longer-period waves, such as infragravity waves. As a result, the functionality of mangroves during high-magnitude flood events is yet to be quantified.” (Gijsman et al., 2021, p.5). Mclvor et al. (2015) similarly conclude that “the understanding of the role of mangroves in mitigating the impacts of large storm surges remains incomplete” (Mclvor et al., 2015, p.424).

A contributing factor to this incomplete understanding is the complex interplay of variables that determine the effectiveness of mangroves in reducing flood extent in tropical storms. This is documented in several studies that highlight the different variables impacting the degree of flood attenuation by mangroves. To illustrate the broad range of variables involved; Quang Bao (2011) investigated the role of forest structure characteristics in flood reduction capacity through field observations. Similarly, Horstman et al. (2014) analyzed how wave attenuation rates vary with vegetation density. Additionally, Mazda et al. (2006) explored the impact of water depth and incoming wave height, and their interaction with mangrove roots, trunks, branches, and leaves, on attenuation rates. Consequently, unlike in traditional hard engineering approaches where clear failure thresholds can be established for coastal protection infrastructure, it is hard to predict the flood-reducing performance of mangroves under tropical storms, as their failure thresholds are much more variable and gradual due to this complex interplay of local ecological, hydrodynamic, and geomorphological variables involved (Gijsman et al., 2021). Therefore, the complexity arising from the many interacting variables that influence the flood attenuation capacity of mangroves makes it difficult to accurately quantify and analyze their role in providing flood protection during tropical storms.

Current research on flood attenuation by mangroves relies almost entirely on numerical modelling and a limited number of field observations (Horstman et al., 2014; Mclvor et al., 2012b). Numerical models are undoubtedly valuable, particularly because they enable the isolation of mangrove impact, thus allowing direct comparison between mangrove-present and mangrove-absent scenarios (Narayan et al., 2019; Zhang et al., 2012). Yet, the variety of factors involved in the attenuation process poses limitations for numerical hydrodynamic modelling, where mangroves are typically represented through a single, uniform roughness value throughout the forest extent. A major challenge is the validation of numerical models, as reliable field data is scarce and point-based, making it difficult to confidently assess the accuracy of the flood maps these models produce (Montgomery et al., 2019). Remarkably, only a few direct field measurements of storm surge attenuation by mangrove forests exists. Krauss et al. (2009) documented a water level reduction of 9.4 cm/km within a mangrove forest during Hurricane Wilma in 2005, in Everglades National Park, South Florida, USA. Zhang et al. (2012) emphasize that the absence of additional field-based evidence has contributed to the ongoing debate surrounding the coastal protection role of mangroves. Field measurements in mangrove forests during extreme weather events are often restrained due to the practical challenges of conducting on-site assessments (Horstman et al., 2014; Krauss et al., 2009). This is further emphasized by Mclvor et al. (2015), who highlight the scarcity of storm surge water level data in mangrove areas, largely due to the inherent difficulties of collecting measurements during storm conditions. This severe lack of validation data constrains the ability of numerical models to reflect reality and limits the further understanding of how mangroves may influence flood extent during tropical storms.

Remote sensing could offer a promising means to help address the research gap surrounding the role of mangroves in flood extent reduction under tropical storms in addition to current research efforts. Particularly, it holds potential to support the challenges of the lack of validation data for numerical models. Currently, the application of remote sensing to assess flood extent in mangrove areas affected by tropical storms remains underexplored. The role of remote sensing as a complementary method alongside numerical modelling and field observations in evaluating flood attenuation by mangroves has received limited attention in literature (Maurya et al., 2021; Yancho et al., 2020). This highlights the need to explore how to effectively leverage remote sensing to assess flood extent in mangrove regions and how it can strengthen existing approaches studying flood attenuation by mangroves under tropical storm conditions.

1.3. Research gap

Two key research gaps are identified. First, there is a theoretical gap concerning the lack of a synthesized understanding of the variables that influence flood extent reduction by mangrove forests during tropical storms. Existing knowledge on these factors remains fragmented across disciplines and literature, making it difficult to establish an integrated perspective. Second, there is a methodological gap regarding the potential contribution of remote sensing for detecting flood extent in mangrove areas and as a complementary tool to enhance existing numerical modelling studies that aim to assess the flood-reducing role of mangroves.

1.4. Research objectives

Research objectives

The objective of this research is to explore the added value of remote sensing for investigating flood extent reduction by mangroves following tropical storms, by mapping flood extent and visualizing identified key variables relevant to flood attenuation.

To achieve this, the research has the following deliverables:

- A **conceptual guideline** that structures the key variables influencing mangrove impact on flood extent, which helps to assess whether mangroves could potentially reduce flooding at a given coast.
- A **remote sensing tool** in Google Earth Engine (GEE) that uses open-source Sentinel-1 SAR data to map flood extent and visualize key variables in mangrove areas.
- The **application** of both the conceptual guideline and remote sensing tool to a case study of the Everglades National Park, South Florida, following Hurricane Irma.

1.5. Research questions

Research question

Main research question:

What can remote sensing contribute to the assessment of flood extent and the potential flood-reducing role of mangroves during tropical storms?

Subquestions:

1. Which geomorphological, ecological, and hydrodynamic variables impact the potential of mangroves to reduce flood extent following tropical storms?
2. How can remote sensing be used to detect flood extent in mangrove areas following tropical storms?
3. How can the approach, applied to the Everglades during Hurricane Irma, inform hydrodynamic models of flood extent and relevant variables in mangrove area under tropical storm conditions?

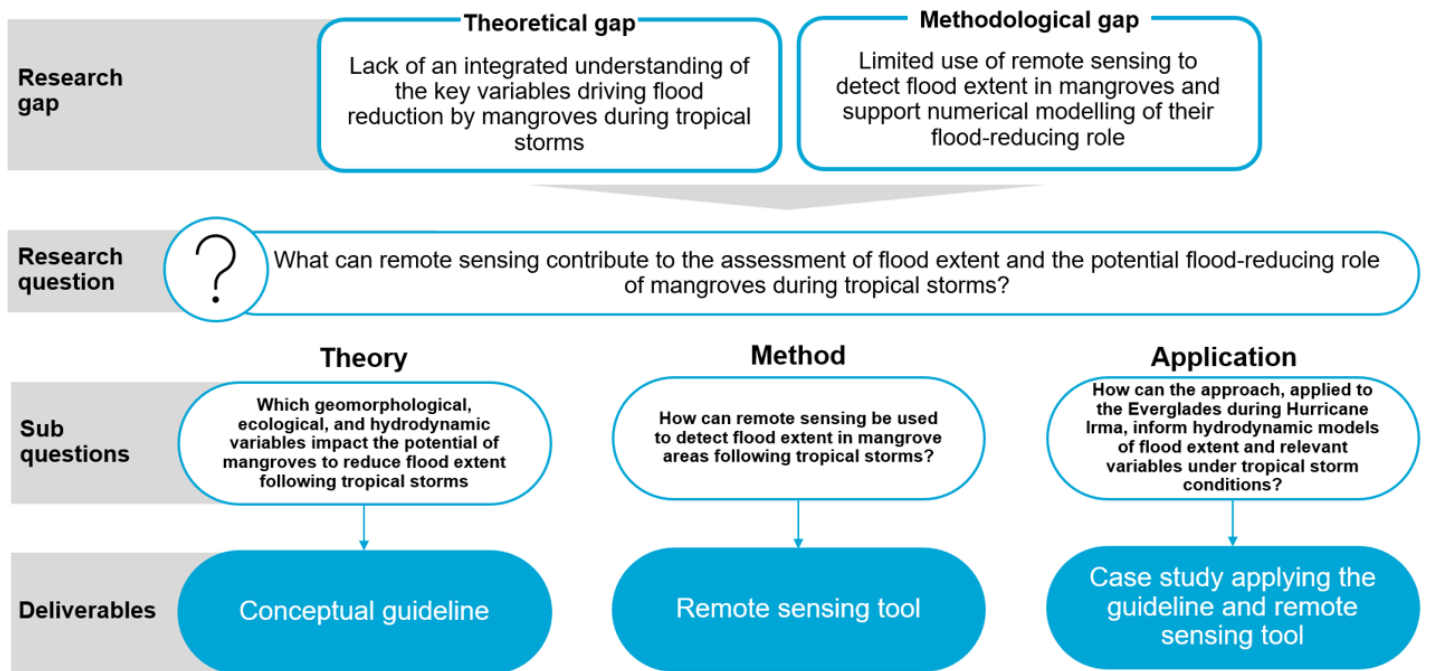
1.6. Research structure

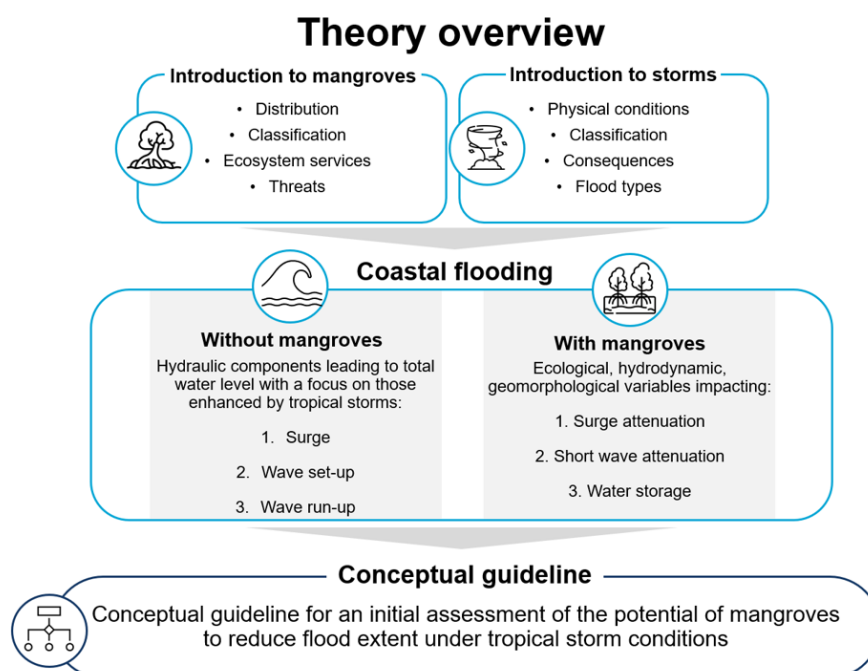
This research consists of three main components. First, a theory study is used to develop a conceptual guideline that structures the key variables influencing the potential of mangroves to reduce flood extent. This guideline synthesizes insights from existing studies across hydrodynamic, geomorphological, and ecological domains.

Second, a remote sensing-based method is introduced through the development of an open-source, user-friendly remote sensing tool in Google Earth Engine, aimed at detecting flood extent in mangrove regions following tropical storms. This tool leverages Sentinel-1 SAR data to allow for cloud-independent flood detection. Additionally, it integrates publicly available earth observation datasets to include variables identified in the conceptual guideline, thereby aiming to provide a more complete view of the factors at play.

Third, both the conceptual guideline and the remote sensing tool are brought together and applied in a case study focused on the mangrove region of the Everglades National Park, South Florida, during

Hurricane Irma (2017). In this case study, the remote sensing tool is tested, refined, and evaluated against existing flood extent data from the event. Simultaneously, the conceptual guideline is filled in using outputs from the tool, allowing for a structured assessment of the flood extent and the variables influencing it in the case study area.





The aim of this section is to develop a conceptual guideline to qualitatively assess mangrove flood attenuation potential during tropical storms. This is achieved through a theory study, which synthesizes current knowledge on the processes by which mangroves interact with flooding. This theory section begins with a general introduction on mangroves, followed by an introduction on tropical storms and the types of flooding they generate. Subsequently, it outlines the three primary mechanisms through which mangroves may affect flood extent: storm surge attenuation, short wave attenuation, and water storage. For each mechanism, the most relevant ecological, geomorphological, and hydrodynamic variables are identified and discussed. These variables form the basis for the guideline and for later exploration of their observability through remote sensing. This leads to an overview of the factors that determine the potential for flood attenuation in mangrove areas following tropical storms. To facilitate the practical application of these insights, a conceptual guideline is created, which classifies a mangrove site based on coastal type, dominant hydrodynamic forcing and then considers the identified key hydrodynamic, geomorphological, and ecological variables. It is intended to offer a qualitative, first-stage assessment of the potential of mangroves to reduce flood extent under tropical storm conditions. In doing so, it provides a structured foundation for decision-making before committing to more resource-intensive modelling or fieldwork.

Positioning this research within the existing literature, it is apparent that while mangrove-based flood attenuation has received considerable academic attention, much of the work remains rather fragmented in scope. Numerous studies have executed research on separate variables—for example, Quang Bao (2011) on forest width; Zhang et al. (2012) on forward storm speed; Montgomery et al. (2022) on the effects of channelization; Tanaka (2008) and Parvathy and Bhaskaran (2017) on coastal slope; Horstman

et al. (2014) on forest biomass and structural density; and Mazda et al. (2006) on the attenuation of short wave height. Broader initial overviews have been provided by McIvor et al. (2012b), who compile key mechanisms related to surge and wave attenuation. However, these efforts do not yet translate the collected insights into an integrated guideline that allows for intuitive assessment across different sites.

Moreover, several studies apply a single global attenuation rate for mangroves, like Van Coppenolle et al. (2018). However, mangrove flood attenuation is highly site-specific, influenced by hydrodynamic, geomorphological, and ecological variables that vary across regions. As a result, applying a uniform attenuation rate at all locations risks oversimplifying the dynamics of mangrove flood protection. Montgomery et al. (2019) highlights this concern by stating that “Without a clear theoretical framework, applying observed flood attenuation rates to other sites is problematic.” This research responds to this by synthesizing dispersed findings into a conceptual guideline, to support early-stage, qualitative evaluation of mangrove flood attenuation potential at a specific site, following tropical storms.

2.1. Mangroves

Mangroves are a unique group of salt-tolerant woody trees and shrubs that thrive in the intertidal zones along tropical and subtropical coastlines (Primavera et al., 2018, Das et al., 2022). Their networks of shrub and tree roots form thick barriers near the water line (Bosboom and Stive, 2023). Mangrove trees typically range from 2 to 8 meters in height, though certain environmental conditions can result in much taller trees (Bosboom and Stive, 2023). Mangroves possess distinct adaptations that enable them to survive in harsh environmental conditions, including waterlogged and anaerobic soils, high salinity, and fluctuating tides (Hamilton, 2020). These adaptations include physical mechanisms for coping with anaerobic soils, salt-exclusion abilities, and reproduction strategies which allow seedlings to establish in varying hydrodynamic environments (Hamilton, 2020). Beyond their resilience, mangroves belong to the most productive and ecologically important ecosystems on the planet (Hamilton, 2020). They play a crucial role in stabilizing shorelines, reducing the impact of natural disasters such as tropical storms, and providing essential services to humans and surrounding ecosystems (Giri et al., 2011; Spalding & Parrett, 2019).

Distribution

Mangroves can typically be found along coastlines, river deltas and estuaries between latitudes of 30° N and 30° S, with their distribution and diversity illustrated in Figure 2.1 (Primavera et al., 2018). These habitats are often located in sheltered environments, protected from strong winds and waves (Das et al., 2022). Mangroves flourish within intertidal environments, situated between mean sea level and high water (Giri et al., 2011). Further information on mangrove distribution is provided in subsection A.1.1.

Classification

Mangrove species have developed specific adaptations to cope with environmental stressors, leading to distinct species distributions across ecological settings (Das et al., 2022; Primavera et al., 2018). Common species include the red mangrove (*Rhizophora*) and the black mangrove (*Avicennia*), illustrated in Figure 2.2 (Duke et al., 2002; Romañach et al., 2018). These are primarily distinguished by their root structures: *Rhizophora* features prop roots—a dense, above-ground network—while *Avicennia* possesses pneumatophores, vertical, straw-like roots facilitating air exchange. Zonation of species varies by region: in the Indo-West Pacific, *Avicennia* often occupies the seaward edge, whereas in the Atlantic-East Pacific, *Rhizophora* typically acts as the pioneer species (Feller & Sitnik, 1996). Further classification details are provided in subsection A.1.2.

Another classification approach is based on coastal type, as proposed by Worthington, Zu Ermgassen, et al. (2020), who categorize mangroves according to their geomorphic setting. As shown in Figure 2.3, four main types are identified: *open coast*, *lagoonal coast*, *deltaic coast*, and *estuarine coast* (Worthington, Zu Ermgassen, et al., 2020). These coastal types differ in wave, river, and tidal influence, as well as their capacity to enhance storm surge. Further details on these coastal types are provided in subsection A.1.2.

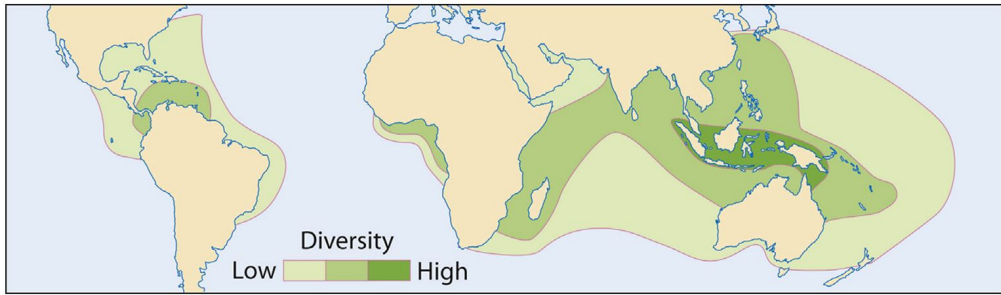


Figure 2.1: Distribution and diversity of mangroves species. The diversity scale is categorized as follows: low diversity includes 0 to 10 genera, medium diversity includes 10 to 25 genera, and high diversity refers to more than 50 genera (McIvor et al., 2015).

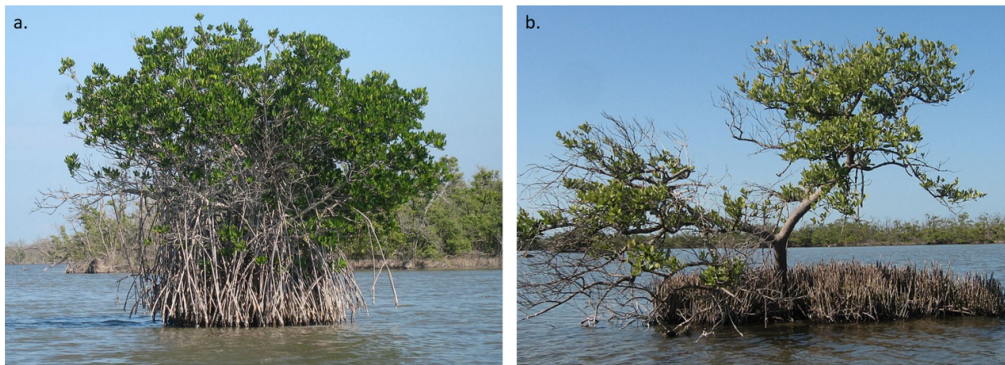


Figure 2.2: The red mangrove (*Rhizophora mangle*) (a) is recognized for its dense network of prop roots (Wikimedia Commons Andrew Tappert, 2007b). The black mangrove (*Avicennia germinans*) (b) is known for its pneumatophores, vertical, straw-like roots in the soil, allowing the tree to access oxygen in waterlogged environments (Wikimedia Commons Andrew Tappert, 2007a).

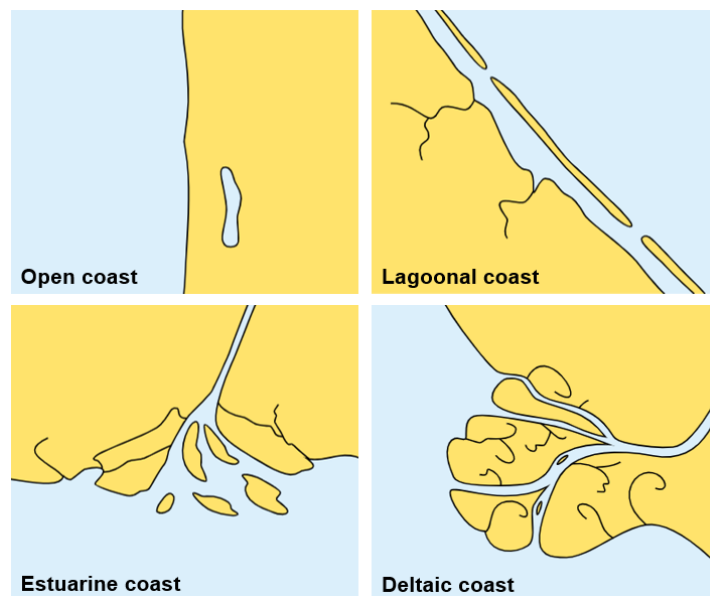


Figure 2.3: Four types of mangrove coasts as classified by Worthington, Zu Ermgassen, et al. (2020). Images from Bosboom and Stive (2023).

Ecosystem services

Mangroves provide a wide array of ecosystem services to both humans and the surrounding environment, as illustrated in Figure 2.4 (Hawkins, 2020). These services include *provisioning*, *regulating*,

supporting, and *cultural functions*. *Provisioning services* involve food and water resources, as mangroves serve as breeding grounds for fish, shrimp, and crabs (Spalding et al., 2014). They also supply dense timber that supports local economies (Spalding et al., 2014). *Regulating services* include coastal protection through wave and surge attenuation and sediment stabilization by root structures. *Supporting services* encompass water purification, as well as carbon sequestration; mangrove soils, being waterlogged and anaerobic, can store carbon up to four times more than terrestrial tropical forests (Spalding et al., 2014; Worthington, Andradi-Brown, et al., 2020). Lastly, *cultural services* include spiritual, recreational, and tourism values (Worthington, Andradi-Brown, et al., 2020). Further details are provided in subsection A.1.3.

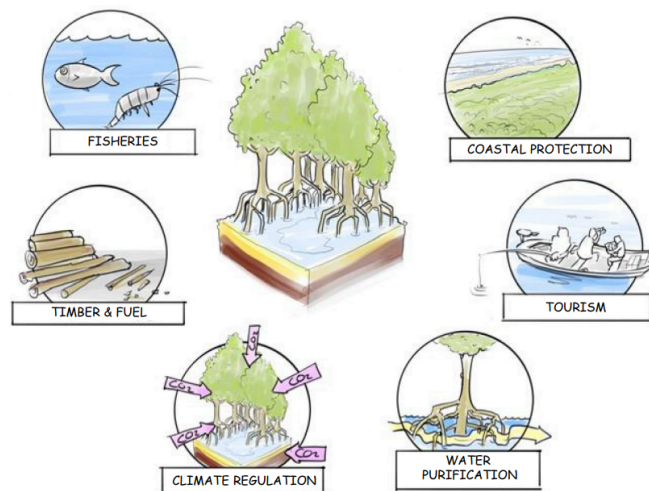


Figure 2.4: Ecosystem services provided by mangroves (Worthington, Andradi-Brown, et al., 2020).

Threats

Mangroves are increasingly threatened by both anthropogenic and natural drivers, accelerating their global degradation and increasing vulnerability to coastal erosion (Granek & Ruttenberg, 2007). Key threats include *land use change*, particularly the conversion of mangrove forests to aquaculture. In Southeast Asia and South America, over 50% of mangrove areas have been transformed into aquaculture ponds (Friess et al., 2019; Worthington & Spalding, 2014). Agricultural expansion and urbanization also contribute to deforestation (Worthington & Spalding, 2014). *Overexploitation* for timber and fuelwood further exacerbates degradation (Friess et al., 2019).

Climate change and *subsidence* present further threats. Sea level rise (SLR) can lead to permanent inundation, with its impact varying regionally depending on tidal dynamics (Parkinson & Wdowski, 2022). Climate change also intensifies tropical storms, which compound the effects of SLR and can also severely damage mangrove ecosystems (Van Coppenolle et al., 2018). Finally, subsidence contributes to relative sea level rise (RSLR), and while mangroves can adapt to this situation to some extent, their resilience depends on sediment availability—often limited in vulnerable regions (van Bijsterveldt et al., 2023). Further elaboration on the threats to mangroves can be found in subsection A.1.4.

2.2. Tropical storms

As this study examines the role of mangroves in reducing flood extent during extreme events, this section focuses on *tropical storms*, used here as an overarching term for extreme weather events occurring in tropical regions. These storms develop over warm ocean waters when rising warm, moist air creates a low-pressure center that draws in surrounding air, forming a rotating system with a calm center and intense surrounding cloud and wind activity (McIvor et al., 2015; Nelson, 2014).

The formation of a tropical storm requires the following key conditions: high ocean temperatures, warm moist air, low atmospheric pressure, and low vertical wind shear (UCAR, 2024). These conditions are generally present between latitudes 5° and 20°, where the Coriolis effect enables storm rotation (McIvor et al., 2012b). Storms evolve through several stages: from tropical disturbance to tropical depression,

then to tropical storm and finally to a hurricane. Once the storm makes landfall and loses access to ocean heat as main energy source, it weakens. A more detailed explanation of tropical storms is provided in section A.2. The naming of the strongest stage of tropical storms varies by region: they are called hurricanes in the Atlantic and Northern Pacific, typhoons in the Northwest Pacific, and cyclones in the South Pacific and Indian Ocean, as shown in Figure 2.5 (Fitzpatrick, 1999). Storm intensity is classified by maximum sustained wind speed, commonly using the Saffir-Simpson Hurricane Wind Scale, illustrated in Figure 2.6 (Mclvor et al., 2015; Smith & Montgomery, 2023).

Tropical storms cause damage through strong winds, rainfall, high water levels, and wave action (Nelson, 2014). Their impact on mangrove forests can be considerable, driven, among other factors, by prolonged water ponding (Krauss & Osland, 2019; Mo et al., 2023). Although mangroves have the capacity to recover, intense tropical storms can cause tree mortality and forest degradation (Krauss & Osland, 2019). In addition, storms disrupt natural processes like seed dispersal and sediment transport, altering the long-term composition of mangrove forests. As mentioned, tropical storms can enhance winds, rainfall, waves, and storm surges. These drivers can lead to different types of floods: *coastal flooding* caused by storm surges and short waves, *pluvial flooding* due to heavy rainfall, and *fluvial flooding* from river overflow (Nasr et al., 2021). When two or more of the flood types occur at the same time it is referred to as compound flooding, as shown in Figure 2.7 (Eilander et al., 2023). As researched by Pelckmans et al. (2024), mangroves primarily influence coastal flooding, while their role in mitigating fluvial or pluvial flooding remaining limited (Pelckmans et al., 2024). Therefore, the following sections focus specifically on coastal flooding, beginning with a scenario without mangroves, followed by one that includes mangrove presence.

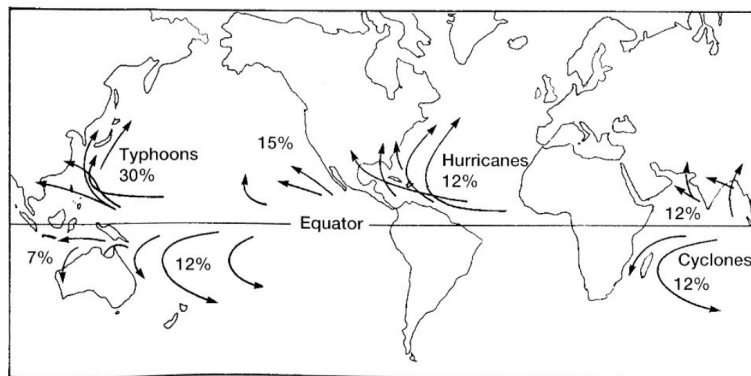


Figure 2.5: Global distribution of tropical storms and their local names. The map highlights the percentage of tropical storms in the different regions (Fritz and Blount, 2007).

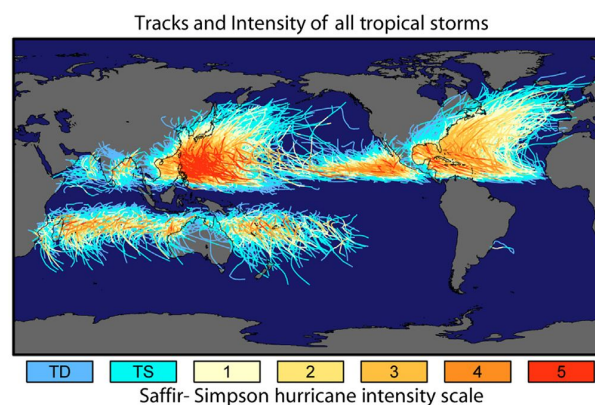


Figure 2.6: Pathways of tropical storms between 1985 and 2005, colour-coded according to their intensity on the Saffir-Simpson Hurricane Wind Scale. TD and TS stand for tropical depression and tropical storm respectively (Mclvor et al., 2015).

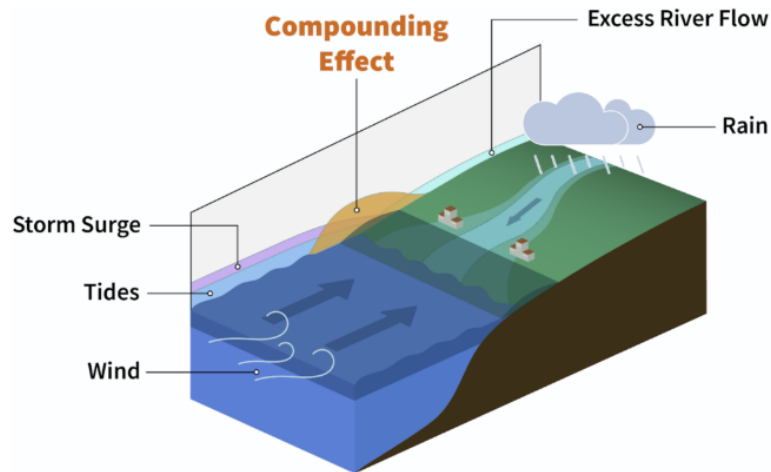


Figure 2.7: Compound flooding: river overflow (fluvial), heavy rainfall and runoff (pluvial), and storm surge (coastal) leading to flooding together in coastal areas. (Cascadia CoPes Hub, 2024)

2.3. Coastal flooding

2.3.1. Coastal flooding without mangroves

In the absence of mangroves, the individual hydrodynamic elements contributing to the total water level (TWL) are sea level rise, seasonal anomalies, tide, surge, wave set-up and wave run-up, as shown in Figure 2.8. An examination of storm surge, wave set-up and wave run-up will be provided, as these are specifically enhanced by tropical storms in mangrove area. The other hydraulic elements are elaborated on in subsection A.3.1.

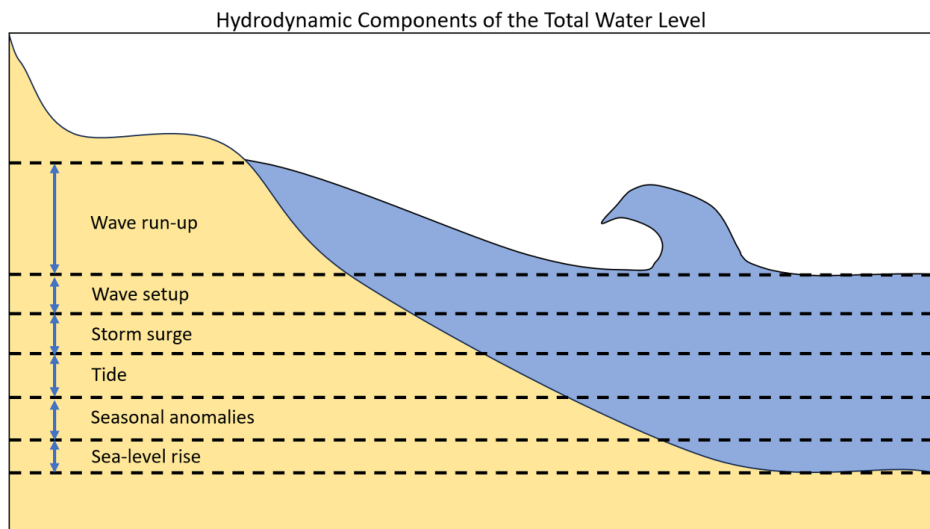


Figure 2.8: Illustration of the hydraulic components contributing to the TWL, which can lead to the flood extent (Image based on Vitousek et al., 2017).

Storm surge

Storm surge is enhanced during tropical storms and alter the TWL along the coast (Bosboom and Stive, 2023). As McIvor et al. (2012b) describes, “Storm surges may be defined as abnormally high sea water levels in coastal areas caused by a short-lived atmospheric disturbance such as a hurricane or storm” (McIvor et al., 2012b, p7). Storm surges are long-period phenomena, with a duration of a few hours to half a day, caused by the combined effects of the transfer of momentum from winds onto the water, low atmospheric pressure, and interactions with the coastal landscape, as shown in Figure 2.9 (Temmerman et al., 2022). Storm surge events can be classified by their surge height, defined as the

difference between the observed water level during the event and the expected tidal water level in the absence of the surge (Mclvor et al., 2012b).

Storm surge can have devastating consequences, causing flooding in communities, urban areas, agricultural and industrial lands, as well as natural ecosystems (Mclvor et al., 2012b; von Storch & Woth, 2008). Storm surges are regarded as one of the most catastrophic natural disasters, both in terms of fatalities and financial impacts (Needham & Keim, 2011). Regarding tidal range, surge can have a particularly great impact on microtidal coasts, where natural tidal variations are minimal (Mclvor et al., 2015). When storm surges, even relatively mild ones, occur at the same time as high spring tides, the combined effect can lead to notably elevated water levels, amplifying the potential for severe coastal flooding (Mclvor et al., 2012b).

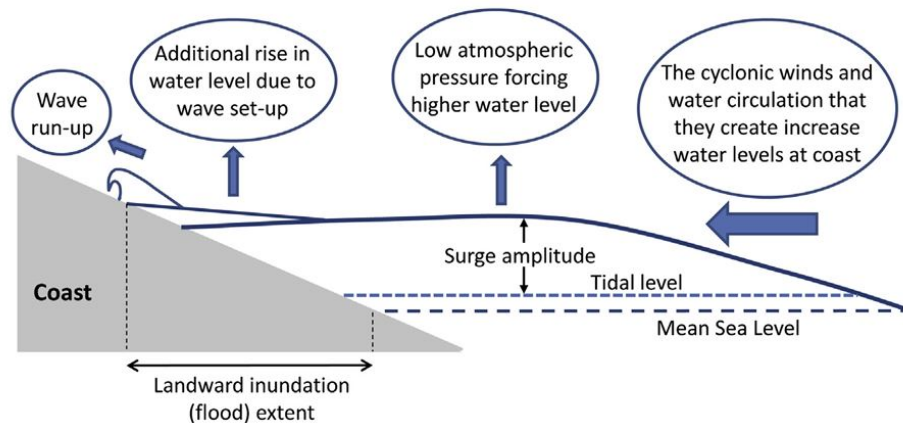


Figure 2.9: Illustration of storm surge dynamics, showing the combined effects of storm surge topped by wave run-up and wave set-up, contributing to an elevated water level at the coast (Mclvor et al., 2015).

To describe the different processes leading up to storm surge more clearly, a stepwise explanation is provided, consisting of two main elements: the effects of pressure and wind (Harris, 1963).

1. Pressure effect

Ocean water, when unrestricted in its flow direction, rises in regions of low atmospheric pressure and drops in areas of high atmospheric pressure (Harris, 1963). A 1 cm difference in water level corresponds to a 1 millibar drop in atmospheric pressure, working towards an equilibrium (Harris, 1963). In extreme cases, this pressure-induced water level increase can reach up to 1 m (Mclvor et al., 2012b). Offshore, this effect is most important as the flow moves toward the low-pressure area of a tropical storm in deeper water. However, as the surge approaches shallower coastal areas, wind effects become more dominant, and the role of atmospheric pressure in determining surge height diminishes (Friebel, 2016).

2. Wind effect

As the storm surge moves from offshore towards shallower water depths, the primary contributor to the surge becomes the wind, which pushes water toward the coast in the direction of the storm's track (Friebel, 2016). This wind stress on the water surface is shown in Figure A.3. The effect is strongest in shallow water, where it generates a gradient in water level elevation (Flather, 2001; Mclvor et al., 2012b). Wind stress is proportional to wind speed and storm size, but larger storms do not automatically result in greater surges due to other influencing factors like bathymetry and coastal topography (Mclvor et al., 2012b; Needham & Keim, 2011).

Wave set-up

Wave set-up is a long-wave phenomenon that contributes to the total water level (TWL), quite similar to surge. It originates from the breaking of short waves (wind and swell waves) and results in a sustained increase in the water level near the shore.

Wind and swell waves are generated by the wind exerting stress on the water surface. Generally, wind waves have shorter wave periods and wavelengths compared to swell waves. Wind waves are defined

as “relatively short, random, and irregular oscillations of the water surface” (Bosboom & Stive, 2023). In contrast, swell waves propagate over vast distances before arriving at the coast. As a result, they exhibit a much more regular and uniform pattern compared to the randomly distributed wind waves generated more locally. Swell waves originate from wind waves through the process of dispersion (Bosboom and Stive, 2023). While both types of waves represent surface fluctuations around the mean water level, they do not directly contribute to TWL. Instead, their influence becomes relevant when they break and wave energy is dissipated near the coast. The energy of a wave per unit area, E , is given by the expression $E = \frac{1}{8}\rho gH^2$, where ρ denotes the water density [kg/m^3], g is the gravitational acceleration [m/s^2], and H represents the wave height [m]. This relationship shows that wave energy per unit area is proportional to the square of the wave height (Mclvor et al., 2012a).

As waves approach the coast and enter shallower water, they begin to interact with the seabed and start shoaling, meaning that the wave height increases while the wavelength reduces, steepening the waves. The wave steepness, defined as the ratio of wave height H to wavelength L , as further shown in Figure A.4, determines the point at which waves eventually break (Bosboom & Stive, 2023). Taking into account the conservation of energy flux, the increase in wave height and consequently wave energy during shoaling, followed by a decrease in wave height and energy as waves break in the surf zone, results in a gradient in radiation stresses (Van Rooijen et al., 2016). As wave momentum is transferred to the water column, this gradient in radiation stress, when divided by the local water depth, applies a horizontal force on the water column (Van Rooijen et al., 2016). This force is compensated by a pressure gradient and bed shear stress (Van Rooijen et al., 2016). The pressure gradient means a rise in the water level at the coast, known as wave set-up. It can be understood as a temporary elevation of the water surface induced by wave breaking, as further illustrated in Figure A.5. According to Mclvor et al. (2012b), wave set-up may contribute 30–60% of the total storm surge height during tropical storm events, making it a substantial component of total water level (TWL) under storm conditions.

Wave run-up

As previously mentioned, short waves themselves do not directly contribute to the TWL. However, once these waves break, the resulting processes do influence TWL and flood extent. Besides the discussed wave set-up, wave run-up is relevant. Wave run-up refers to the uprush of water at the coastline, “the final flow of water from breaking waves”, as Mclvor et al. (2012b) describes, where the last remains of wave energy dissipate due to gravity and friction. This process plays a role in how far water can travel inland, which can impact overtopping and flood extent. According to Friebel (2016), short waves superimposed on storm surge are especially relevant to coastal flood damage, as their damaging energy can extend further inland.

2.3.2. Coastal flooding with mangroves

Mangrove forests can play a role in reducing coastal flood extent following tropical storms through three primary mechanisms. First, they can slow down the propagation speed of storm surges. Second, is their ability to attenuate short waves, which can travel on top of the storm surge, as illustrated in Figure 2.10. Lastly, mangroves can mitigate flood extent by providing a water storage function, acting much like a sponge. By retaining water, the mangrove forest can simply reduce the volume of water that flows towards inland areas, thereby offering protection from coastal flooding. The effect of mangroves on storm surge is often limited, primarily due to the large forest widths required for substantial attenuation (Gijón Mancheño et al., 2022). In contrast, their impact on short wave energy is more pronounced. Yet, Van Rooijen et al. (2016) highlight that breaking short waves generate wave set-up, which in turn is a long-wave phenomenon similar to storm surge. Therefore, also in the absence of storm surge, when set-up is generated by breaking waves before having entered the mangrove forest, the mangroves must still attenuate these long-wave phenomena resulting from wave set-up.

This section provides a further examination of these three mechanisms and evaluates the key variables influencing the effectiveness of mangroves in flood mitigation. These factors include geomorphological, ecological, and hydrodynamic variables. These variables will also serve as inputs for the conceptual guideline and the remote sensing tool in following chapters.

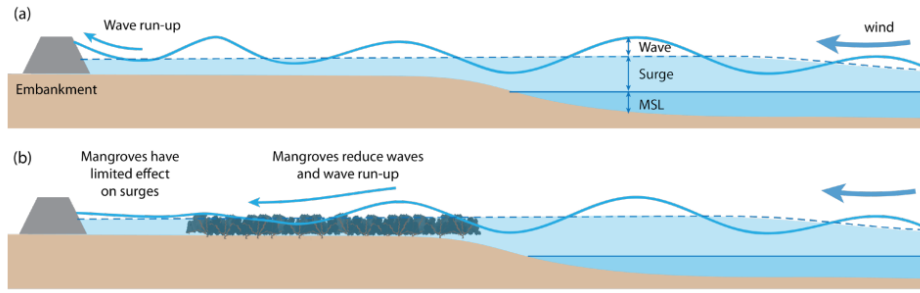


Figure 2.10: Illustration of the interaction between mangroves and surge and short waves (Gijón Mancheño et al., 2022). (a) Depicts water level in the absence of mangroves, where storm surge and waves propagate freely. (b) Demonstrates the effect of mangroves, which primarily reduce short wave energy, while mangroves have generally have lower effect on surge attenuation. Additionally, mangroves can contribute to flood mitigation through a water storage mechanism.

Mangrove impact 1: Surge attenuation

The influence of mangroves on storm surge attenuation remains a topic of ongoing research, with observational studies showing considerable variability, ranging from 0 to 50 cm surge height reduction per kilometer of mangrove forest (Montgomery et al., 2022). Large widths of mangrove forests are typically required for meaningful surge attenuation; field observations in the Everglades National Park in Florida by Krauss et al. (2009) determined that a minimal forest width of 12-20 km is necessary for reducing a surge height of 3-5 meters.

The need for extensive mangrove forest widths to achieve surge attenuation stems from the long-wave character of surge, forming over spatial scales of several hundred kilometers (Gijón Mancheño et al., 2021, 2022). Mangrove forests impose friction on these long surge waves, reducing their propagation speed. This, in turn, limits water exchange through the forest, thereby decreasing flood depth and, consequently, flood extent (Temmerman et al., 2022). By simplifying the conservation equations for mass and momentum, this system can be reduced to a diffusion equation, which can be used in this context to represent how surge flows through a mangrove forest (Montgomery et al., 2022). This diffusion equation describes the spatial and temporal spreading of the elevated water level, which is influenced by frictional forces applied by the mangrove forest (Montgomery et al., 2022).

The friction introduced by the mangroves reduce the diffusion coefficient, thereby restricting the spread of the elevated water level and the inland transfer of water. This results in reduced flooding. However, when channels are present, the diffusion process is no longer primarily governed by the frictional resistance of the mangroves, but rather by the physical characteristics of the channels themselves—such as channel depth. These features facilitate greater water transfer, diminishing the attenuation capacity of mangroves and leading to increased inland flooding (Montgomery et al., 2022). The diffusion equation is expressed as follows (Montgomery et al., 2022):

$$\frac{\partial \eta}{\partial t} = \frac{\partial}{\partial x} \left(D \frac{\partial \eta}{\partial x} \right) \quad (2.1)$$

Where η is the water surface elevation, t is time, x is the horizontal distance, and D is the diffusion coefficient. D defines how effectively the surge level spreads based on whether the flow occurs through *non-channelized* or *channelized* mangrove forests. A higher diffusion coefficient indicates a larger rate of water exchange (Montgomery et al., 2019).

Non-channelized flow

For a mangrove forest without channels, the friction provided by mangrove roots, trunks, and branches determines D , which is expressed as (Montgomery et al., 2022):

$$D = \eta_v \sqrt{\frac{2g}{a_v C_v \left| \frac{\partial \eta}{\partial x} \right|}} \quad (2.2)$$

In this equation, η_v denotes the forest water depth, g is the gravitational acceleration, a_v represents the vegetation frontal area density, C_v is the vegetation drag coefficient, and $\left| \frac{\partial \eta}{\partial x} \right|$ is the sea surface slope. Larger frontal vegetation area density (a_v) and shallower water depths (η_v) result in greater attenuation.

Channelized flow

For channelized flow, the friction on the surge comes mainly from the channel itself rather than the mangrove vegetation. Channels allow the surge to bypass mangroves, resulting in lower attenuation rates compared to non-channelized mangroves (Montgomery et al., 2022). The diffusion coefficient in this case is given as (Montgomery et al., 2022):

$$D = \eta_c^{1.5} \sqrt{\frac{g}{C_c \left| \frac{\partial \eta}{\partial x} \right|}} \quad (2.3)$$

Here, η_c denotes the channel water depth, and C_c is the channel drag coefficient.

Summing up, the diffusion equation is used to describe how mangrove forests attenuate surge. A low diffusion coefficient (e.g., due to dense vegetation and shallow water) enhances attenuation and reduces flood extent. Conversely, a high diffusion coefficient (e.g., due to sparse vegetation or deeper water) results in higher fluid exchange and less attenuation, increasing the flood extent. The distinction between channelized and non-channelized flow is critical, as channelized systems generally lower the effectiveness of attenuation by mangroves. These factors stress the importance of local landscape features.

With the formulation of storm surge dynamics and its attenuation by mangroves now established, the focus extends to an overview, provided below, of the key ecological, geomorphological, and hydrodynamic variables that influence surge attenuation. These variables collectively determine the effectiveness of mangrove forests in mitigating surge impacts. It is important to acknowledge that numerous additional variables contribute to this complex process, some of which are not included in the following overview. The overview is necessarily concise and represents a simplified approximation of these interactions.

Variables affecting surge attenuation by mangroves

Hydrodynamic variables:

1. **Storm surge height:** Higher storm surges generally result in lower attenuation rates as the relative influence of vegetation-induced friction diminishes compared to the higher momentum of the surge. This is reflected in the diffusion equation, where increased water depth leads to a higher diffusion coefficient, enabling more fluid exchange (Montgomery et al., 2022). Moreover, high surge levels may also damage mangrove forests, limiting their further capacity to attenuate flooding (Krauss & Osland, 2019).
2. **Forward speed of the storm:** Surges from faster-moving storms tend to be attenuated more effectively by mangroves than slower-moving storms (Zhang et al., 2012). Slower-moving storms allow more time for surge waters to propagate through the mangrove forest, leading to more flooding (Montgomery et al., 2019). Zhang et al. (2012) demonstrated that mangroves provide better attenuation for a fast-moving Category 5 storm (11.2 m/s) than a slow-moving Category 5 storm (2.2 m/s).

Ecological variables:

1. **Mangrove forest width:** Wider mangrove forests result in greater surge height reduction, as shown in Figure A.6. Zhang et al. (2012) demonstrated that the relationship between forest width and surge attenuation is non-linear, with the greatest attenuation occurring at the seaward edge of the forest and flattening further inland. Studies report a range of attenuation rates from 5–15 cm/km to as high as 50 cm/km (Krauss et al., 2009; Mclvor et al., 2012b; Zhang et al., 2012). Due to the large spatial scale of storm surges, extensive forest widths are generally required to achieve attenuation.
2. **Mangrove biomass:** This parameter serves as a measure of both structural complexity of individual trees and overall mangrove forest density, which vary by species and forest age. Root systems play a key role in the structural complexity, with dense prop roots of *Rhizophora* and the pneumatophores of *Avicennia* providing attenuation (Mclvor et al., 2012b). At higher water levels, more flexible branches and leaves also contribute. Empirical data linking species-specific structures to surge reduction remain limited (Mclvor et al., 2012b). Given the interplay of these factors, above-ground biomass is used as a metric to encompass both the structural complexity and forest density of mangroves in relation to their impact on surge attenuation.
3. **Species zonation:** The spatial distribution of mangrove species across the cross-shore plays a role in surge attenuation. As shown in Figure A.6, the attenuation rate decreases non-linearly further inland, indicating that the seaward-most trees contribute disproportionately to surge dissipation (Mclvor et al., 2012b). If the densest mangroves are positioned inland, the overall attenuation may be reduced. Furthermore, the zonation of species influences the resilience of the forest, as seaward-positioned species experience higher hydrodynamic forces and must mitigate erosion, which can compromise long-term coastal protection.

Geomorphological variables:

1. **Topography (coastal slope):** Gentler coastal slopes can result in greater attenuation. Tanaka (2008) demonstrated that on a gentle slope (1:500), mangroves reduced water levels behind the vegetation by up to 80 cm, while on a steeper slope (1:100), the reduction was only 12–28 cm. Tanaka (2008) compared both vegetated and non-vegetated conditions, showing that while wave attenuation is generally greater on milder slopes even without vegetation, the relative contribution of vegetation to surge attenuation is larger on gentler slopes, meaning that a higher percentage of total attenuation is attributed to mangroves compared to steeper slopes (Tanaka, 2008). This suggests that mangroves are more effective at lowering surge levels on lower coastal slopes than on steeper slopes (Mclvor et al., 2012b).
2. **Presence of channels and ponds:** The presence of channels in mangrove area reduces surge attenuation (Montgomery et al., 2022). Channels allow storm surges to bypass vegetation, limiting the friction the mangroves can apply on the surge to slow down the propagation and lower water levels. A study by Montgomery et al. (2022) showed that channelization could drastically reduce or even eliminate attenuation.

Mangrove impact 2: Short wave attenuation

Mangroves have been demonstrated to be effective in attenuating short wave energy (Temmerman et al., 2022). According to Mclvor et al. (2012b), mangroves have been shown to reduce short wave energy and wave height by more than 75–100% over a 1 km forest width. A more recent study by Van Wesenbeeck et al. (2025) showed that mangrove forests that are at least 500 m wide can reduce 75% of wave energy.

To represent the attenuation of short wave energy by mangroves analytically, a wave energy balance approach is employed, where mangrove vegetation is introduced as a dissipation term (Mendez & Losada, 2004). The network of mangrove roots, branches, and stems imposes frictional resistance on incoming waves, thereby reducing wave energy and thus height (Temmerman et al., 2022). This frictional force exerted by mangroves on waves can be described by the following expression (Dalrymple et al., 1984; Van Rooijen et al., 2016):

$$F_D = \frac{1}{2} \rho C_D b_v N u |u| \quad (2.4)$$

Here, ρ is the density of water, C_D is the drag coefficient, b_v represents the mangrove stem width, N is the number of stems per unit area, and u is the horizontal velocity of the wave-induced flow.

Using linear wave theory to describe wave propagation, the frictional force exerted by mangroves results in an energy dissipation term within the wave energy balance. This dissipation term is formulated by Dalrymple et al. (1984) as follows:

$$\epsilon_v = \frac{\rho \cdot C_D \cdot N \cdot D_s}{2\sqrt{\pi}} \cdot \left(\frac{g \cdot k}{2 \cdot \sigma} \right)^3 \cdot \frac{\sinh^3(k\alpha h) + 3 \cdot \sinh(k\alpha h)}{3k \cdot \sinh^3(kh)} \cdot H_{rms}^3 \quad (2.5)$$

In Equation 2.5, ϵ_v represents the vegetation-induced dissipation of wave energy, ρ is the water density, C_D is the drag coefficient, N is the number of stems per unit area, D_s denotes the stem diameter, g is the gravitational acceleration, k is the wave number, σ is the angular wave frequency, h represents the water depth, H_{rms} is the root-mean-square wave height, and α denotes the relative height of the vegetation.

However, as previously mentioned, the attenuation of short wave energy does not necessarily translate into a reduction in total water level or flood extent. The contribution of wave set-up, a component associated with short waves, is often overlooked concerning mangroves and wave attenuation, as highlighted by Van Rooijen et al. (2016).

In the surf and swash zones, short wave energy is transformed into wave set-up and run-up, respectively. When waves have not yet broken before reaching the mangroves, the attenuation of short wave energy by vegetation leads to a reduction in the energy available to generate set-up, thus logically resulting in a lower set-up. However, in scenarios involving large offshore waves, such as during tropical storms, it is likely that waves have already broken before entering the mangrove zone, not unlikely in shallow coastal areas where mangroves typically grow. In these cases, much of the wave set-up is likely generated prior to any interaction with the vegetation. Besides reducing the initial generation of wave set-up by attenuating short wave energy, mangroves can naturally also reduce the set-up itself, quite similar to the attenuation of surge. Van Rooijen et al. (2016) investigated the influence of vegetation on set-up, demonstrating that mangroves can interact with and diminish set-up, with the degree of this interaction depending on the local geomorphological characteristics.

The ability of mangroves to attenuate short waves is influenced by a range of ecological, geomorphological, and hydrodynamic factors, of which the following overview is provided. Again, it should be noted that this overview does not encompass all variables influencing short wave attenuation and represents a simplified approximation of a complex process.

Variables affecting short wave attenuation by mangroves

Hydrodynamic variables:

1. **Wave height:** For short waves, larger incoming wave heights demonstrated higher attenuation rates by mangroves than lower incoming wave heights, when water levels are at the height of branches and leaves, as shown in Figure A.7 (Gijon et al., 2021; Mazda et al., 2006). This observation aligns with field studies showing that mangroves perform more effectively at reducing higher incoming waves compared to smaller waves (Horstman et al., 2014). At a coast without mangroves, this pattern between higher incoming wave heights and more wave energy reduction was not observed, shown in Figure A.7 (McIvor et al., 2012a).
2. **Wave period:** Waves, with the same incoming wave height, with periods of 20 seconds and shorter are attenuated more effectively by mangroves than longer-period waves, which subsequently require wider forests to be strongly reduced, as shown in Figure A.8 (Gijon Mancheño, 2022).
3. **Water depth:** Attenuation rates decrease with greater water depth, which is also related to the tidal phase (Temmerman et al., 2022). Van Wesenbeeck et al. (2022) showed that short-wave attenuation relies much on water depth, with real-scale flume tests on willow trees showing greater attenuation at 3 m depth than at 4.5 m. Probably, this is because attenuation is most effective when the frontal surface area of the vegetation compared to the submerged area is maximized (Van Wesenbeeck et al., 2022). Additionally, their study highlights that very flexible elements, such as leaves, contribute only to a small extent to attenuation, explaining the reduced attenuation rates at higher water levels (Van Wesenbeeck et al., 2022).

Ecological variables:

1. **Forest width:** The width of the mangrove forest determines the extent of wave-vegetation interaction and thus the amount of wave energy dissipated by the vegetation, shown in Figure A.9. At least 500 m of forest width is required to attenuate short waves by 75%, regardless of other factors (Van Wesenbeeck et al., 2025). At narrower forest widths, attenuation becomes dependent on other variables including water level, incoming wave height, and forest characteristics (Van Wesenbeeck et al., 2025).
2. **Mangrove biomass:** The parameter above-ground biomass (Mg/ha) encompasses species characteristics and forest density. Higher biomass generally corresponds to greater structural complexity and forest density, contributing to wave dissipation. Rhizophora species, with prop root systems, maintain a high frontal area density across a range of water depths, as opposed to Avicennia, whose pneumatophores taper off more abruptly with depth, shown in Figure A.10 (Horstman et al., 2014; Sánchez-Núñez et al., 2020). Linked to species characteristics, overall forest density plays a role, as denser forests increase wave energy dissipation, shown in Figure A.11 (Horstman et al., 2014). Above-ground biomass serves as a metric to quantify these effects in a single parameter.
3. **Species zonation:** The effectiveness of mangroves in attenuating short waves is dependent on the zonation of species along the cross-shore profile. As waves propagate through the forest, they experience nonlinear decay, with the largest reductions occurring in the first tens of meters of the forest, as illustrated in Figure A.6 (Gijon Mancheño et al., 2021, Quang Bao, 2011). Figure A.6 also shows that the extent of wave height reduction is influenced by the specific mangrove species present, as different species exhibit varying structural characteristics for wave dissipation. Species with denser root and branch structures, when positioned at the seaward side, could enhance this initial wave dissipation. If less dense species dominate the outer fringe, wave energy may propagate deeper into the forest. The zonation also affects sediment stabilization, as wave-induced erosion is greater in the absence of robust root networks at the seaward side.

Geomorphological variables:

1. **Topography (coastal slope):** The slope of the coastline plays a role in determining wave attenuation by influencing the interplay between shoaling, wave breaking, bottom friction, and vegetation drag, as shown in Figure A.12 (Parvathy & Bhaskaran, 2017). A study by Parvathy and Bhaskaran (2017) showed that on all tested slopes (1:80 to 1:10) sufficient wave attenuation took place, yet to a different extent. Mild slopes (1:80 to 1:40) showed an exponential decay of wave height with energy reductions of 93–98%. In contrast, steeper slopes (1:10), result in more gradual energy reductions of 67% (Parvathy & Bhaskaran, 2017).

Mangrove impact 3: Water storage effect

Mangroves not only reduce flood extents through the dissipation of short waves and the slowing down of surge propagation, but they can also act as a natural water storage system (Montgomery et al., 2022). This water storage effect is similar to the role of green spaces in urban environments, where vegetation helps prevent flooding by holding water. Within mangrove forests, the inner part of the forest functions as a reservoir, storing water during surge events, while the outer edge restricts the initial water exchange (Montgomery et al., 2019).

Variables affecting water storage capacity by mangroves

Ecological variables

1. **Forest width:** The effectiveness of the water storage mechanism is primarily determined by the width of the mangrove forest. Wider forests have a greater capacity to store water in their inner sections (Montgomery et al., 2019).

2.4. Conceptual guideline

The objective of this guideline is to structure the thinking process when assessing the potential of mangroves to reduce flood extent. Rather than providing strict quantitative thresholds, the guideline serves as a framework for decision-making, helping to systematically evaluate whether the local conditions support or limit the effectiveness of mangroves in mitigating flood impacts. This approach is necessary due to the lack of comprehensive quantitative data in a variety of locations.

To synthesize the findings of the literature study, mangroves influence flood extent during tropical storms through three primary mechanisms: (1) surge attenuation, (2) short wave attenuation, and (3) water storage. In the current literature, the role of water storage in reducing flood extent remains relatively underexplored. Consequently, this mechanism is excluded from further consideration in the conceptual guideline and subsequent analyses, which will focus exclusively on surge- and short wave attenuation.

Assessing the flood mitigation potential of mangroves requires consideration of the coastal type in which the forest is situated, as it strongly influences key hydrodynamic processes such as wave breaking, wave set-up, and surge amplification. To incorporate the coastal type, the biophysical typology of Worthington, Zu Ermgassen, et al. (2020) is applied in the conceptual guideline. Moreover, the guideline incorporates the dominant hydrodynamic driver of the flood, either storm surge or short waves. For each driver, a specific pathway is provided with the *ecological*, *geomorphological*, and *hydrodynamic* components impacting attenuation by mangroves. It should be noted that precipitation is included in the guideline as one of the hydrodynamic drivers to flood extent. However, it is not linked to any of the subsequent pathways, as mangroves have limited influence on precipitation-induced flooding and pluvial flooding lies beyond the scope of this study.

While the conceptual guideline aims to provide a structured and accessible framework for assessing the potential of mangroves to reduce flood extent during tropical storms, nuances should be considered. In order to translate a complex physical system into a usable decision-making guideline, certain simplifications have been made. These include the interdependency of variables, the role of wave set-up, the long-term influence of mangroves on coastal protection, and the distinction between flood depth and flood extent. Each of these considerations is elaborated on in the discussion in chapter 5.

Acknowledging these limitations, the conceptual guideline remains a valuable tool for introducing structure into the complex assessment of mangrove-based flood attenuation. It is intended to support decision-makers in identifying coastal locations where mangroves are likely to provide natural protection against flooding during tropical storm events. The variables incorporated into the guideline are listed in section A.4. These variables also serve as the foundation for the subsequent remote sensing analysis, thereby ensuring methodological continuity between the conceptual guideline and the remote sensing component of this study. An overview of the final conceptual guideline is presented on the following page. Zoomed-in versions of the separate sections can be found in section A.5 for better readability.

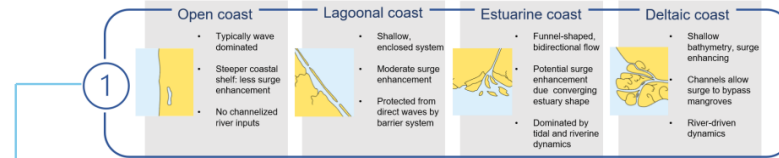
Conceptual guideline for assessing flood extent reduction by mangroves following tropical storms

Step 0: Identify the flood extent

What is the spatial extent of the flood caused by the tropical storm?

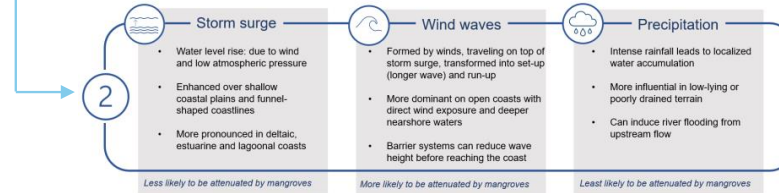
Step 1: Identify the mangrove coastal type

What is the coastal type where the mangrove forest is located?



Step 2: Determine the dominant hydrodynamic forcing

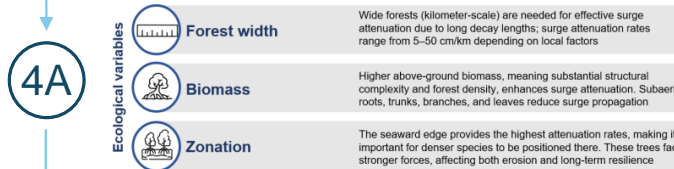
Which hydrodynamic forcing contributes most to flood extent during a tropical storm at this location?



Step 3A: If storm surge is the dominant mechanism



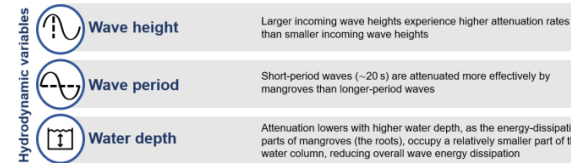
Step 4A: Ecological variables for surge attenuation



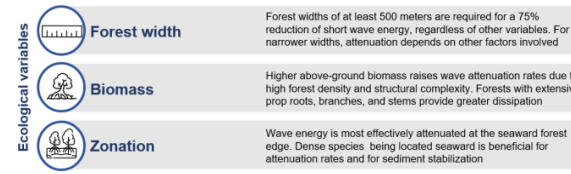
Step 5A: Geomorphological variables for surge attenuation



Step 3B: If wind waves are the dominant mechanism



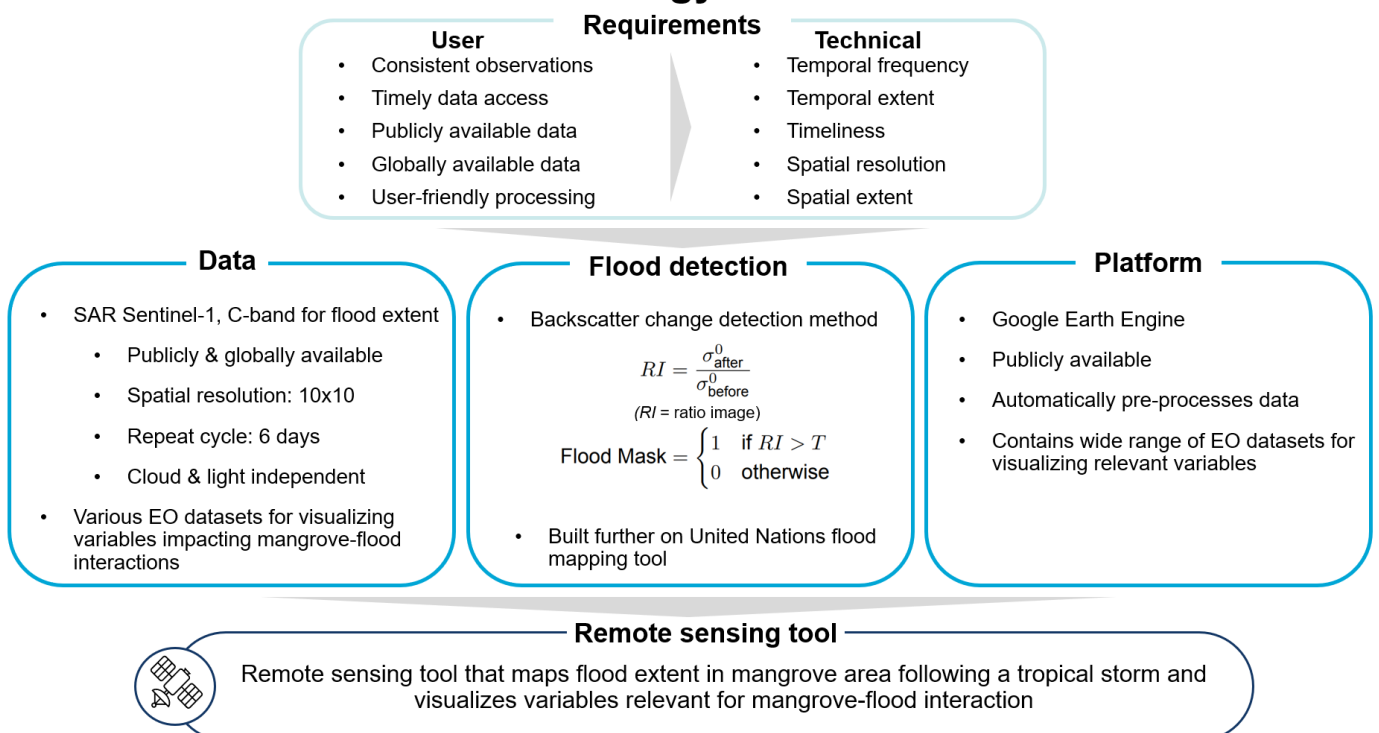
Step 4B: Ecological variables for wave attenuation



Step 5B: Geomorphological variables for wave attenuation



Methodology overview



As highlighted in the conceptual guideline, assessing the role of mangroves in flood extent reduction during tropical storms requires consideration of geomorphological, ecological, and hydrodynamic variables. Given the complexity of these influencing factors, it is challenging to incorporate them into hydrodynamic models, which lack validation from field observations. To make remote sensing a valuable complement to these existing numerical approaches, the method developed in this study must be capable of capturing the flood extent resulting from actual tropical storm events, thereby reflecting the complex interactions. In doing so, the remote sensing approach can contribute by supplementing hydrodynamic models, which currently face limitations in empirical grounding.

Since flood extent is the dependent variable in this research, the scope of the remote sensing method is focused on the detection of flood extent in mangrove areas affected by tropical storms. A key methodological demand is that the tool also enables the integration of the influencing variables identified in the conceptual guideline. While the direct remote sensing of these additional variables falls outside the scope of this thesis, many of them are available through existing open-access earth observation (EO) datasets. Integrating these EO datasets within the tool provides a more comprehensive picture of the conditions shaping flood extent.

The following section outlines the user and technical requirements of the remote sensing tool, describes

the selected satellite data, the flood mapping method, and the processing platform. A methodological framework provides a step-by-step explanation of the developed tool, including its testing procedures, flood detection process, and integration of variables. Background information on remote sensing—covering both radar and optical remote sensing, backscattering mechanisms, and details of the Sentinel-1 mission from which the data are sourced—is provided in section B.3. Moreover, section B.4 outlines how the variables identified in the conceptual guideline can be detected using remote sensing-derived metrics. This demonstrates how EO data enables the integration of key factors influencing flood attenuation by mangroves into the assessment. In doing so, it stresses the potential of remote sensing to provide a more comprehensive understanding of flood mitigation by mangroves.

3.1. Methodological requirements

3.1.1. User requirements

The remote sensing tool aims to provide an assessment of flood extent in mangrove areas following a tropical storm. To ensure accessibility and reliable performance, the tool must meet the following key user requirements:

- **Consistent observations:** The tool must enable data acquisition under diverse atmospheric and lighting conditions. Tropical storms are often accompanied by dense cloud cover and may occur during nighttime, which limits the effectiveness of optical sensors. Therefore, it is essential that the tool utilizes observation methods that are unaffected by cloud or light conditions. Consistent observations are crucial for capturing the flood extent as soon as possible after the event.
- **Timely data access:** The tool must facilitate rapid access to flood extent information following data acquisition, ensuring that flood mapping results are available within a few days after the event. This is important to support relevant post-flood assessments.
- **Publicly available data sources:** The tool must rely on freely accessible satellite data, ensuring that it can be utilized in resource-limited regions.
- **Globally available data sources:** The tool must rely on data sources that offer global coverage to ensure applicability across all mangrove regions worldwide. This guarantees that the tool is not constrained to specific geographic areas and can be deployed universally.
- **User-friendly processing:** The tool should be developed on an open-access, cloud-based platform to support scalable and efficient data processing. It must be accessible to a broad range of users, including those with limited experience in remote sensing. A streamlined workflow is essential to ensure that non-expert users can apply the tool for flood mapping and assessment without requiring extensive technical expertise.

3.1.2. Technical requirements

The user requirements necessitate a set of technical requirements that determine the required characteristics of the satellite data sources and flood detection method. The following technical requirements are set:

- **Temporal frequency:** To respond to the user requirement of consistent observations, a high temporal frequency is essential to capture the flood extent on time after the occurrence of the event, since floodwaters may recede within a day. This creates a challenge, as the flood event may occur and recede between satellite overpasses, potentially missing the critical observation window. As a result, temporal frequency is likely the most critical technical requirement.
- **Temporal extent:** The tool must allow pre- and post-event comparisons to detect flood extent. Access to satellite data spanning approximately a decade or more provides first opportunities to study previous tropical storms and their associated flood extents.
- **Timeliness:** Since the tool is intended for post-storm assessment rather than emergency response, near-real-time data is not really essential. However, to ensure relevance, flood extent data should still be available within a short time frame (within days) after the event.
- **Spatial resolution:** The resolution must be sufficient to detect variations in flood extent. A resolution of at least 20 m is required to effectively distinguish differences in flooded areas. A finer resolution improves precision in flood delineation, ensuring that changes are captured.

- **Spatial extent:** A substantial spatial extent is required to capture both flooded and non-flooded areas around the mangrove forest area at a coastal region. Given that tropical storms impact wide coastal regions, the system should ideally cover an area in the range of 200 km per observation to ensure a comprehensive view of flood extent (von Storch & Woth, 2008).

3.2. Remote sensing tool

3.2.1. SAR Sentinel-1 C-band

Considering the user- and technical requirements, this study selected Sentinel-1 C-band Synthetic Aperture Radar (SAR) data, specifically from the Sentinel-1 satellites, as the data source for flood detection, its information is summarized in Table 3.1. Further information on radar remote sensing is provided in section B.2.

Satellite	Spatial resolution	Swath width	Repeat cycle	Primary function
Sentinel-1 (C-band SAR)	10 m × 10 m (GRD, IW mode), VV/VH polarization	250 km	6 days	Cloud-independent flood extent mapping using SAR-based change detection

Table 3.1: Specifications of Sentinel-1 used for flood extent mapping (SentiWiki, 2024).

Responding to the user requirement of consistent observations and the technical requirement of temporal frequency, Sentinel-1 SAR C-band data is selected for flood extent detection due to its ability to operate independently of cloud cover, a critical advantage given the persistent cloud conditions associated with tropical storms (Zhang et al., 2018). Optical sensors, such as Sentinel-2, often face limitations due to cloud obstruction, making SAR the better option for pre- and post-event flood mapping. The selection of C-band SAR data is further justified by its global and free availability, aligning with the user requirements of publicly and globally available data sources. While C-band SAR is rather limited in its ability to detect floodwater beneath dense mangrove canopies due to limited penetration through vegetation, this is considered acceptable, as the primary objective is to identify flooding inland of the mangrove belt—the zones where population, assets, and infrastructure are typically exposed to flood hazard. Furthermore, the technical requirement for sufficient spatial resolution and spatial extent is fulfilled, given the spatial resolution of 10 by 10 meters and the swath width of 250 km provided by a single Sentinel-1 image (see Table 3.1).

3.2.2. Change detection

The selected flood mapping technique in this study is a change detection method using SAR imagery. The methodology builds upon the flood mapping framework developed by UN-SPIDER (United Nations Platform for Space-based Information for Disaster Management and Emergency Response), an initiative of the United Nations Office for Outer Space Affairs (UN-SPIDER, 2025). The UN-SPIDER tool was selected as the foundation of the remote sensing tool due to its emphasis on global applicability, open-source availability, and its origin from a recognized institution, responding to the user requirements. Furthermore, the UN-SPIDER tool has been applied and adapted in previous studies addressing tropical storm impacts, such as by Singh and Schoenmakers (2023), demonstrating its utility as a foundation for further development in the context of flood extent mapping, storm events, and mangroves.

The flood detection method is based on identifying changes in radar backscatter values between pre-storm and post-storm SAR imagery (UN-SPIDER, 2025). As explained in more detail in section B.2, different surface objects reflect radar signals back to the satellite sensor to varying degrees, depending on the surface roughness. When an area is flooded, the surface characteristics are altered, which in turn affects the radar backscatter. This change in backscatter forms the basis of the applied method. In this study, the UN-SPIDER approach is taken as a basis but is expanded and refined. Specifically,

the remote sensing tool developed in this study improves reliability by incorporating a time stack of pre-storm images rather than relying on a single pre-storm acquisition. Moreover, it includes refining and testing of key parameters and the integration of EO datasets that provide ecological, geomorphological, and hydrodynamic variables relevant to assessing flood interactions with mangrove systems.

Furthermore, the remote sensing tool introduces a comparative flood extent layer by incorporating a flood extent derived from a bathtub inundation model. This model, based on elevation and water level thresholds, provides insight into areas that could be flooded under a given water level scenario. Moreover, comparing this simulated flood extent with the SAR-detected extent allows for preliminary interpretations of where mangrove presence may have influenced flood extent.

3.2.3. Google Earth Engine

Google Earth Engine (GEE) is selected as the processing platform for the flood mapping techniques as it provides direct access to Sentinel-1 data, offers pre-processed datasets, operates in a cloud-based environment, is user-friendly, and includes a wide range of EO data products.

GEE aligns with the user requirements by ensuring access to publicly available data. Additionally, it provides a user-friendly interface that does not require advanced remote sensing expertise, making it suitable for a variety of users (Gorelick et al., 2017). Its cloud-based nature allows large-scale processing without the need for extensive computing resources and local storage (Gorelick et al., 2017).

From a technical requirements perspective, GEE meets the requirement for timely data availability, as Sentinel-1 imagery is processed and accessible about 24 hours after acquisition, according to Gorelick et al. (2017). The platform offers pre-processed satellite imagery and datasets, reducing the need for manual corrections and ensuring efficient workflow execution. For example, noise removal and radiometric calibration for Sentinel-1 SAR data is already automated in GEE. GEE's ability to handle large spatial datasets is particularly beneficial for flood extent assessments, where large areas need to be analyzed. Finally, many EO datasets can be integrated into GEE, allowing for the visualization of variables that influence mangrove–flood interactions. This removes the need to manually detect such variables (like mangrove extent) while still enabling their inclusion in the analysis. Given these features, GEE is selected as the platform for implementing the flood extent mapping tool in mangrove area under tropical storm conditions.

3.2.4. Methodological framework

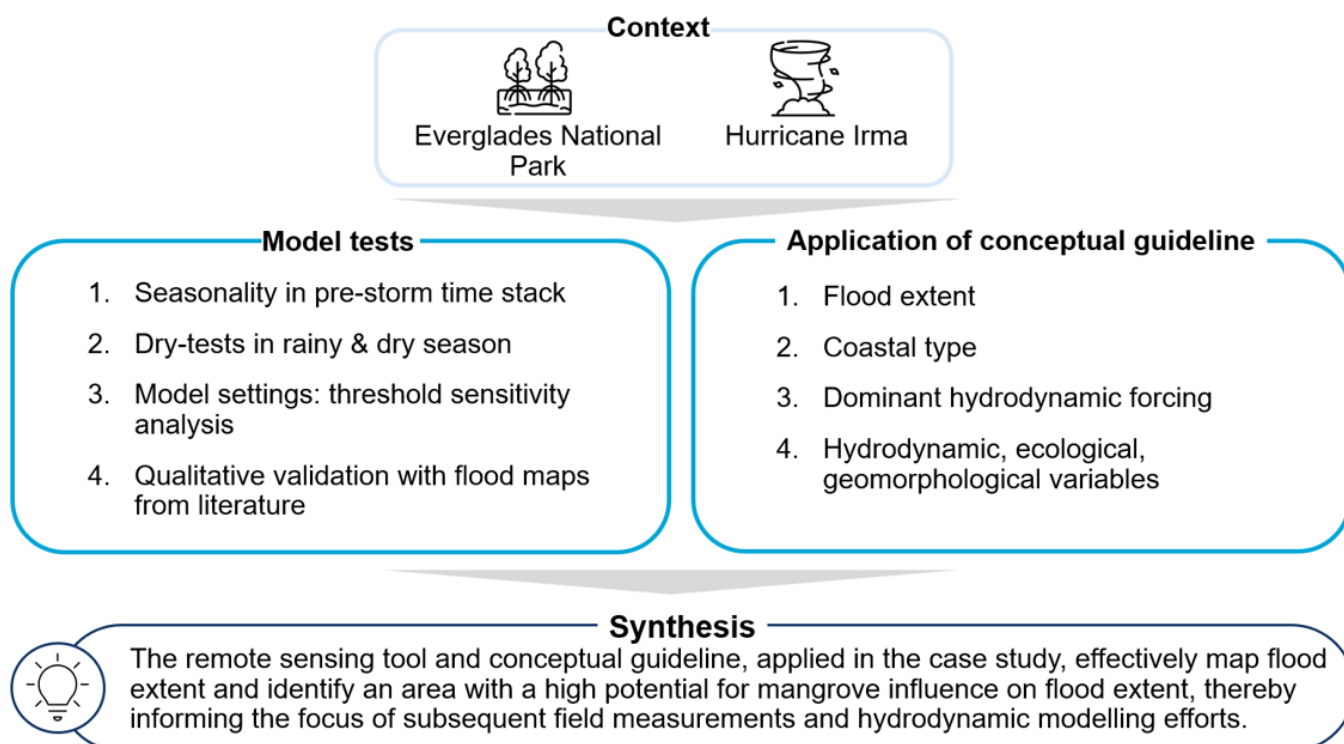
The subsequent page presents the methodological framework of the complete developed remote sensing tool, supported by a stepwise explanation provided in section B.5. The remote sensing tool includes the SAR-flood mapping method, the refining and testing of the flood mapping method, the bathtub inundation model for comparison, and the integration relevant variables through EO datasets. Finally, an overview of the datasets used in the remote sensing tool, along with their resolution and purposes, is presented in section B.6.

Methodological framework for flood extent mapping and integration of EO datasets in mangrove area under tropical storms



Case study

Case study overview



This case study focuses on the mangrove forest of the Everglades National Park in Florida, United States, following Hurricane Irma (2017). The objective is to evaluate whether the developed remote sensing tool can effectively map flood extent following the storm and account for the key variables relevant to mangrove-flood interactions. In doing so, the case study considers the potential contribution of the remote sensing flood extent output to hydrodynamic models that assess the role of mangroves in mitigating coastal flooding.

This chapter begins by providing background on the Everglades National Park and Hurricane Irma. Next, the remote sensing tool is tested and refined, and qualitatively compared to flood maps from literature as a first means of validation. Finally, the conceptual guideline is applied to the case study, with the remote sensing tool used to inform the guideline by providing the flood extent and the key variables addressed in the guideline, thereby adding to the understanding of the elements involved in flood extent reduction by mangroves following tropical storms.

4.1. Study area: The Everglades National Park

The case study area is located in South Florida and contains the Everglades National Park. The Everglades National Park, depicted in Figure 4.1, represents the largest mangrove forest in the United States (Han et al., 2018). Approximately 75% of the nation's mangroves are concentrated within the park (Lagomasino et al., 2021). The Everglades is an ecologically diverse and hydrologically dynamic landscape with a subtropical climate characterized by highly seasonal precipitation with a distinct rainy (May–October) and dry (November to April) season (Han et al., 2018; Zhang et al., 2018).

Landscape

As the National Park Service (2025b) describes: “It is home to rivers, lakes, wooded uplands, cypress swamps, brackish estuaries, coral reefs, and the sawgrass prairies known as the River of Grass. It is also home to dense urban centers, vast suburbs, Tribal lands, and working farms.” Moreover, the park plays an important role in the regional economy, driven by tourism, agriculture, fisheries, and as a source of drinking water (Choe & Schuett, 2020; National Park Service, 2025b). Established in 1947, the Everglades National Park spans approximately 5,700 km² and hosts over 830 different plant species (Todd et al., 2010). The intricate relationship between vegetation and hydrological processes plays a crucial role in shaping the wetland dynamics of the Everglades (Todd et al., 2010).

In addition to Everglades National Park, the region of the case study includes Water Conservation Areas, which serve roles in flood control, water storage, and ecosystem preservation. West of these conservation areas lies Big Cypress National Preserve, characterized by cypress trees standing in the water (National Park Service, 2025a). Further north—outside the boundaries of the present case study area—lies an agricultural zone established through the drainage of peatlands situated just south of Lake Okeechobee and adjacent to the Water Conservation Areas (Rodriguez et al., 2020). A map containing the boundaries of these areas is provided in Figure C.1, in section C.1.



Figure 4.1: Case study area of this research, containing the Everglades National Park, on which the conceptual guideline and the remote sensing tool are applied.

Mangrove forest

The mangrove forests of the Everglades extend over a 200 km-long belt along the Southwestern coast, covering approximately 2,800 km² with forest widths ranging from 6 to 30 km (Zhang et al., 2012). The mangrove forest consist predominantly of *Rhizophora mangle*, *Laguncularia racemosa*, and *Avicennia germinans* species, with tree heights varying between 4 and 18 meters, and stem diameters ranging from 5 to 60 cm (Zhang et al., 2012). Smaller mangrove formations, typically under 4 meters, are found further inland (Zhang et al., 2012). The region faces increasing challenges from hurricanes and sea-level rise (Lagomasino et al., 2021). Figure 4.2 illustrates the vulnerability of the geographic location

of the Everglades National Park in the Gulf of Mexico, highlighting its frequent exposure to hurricanes. Despite exposure to coastal flooding, the mangroves demonstrate regenerative capacity, enabling them to persist in this dynamic coastal environment to a large extent (Zhang et al., 2012).

Topography & bathymetry

In terms of topography, the Everglades is a low-relief landscape, with an average elevation increase of only 5 cm per kilometer, according to Stabenau et al. (2011). It features shallow bathymetry and a gentle coastal slope, making the area susceptible to high storm surges (Zhang et al., 2012). Such processes may have had a pronounced impact on the mangrove forests, which have migrated about 3 km inland since the 1940s, according to Stabenau et al. (2011). The Big Cypress National Preserve has a higher elevation than the adjacent mangrove area as it is situated above a limestone bedrock only (National Park Service, 2025a).

Tide & wave climate

Regarding the tide- and wave climate, the area experiences a semidiurnal tide, characterized by two high and two low waters per day. The tidal range is relatively small, approximately 0.3 to 0.6 meters (Zhang et al., 2012). The intricate network of many small islands on the Southwestern coast provides a sheltered environment with mild tidal and wave conditions.

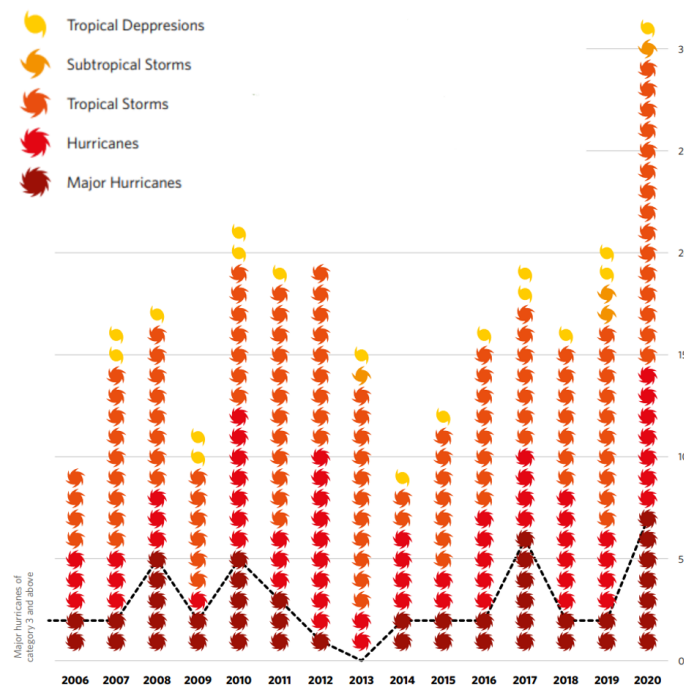


Figure 4.2: Frequency and intensity of tropical storm events in the Gulf of Mexico and the Caribbean from 2006 to 2020. The figure highlights the high occurrence of tropical depressions, subtropical storms, tropical storms, hurricanes, and major hurricanes in the region. Given that the Everglades and its mangrove ecosystems are located within this area, they are often exposed to severe tropical storms (Herrera-Silveira et al., 2022).

Hydrology, soil type & subsidence

The Everglades' hydrology is dominated by slow-moving, shallow water systems. The Taylor and Shark Rivers function as the primary drainage channels, discharging freshwater into the Gulf of Mexico (Han et al., 2018; Krauss et al., 2009). Historically, the Everglades functioned as an uninterrupted wetland system, receiving water from Lake Okeechobee, located to the north of the study area and flowing southward towards the Gulf of Mexico (Todd et al., 2010), as shown in Figure 4.3. This wetland system was thoroughly changed throughout the 20th century, when human interventions have altered the hydrology of the Everglades (Todd et al., 2010). Urbanization, agricultural expansion, and a large variety of water management infrastructure, including levees, drainage networks, and pumps, have drastically reshaped the natural flow of water in the region (Florida Museum, 2022; Gunderson & Light, 2007). While these changes facilitated agriculture and human settlement, they also disrupted the balance

of the Everglades' ecosystem, necessitating conservation efforts aimed at preserving the Everglades' hydrological and ecological functions (Gunderson & Light, 2007; Todd et al., 2010).

Furthermore, the main soil types in the area are fine-grained marl (a mixture of clay and calcium carbonate) and peat (which consists of decomposing organic matter) (National Park Service, 2025a). The bedrock below the marl and peat consists mainly of porous limestone (National Park Service, 2025a). The presence of peat and marl in the upper soil layers makes the area susceptible to subsidence. Subsidence occurred primarily outside the case study area, further north, in the Everglades Agricultural Area, as shown in Figure C.1. In this region, land drainage for agricultural use has led to peat soil compaction and subsequent gradual settling (Rodriguez et al., 2020). In contrast, subsidence is not taking place to the same extent in the case study area further south including the mangrove-dominated coastal zones, where the soil is not so much subject to artificial drainage.

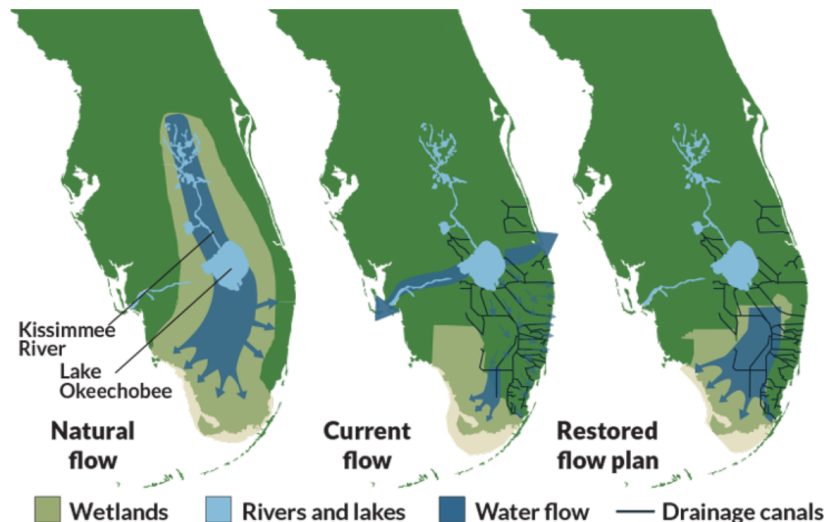


Figure 4.3: Changes in flow patterns in the Everglades due to human interventions. The natural flow (left) directed water from Lake Okeechobee through wetlands to the Gulf of Mexico. The current flow (middle) is changed by man-made drainage canals (black lines), leading water eastward and reducing flow to the southern wetlands. The restored flow that is planned (right) aims to re-establish more natural hydrological conditions (Florida Museum, 2022).

Road and canal networks

Given that the majority of the case study area consists of natural landscape, road density is relatively low, which is further illustrated in section C.1 in Figure C.2. A few main roads traverse the vegetated region, often elevated and accompanied by dikes, thereby forming physical barriers in the landscape that can influence water movement. In the Water Conservation Area, as further shown in Figure C.1, a network of small, man-made canals is present. These canals, which are not visible in the Earth observation imagery due to their narrow width, are laid out in a highly regular pattern.

4.2. Context: Hurricane Irma

Hurricane Irma, depicted in Figure 4.4, made landfall in South Florida on September 10, 2017, as a Category 4 hurricane, with sustained wind speeds of approximately 187 km/h (Lagomasino et al., 2021; Wingard et al., 2020). As the storm progressed northward, it weakened to a Category 3 hurricane (Wingard et al., 2020). In terms of intensity, Hurricane Irma ranked as the sixth-strongest storm since 1888 based on wind speed and central pressure (Wingard et al., 2020).

The impacts of Hurricane Irma were severe, including extensive flooding, reportedly caused by both rainfall and storm surge, and widespread destruction (Zhang et al., 2018). The economic damage was estimated at approximately 50 billion dollars (Narayan et al., 2019). The highest storm surge recorded within Everglades National Park reached approximately 3 meters (Narayan et al., 2019).

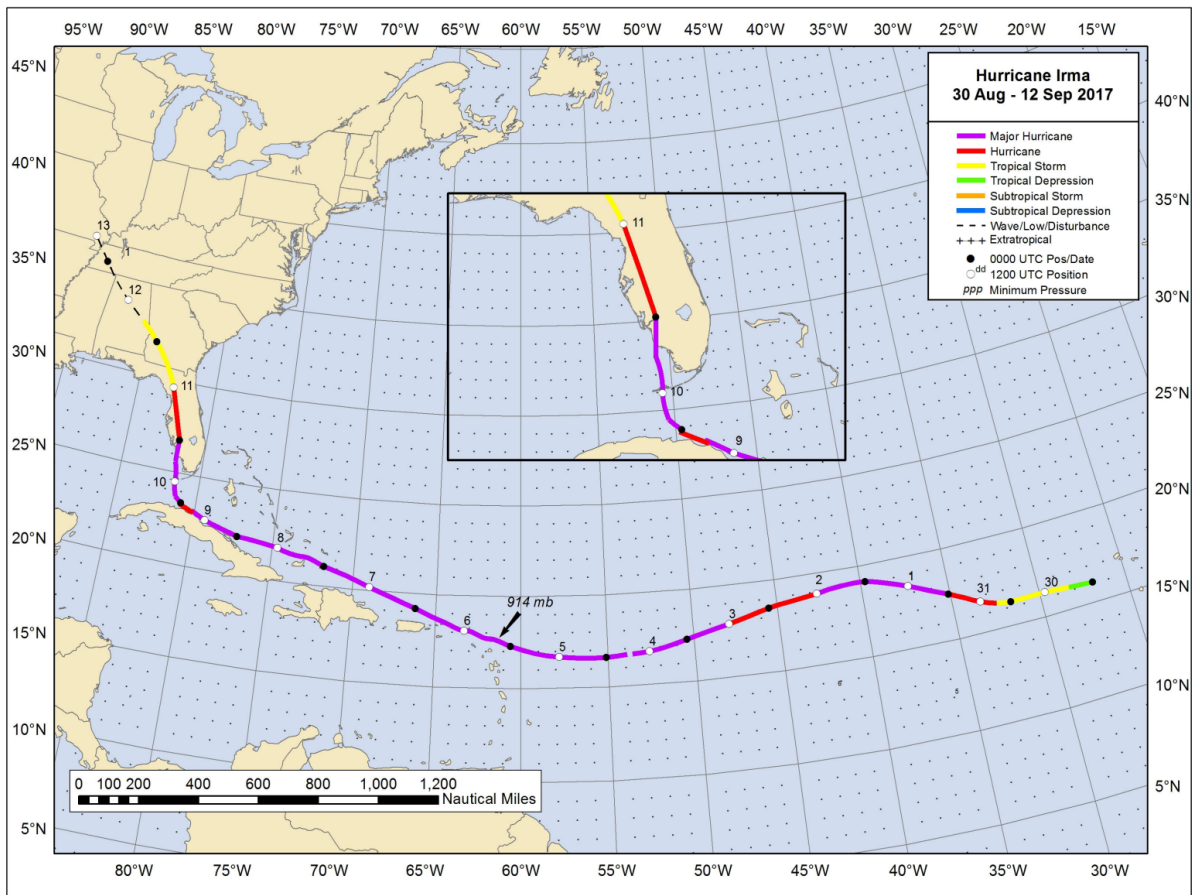


Figure 4.4: Track of Hurricane Irma, 2017. The colour-coded path represents the different storm classifications (NOAA, 2018).

4.3. Model testing and qualitative validation

To test and refine the developed remote sensing tool, the following analyses are conducted: (1) Testing the impact of different pre-storm time stack ranges on flood extent, (2) performing ‘dry tests’ in periods in the dry and rainy season with no reported flooding, (3) adjusting the model settings to optimize performance for this event, including a sensitivity analysis of the change detection threshold, and (4) qualitatively comparing the resulting flood extent map with two flood maps from literature as a first step of validation. It should be noted that the analysis of the flood extent itself—for example the spatial distribution and explaining observed tiling patterns—is addressed in detail in subsection 4.4.1.

4.3.1. Pre-storm time stack

As the remote sensing tool detects flooding from a specific event, the selection of post-storm imagery is constrained. However, there is flexibility in choosing the pre-storm imagery. Relying on a single pre-storm image may introduce errors, due to potential speckle noise, which could affect the accuracy of the detected flood extent. For this reason, unlike the UN-SPIDER (2025) approach, this research uses a time stack for the pre-storm image, in which the backscatter values from multiple pre-storm images are averaged, to minimize the impact of noise from an individual image. To explore this further, first, the difference between using a single pre-storm image and a time stack is assessed. Second, the influence of seasonality within the pre-storm time stack on the resulting flood extent is evaluated.

Pre-storm single image vs. time stack

The mapped flood extent using the pre-storm time stack is 168,811 hectares, whereas the flood extent derived from a single pre-storm image (2017-08-29) is 177,891 hectares. The higher flood extent detected with the single-image approach could suggest a greater presence of false positives, perhaps due to more noise in the single image, which is averaged out when using a more stable pre-storm time

stack.

Seasonality in pre-event time stack

As noted by Zhang et al. (2018), seasonal variations influence SAR backscatter values. When pre-storm images in the time stack are drawn from multiple seasons, the variation in backscatter is greater than when all images originate from the same season. Consequently, changes between pre- and post-storm images, indicative of flooding, may be less detectable. Specifically, two scenarios are tested:

- A single-season time stack, where pre-storm images are selected exclusively from the rainy season, corresponding to the season in which the flood occurred.
- A mixed-season time stack, incorporating images from both the rainy and dry seasons.

The results, shown in Table 4.1, demonstrate that when a mixed-season dataset is used, the total detected flood extent is much lower than when single-season images are included (89,290 hectares compared to 168,811 hectares). This lower flood extent for the mixed time stack is also shown in Figure 4.5a. This finding aligns with Zhang et al. (2018), who emphasized the importance of ensuring that pre-storm SAR imagery in the time stack originates from the same season to minimize seasonal variation in backscatter which lowers flood extent detection. The details of the used specific satellite data are provided in Table C.1, Table C.2 and Table C.3.

Table 4.1: Comparison of flood extent of Hurricane Irma using pre-storm image time stacks from the same season and mixed seasons.

Pre-storm stack	Flood extent (ha)
Rainy season only	168,811
2017-06-18 (Rainy)	
2017-07-24 (Rainy)	
2017-08-17 (Rainy)	
2017-08-29 (Rainy)	
Mixed seasons	89,290
2017-03-02 (Dry)	
2017-03-26 (Dry)	
2017-05-13 (Rainy)	
2017-06-18 (Rainy)	

4.3.2. Dry tests

To assess the model's behaviour in the absence of actual flooding, a series of "dry tests" are conducted. For each of the years 2017, 2018, and 2019, the same three dates were selected in both the rainy and dry seasons, during periods when no flooding was reported. Both dry- and rainy-season periods were selected to examine the extent to which seasonal factors influence the occurrence of false-positive flood detections. The selected dates were used as input in the remote sensing tool, using a post-storm window of 0–12 days. For the pre-storm imagery, a time stack was compiled from the preceding months within the same season. The information on the specific satellite data is documented in Table C.4 and Table C.5. Table 4.2 presents the selected dates across the three years for both the dry and rainy seasons, along with the corresponding flood extent in hectares detected for each dry test.

As shown in Table 4.2, the model detects flood extent in periods when no floods were reported. The average flooded area in these 12 dry tests is 3,614 hectares. The difference in dry test flood extent between the seasons is minimal, the average detected flooded area in the dry tests in the rainy season is 3,747 hectares, while in the dry season, it is 3,481 hectares. In comparison, the flood extent following Irma is 168,811 hectares. When the dry-season dry tests are regarded as false positives, the average flood extent they produce accounts for only 2% of the flood extent recorded following Hurricane Irma.

It can reasonably be assumed that the flood extent detected during dry-season dry tests represents false positives, as no flood events or major rainfall were reported during this period. Such misclassifications may result from a range of factors, including variations in soil moisture and vegetation growth,

Table 4.2: Dry tests: Flooded area (hectares) in periods of no reported flooding, detected by the model in dry and rainy seasons (2017-2019)

Year	Date	Season	Hectares flooded
2017	2017-12-05	Dry	2073
2018	2018-12-05	Dry	1232
2019	2019-12-05	Dry	3826
2017	2017-12-25	Dry	1473
2018	2018-12-25	Dry	4187
2019	2019-12-25	Dry	8093
2017	2017-08-15	Rainy	612
2018	2018-08-15	Rainy	3100
2019	2019-08-15	Rainy	7076
2017	2017-07-15	Rainy	5133
2018	2018-07-15	Rainy	1982
2019	2019-07-15	Rainy	4579

which can alter backscatter values. Urban features and shadow effects may also influence signal returns. Additionally, speckle noise inherent to SAR imagery remains a potential source of false flood identification. Flood extent detected during dry tests in the rainy season may represent either false positives or actual flooding resulting from intense local rainfall. It cannot be ruled out that localized precipitation led to genuine inundation in some areas. Therefore, flood detections during the rainy season cannot be definitively classified as misclassifications. Further research involving a longer time series and detailed rainfall data would be necessary to distinguish between these scenarios. Such an investigation could also provide valuable insights into the spatial patterns of water accumulation during heavy rainfall events.

To consider the spatial distribution of flood extents detected during the dry tests, a series of maps was generated, as shown in Figure 4.5. Figure 4.5b displays flood detections from the dry tests, with red indicating detections during the dry season and green representing those during the rainy season. Overlapping detections appear in darker shades. Figure 4.5c shows the dry test of the dry season flood extent (red) and the SAR-derived flood extent following Hurricane Irma, shown in blue. Figure 4.5d presents the land cover classification of the study area based on NLCD data and the flood extent from the dry test in the dry season shown in black, to explore potential associations between land cover types and areas prone to flood detection in the dry tests (U.S. Geological Survey (USGS), 2024).

In panel (b), limited overlap is observed between dry-season and rainy-season detections. Both are spatially scattered, though some areas show localized clustering. The red detections likely represent false positives, while the green detections may also be false positives or reflect actual flooding caused by localized precipitation. In panel (c), only the dry test from the dry season is included as they are most likely false positives. Limited overlap is observed between the false positives and the flood extent of Irma, with the exception of the southern part of the Irma flood extent, where the overlapping areas shown in darker colour suggest potential false positives. In contrast, the other false positive areas in the western region, do not align with Irma's flood extent. The overlapping areas in the south indicate that the flood extent mapped there for Hurricane Irma may not represent actual flooding, as these same areas also appear as flooded during a dry-season test period without any reported rainfall or flooding. This should be taken into account when interpreting the flood extent in this region.

In panel (d), the flood extent of the dry-season dry test is shown in black to maintain distinction from the underlying land cover map. Only the dry test from the dry season was used here to assess which land cover types are associated with false positives, as dry tests from the rainy season may reflect local rainfall and were therefore excluded. The areas of overlap between the Hurricane Irma flood extent and the dry-season dry test (panel c), which may represent false positives in the Irma flood map, align predominantly with the land cover type classified as emergent herbaceous wetlands. In other regions, where the dry tests did not overlap with the Irma flood extent, overlap was also observed with developed areas—particularly within the city of Miami—and with cultivated crop areas surrounding Miami. Figure 4.6 presents the flooded area (in hectares) from the dry-season dry test, categorized by land cover type. This was determined by calculating the number of dry-test pixels within each land

cover category. It clearly shows that emergent herbaceous wetlands account for the largest number of false positives by far. This is expected, as these wetlands can experience fluctuating water levels, which alters the backscatter detected by the satellite sensor, which is further explained in Figure B.4. Such changes in the wetland are identified by the tool as flooding, even though the area may not be truly flooded but simply became slightly wetter.

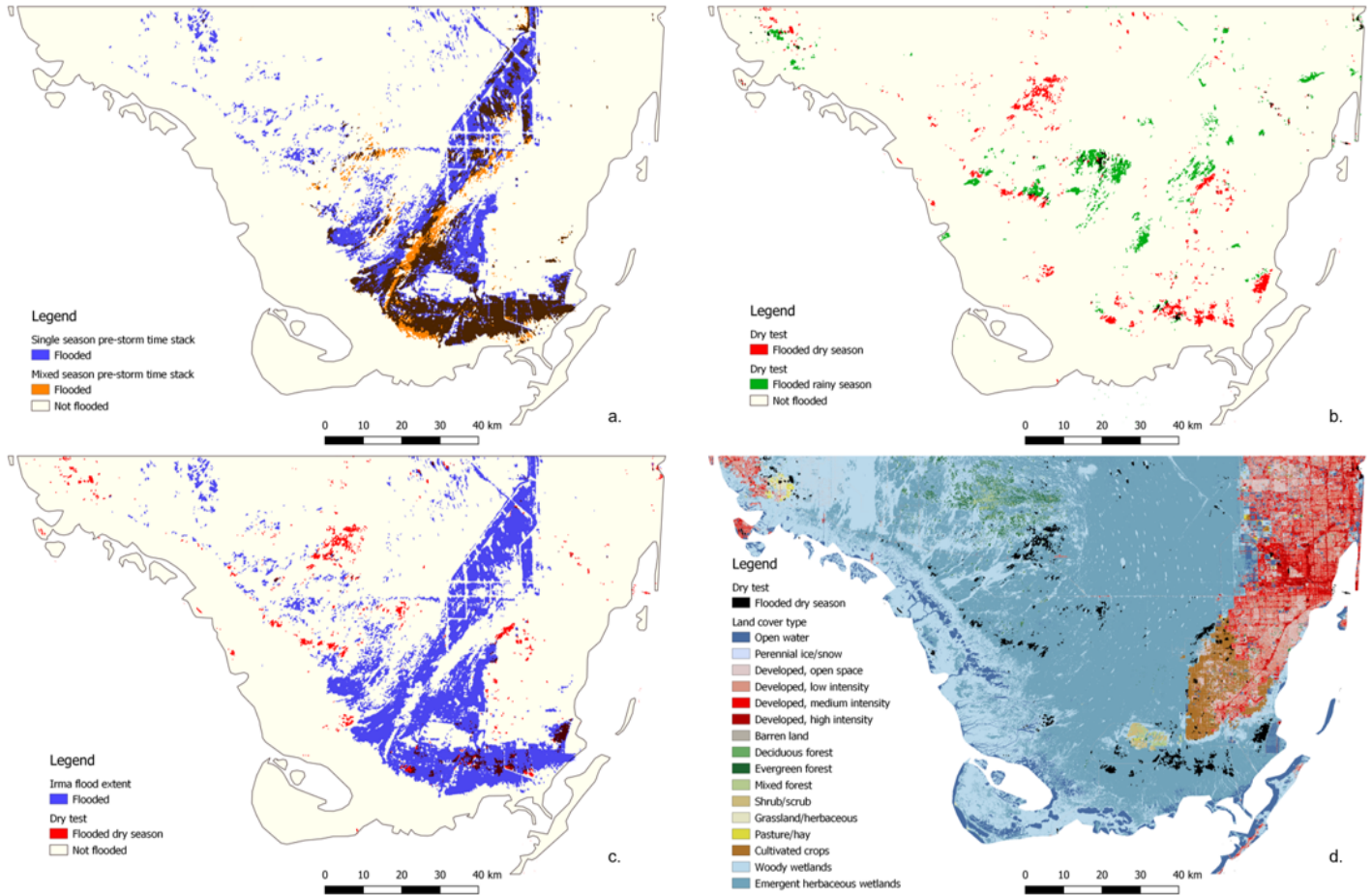


Figure 4.5: Overview of spatial flood patterns from seasonality- and dry tests. (a) Flood extents from using pre-storm images from only the rainy season (blue) and from using pre-storm images from both the rainy and the dry season (orange), showing a much smaller flood extent. The overlap between the two flood layers is shown in black. (b) Dry tests across 12 dates with no reported flooding between 2017 and 2019. Red indicates detections during the dry season, green during the rainy season; areas with overlap are shown in a darker colour. (c) Flood extent from the dry tests in the dry season (red) and the SAR-derived flood extent following Hurricane Irma (blue), overlapping areas are black. (d) Land cover map of the study area displaying various land cover classes, overlaid with the flood extents from dry tests in the dry season, shown in black.

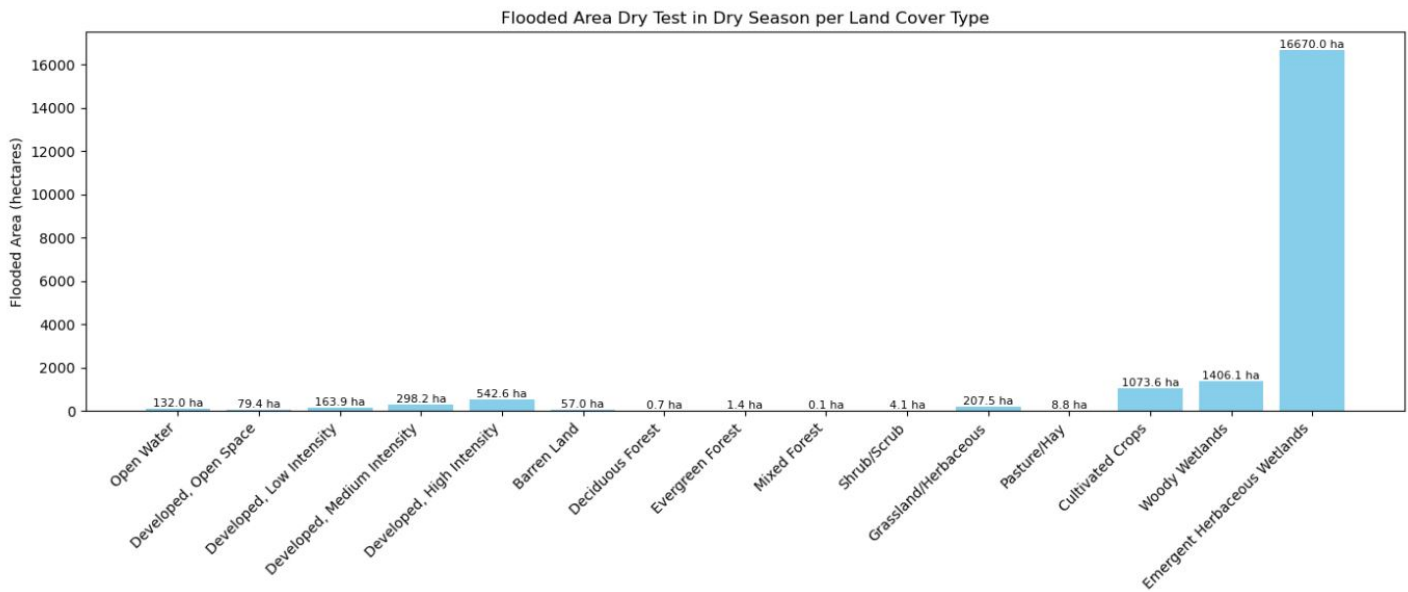


Figure 4.6: Histogram showing the hectares flooded in the dry test of the dry season per land cover type

4.3.3. Specific model settings

The performance of flood detection is influenced by key processing parameters. These settings aim to balance capturing actual flooding while minimizing noise. Optimal settings vary depending on factors such as the intended scale of the analysis. The model parameters were refined through an iterative trial-and-error approach, also guided by the dry testing described above. The final model settings applied on the Everglades during Hurricane Irma are summarized in Table 4.3.

Table 4.3: Summary of refined model settings for flood detection in South Florida after Hurricane Irma

Setting	Value	Justification
Polarization	VV	More accurate than VH
Passing direction	Ascending	Coincided with landfall of Irma
Smoothing radius	200 m	Reduced speckle noise
Water body removal	9 months	Excluded permanent water
Flood threshold	1.35	Minimized false positives
Small pixel removal	50 pixels	Reduced noise

Polarization choice

For this analysis, VV polarization (vertical transmit, vertical receive) was selected over VH polarization (vertical transmit, horizontal receive). Both options were tested, but VH detected almost no flood extent (only 6046 hectares) and did not correspond with flood reports in literature (NOAA, 2017; Zhang et al., 2018). This choice for VV polarization is also supported by the research of Zhang et al. (2018), who used VV polarization for this area of interest.

Satellite passing direction

The analysis uses ascending orbit data, meaning the satellite captures images as it moves from south to north during its pass. Using data from the same passing direction, pre- and post-storm, is important to ensure comparability, as different viewing angles may capture surface features differently. In this case study, the ascending satellite pass coincided with the day of Hurricane Irma's landfall and was therefore used for both the pre- and post-storm imagery.

Smoothing radius for speckle noise reduction

A smoothing radius of 200 meters was applied to reduce speckle noise in the radar imagery. Initially, a 50-meter radius, similar to the UN-SPIDER (2025) standard, was tested. However, this proved in-

sufficient in reducing speckle noise, as large numbers of flood pixels appeared in similar locations in both storm and dry tests, suggesting potential false positives. The smoothing radius was gradually increased through trial and error, eventually reaching 200 meters, at which point the scattered noise was much reduced while still preserving the main flood patterns. The trade-off of a high smoothing radius is the risk “over-smoothing”, where smaller flood features may be lost. However, given that this study focuses on rather large-scale flood events, this choice was seen as acceptable.

Permanent water body removal

A 9-month threshold was applied to mask permanent water bodies from flood detection. This means that any area classified as water in the JRC Global Surface Water dataset for more than 9 months per year is excluded from the detected flood extent. This step ensures that persistent water bodies, such as lakes and rivers, are not mistakenly classified as flood events.

Change detection threshold setting and sensitivity analysis

To evaluate the impact of threshold selection on flood detection, a sensitivity analysis was conducted by varying the threshold values used for change detection in backscatter. In this sensitivity analysis, threshold values of 1.05, 1.15, 1.25, 1.35, 1.45, and 1.55 were tested.

A lower threshold means that even a small change in backscatter between the pre-flood and post-flood images is sufficient for a pixel to be classified as flooded. While this increases the number of detected flood pixels, it also raises the risk of false positives. Conversely, a higher threshold requires a larger change in backscatter, reducing the likelihood of misclassification but potentially underestimating the flood extent. The detected flooded areas for each threshold are summarized in Table 4.4, and the corresponding flood maps are shown in Figure 4.7.

Based on the sensitivity analysis, the change detection threshold was chosen at 1.35, which is higher than the 1.25 standard used by UN-SPIDER (2025). A threshold of 1.25 resulted in a large number of scattered, noisy flooded areas. When examined in detail, including in the dry test analysis, it was observed that this lower threshold led to a higher number of potential false positives, likely capturing more backscatter noise. Increasing the threshold to 1.35 reduced these false positives while still delineating well-defined flood extents following Hurricane Irma. As shown in Figure 4.7, the 1.35 threshold maintains a clearly visible flood extent but with fewer patchy flooded areas compared to 1.25. It should be noted that the threshold value of 1.35 is relatively conservative, meaning that some actual flooding may not be detected with this setting. However, a stricter threshold was deliberately chosen to ensure a higher level of confidence in identified flood areas.

Table 4.4: Detected flooded areas for different change detection thresholds for Hurricane Irma in the Everglades

Threshold	Detected flooded area (hectares)
1.05	427,469
1.15	323,362
1.25	238,490
1.35	168,811
1.45	115,473
1.55	74,971

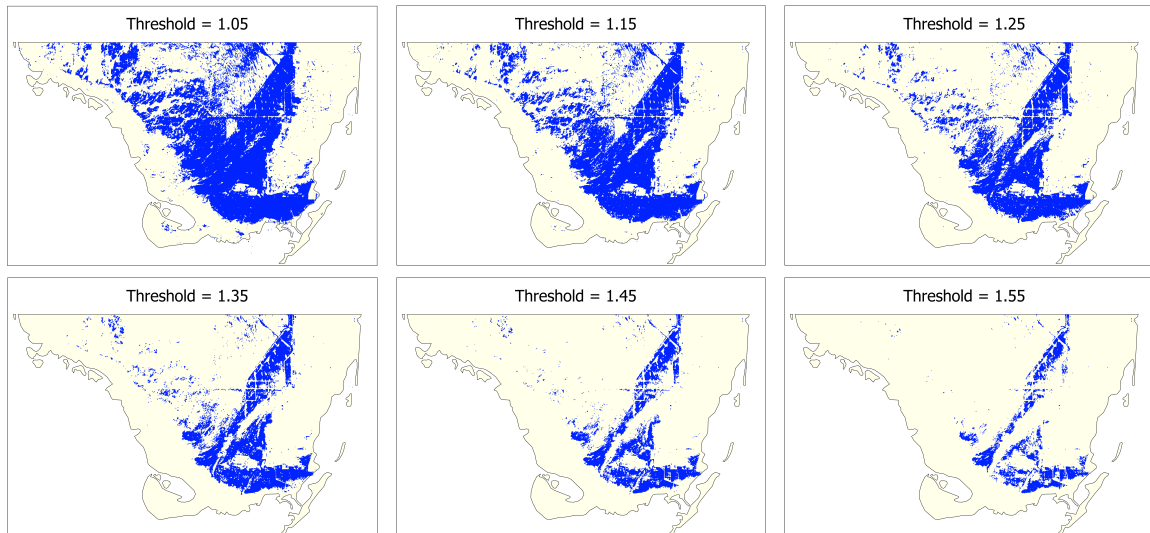


Figure 4.7: Sensitivity analysis of backscatter change detection threshold

Removal of small isolated flood pixels

A connectivity filter of 50 pixels (500 m) was applied to eliminate small, isolated flood pixels that were likely false detections. The default setting in UN-SPIDER (2025) (8 pixels) was insufficient, as speckle noise caused large numbers of small, scattered flood patches to appear, even in the dry tests. The value was progressively increased through trial and error, eventually reaching 50 pixels, where much of the speckle noise was removed while still retaining clear flood areas. This setting is justified given the scale of analysis, the objective is to detect large-scale flood events rather than small localized water bodies. Therefore, a higher connectivity filter helps focus on true flooding events rather than isolated noise.

4.3.4. Qualitative validation

A qualitative evaluation is performed as a first means of validation, between the SAR-derived flood map and two existing flood maps from literature, shown in Figure 4.8 and Figure 4.9. This comparison serves to justify the selected parameter settings and to explore the level of consistency or divergence with reported flood extents for the same event. This evaluation is summarized in Table 4.5, where the level of correspondence within three identified areas is ranked from low, to moderate, to high correspondence. The evaluation is elaborated on below.

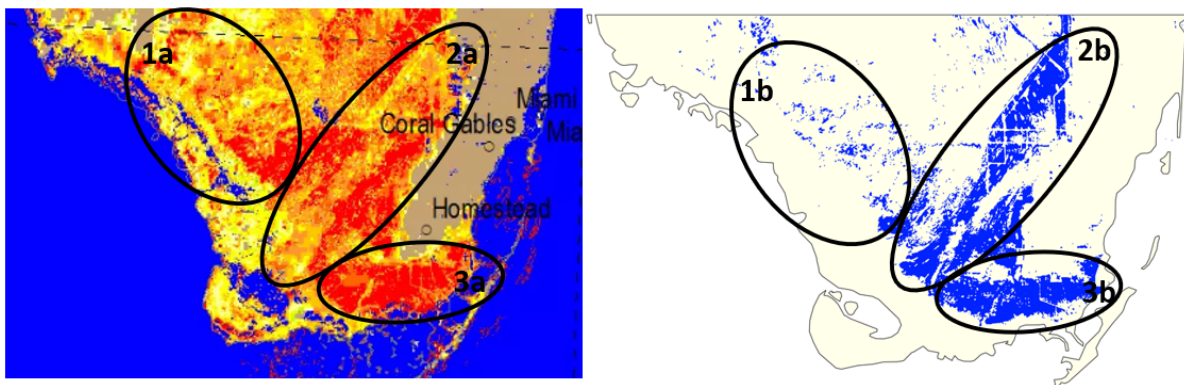


Figure 4.8: Comparison between the NOAA-derived flood map, NOAA (2017) (left), and the SAR-derived flood map (right) for Hurricane Irma in South Florida. Three areas (1, 2, and 3) are delineated to qualitatively assess similarities and differences in detected flood extent. In the NOAA map, colours represent the fraction of land covered by water, varying from green (less than 30%) to red (more than 90%).

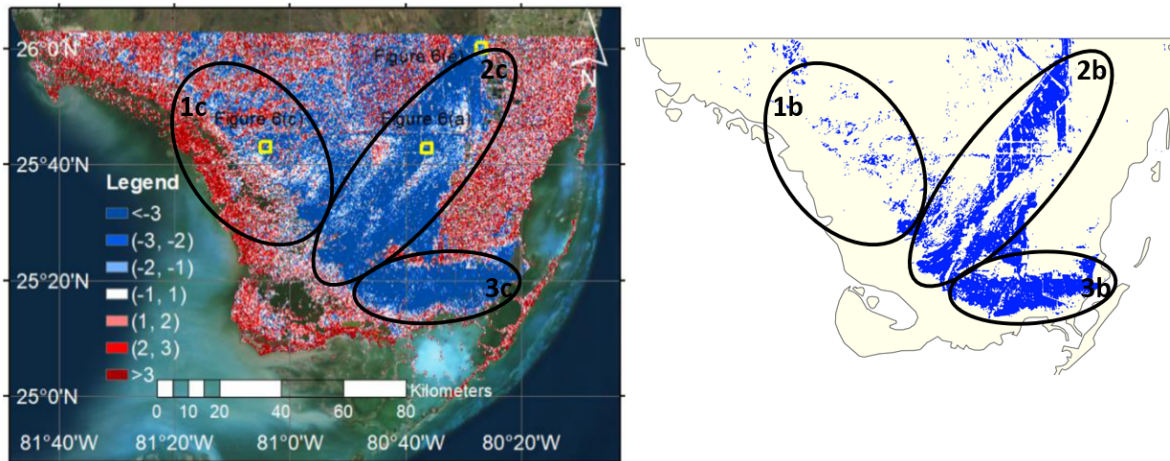


Figure 4.9: Comparison between flood map of Zhang et al. (2018) (left), and the SAR-derived flood map (right) for Hurricane Irma in South Florida. Three areas (1, 2, and 3) are delineated to qualitatively assess similarities and differences in detected flood extent. In the map by Zhang et al. (2018), blue indicates a decrease in backscatter, red indicates an increase in backscatter, and white represents areas where no flooding was detected or where flooding was not detectable.

The flood map from NOAA (2017), is derived from satellite observations by NOAA, which operates the satellites GOES-16 and Suomi NPP, using optical and infrared sensors (ABI and VIIRS) to monitor flooding, with spatial resolutions of 1 km and 375 m, respectively (NOAA, 2017). The NOAA data also differs in acquisition date, being captured on 11 September, one day after the SAR-based flood map. In Area 1, a clear difference is observed: the NOAA flood map 1a shows substantial flooding, including areas marked in red, indicating 100% flood coverage, and surrounding regions in yellow and orange, reflecting 50–80% flood coverage. In contrast, the SAR-derived map 1b indicates only small patches of flooding. In Area 2, the flood patterns between the two maps are more consistent, though the NOAA map appears to show slightly more flood extent than the SAR-derived map. In Area 3, there is strong agreement between the two flood maps, although the flood extent in the NOAA map extends further southward, into regions where mangroves are located. A notable discrepancy observed across all areas is the detection of flooding within the mangrove zones. The SAR-derived map shows no flooding in these areas, likely due to the backscatter signal from dense mangrove vegetation being stronger than the signal reflected from flooding, as these type of radar signals are unable to fully penetrate dense canopy cover. In contrast, the NOAA map indicates moderate flooding within the mangrove extent.

Secondly, the SAR-derived flood map is compared with the flood extent presented by Zhang et al. (2018). Zhang et al. (2018) used a combination of Sentinel-1 C-band data, the same data as used in the flood extent map developed in this study, and interferometric SAR (InSAR) techniques to map flooding. Their approach identified flooded areas through both decreased backscatter (shown in blue), occurring in low-vegetation zones, and increased backscatter (shown in red), likely resulting from the double-bounce effect in high-vegetation areas. A key observation from the comparison with Zhang et al. (2018) is the presence of a clearly defined blue flood extent, which largely resembles the overall SAR-derived flood map in spatial coverage. However, outside this main flooded area, the flood map by Zhang et al. (2018) displays a scattered distribution of white, red, and additional blue pixels. This part of the map appears rather noisy, with numerous isolated pixels. Regarding Figure 4.9, in Area 1, the map by Zhang et al. (2018) 1c, shows more extensive flooding than 1b, although it is intermixed with red and white pixels, indicating increased backscatter or undetectable areas. This spatial noise complicates interpretation, but it is evident that 1b represents a more conservative flood extent than 1c. In Area 2, the central flooded region in 2c resembles that in 2b in shape, although 2b appears narrower, likely due to a stricter threshold. A similar pattern is observed in Area 3, where the overall shapes of 3b and 3c are consistent, but the extent in 3c is slightly larger. Overall, the spatial alignment between the two sources is relatively strong. The larger flood extent in Zhang et al. (2018) may result from a less conservative classification. Moreover, the presence of red areas, indicating increased backscatter, suggests flooding in high-vegetation areas such as mangroves, which is not captured by the approach used in 1b, 2b, and 3b that relies solely on backscatter reduction.

Table 4.5: Qualitative evaluation of the SAR-derived flood map compared to existing flood maps from literature.

Source	Area	Level of correspondence	Main differences and possible explanations
NOAA (2017)	1	Moderate	NOAA (2017) shows substantially more flooding than the SAR-derived map. This may be due to conservative SAR thresholding and model settings, differences in spatial resolution (VIIRS: 375 m; SAR: 10 m), sensor type (optical vs. radar), and a one-day offset in acquisition date.
	2	Moderate	NOAA (2017) shows a slightly larger extent, with some high-flooded areas absent in the SAR map. Overall shape aligns well; differences may stem from SAR thresholding and differences in resolution and acquisition timing.
	3	High	Strong spatial agreement overall. The main discrepancy occurs in the most southern mangrove zone, where NOAA (2017) shows flooding not captured by the SAR-derived map.
Zhang et al. (2018)	1	Moderate	Zhang et al. (2018) displays more flood coverage with mixed signals from both increased and decreased backscatter. The SAR map is more conservative, using only backscatter decrease, yielding a smaller extent.
	2	High	Good agreement in the core flooded zones. The narrower extent in the SAR map likely reflects more conservative thresholding and model settings compared to Zhang et al. (2018).
	3	High	Overall, there is strong correspondence in the general flood outline, though the SAR-derived extent is smaller than that of Zhang et al. (2018), likely due to more conservative detection settings.

4.4. Application of conceptual guideline and remote sensing tool

With the model settings refined and qualitatively compared to flood maps from literature, this section proceeds to apply the conceptual guideline and the remote sensing tool to the case study. The approach follows the conceptual guideline step by step, using, where possible, the outcomes from the remote sensing tool. In cases where the remote sensing tool alone cannot provide information, literature is used to supplement the analysis. The numbers of the steps of the sections below correspond to the steps in the guideline, shown before in section 2.4.

4.4.1. Step 0: Flood extent

Figure 4.10 shows the flood extent following Hurricane Irma, detected using the remote sensing tool. Additionally, the mangrove extent and the storm track of Irma are added to the map for context. Some initial observations of the mapped flood extent, mangrove extent, and storm track are provided. A first inspection of the map reveals that a substantial portion of the case study area was flooded. The total flooded area within the area amounts to **168,811 hectares**, while the total mangrove extent within the area is **175,030 hectares**.

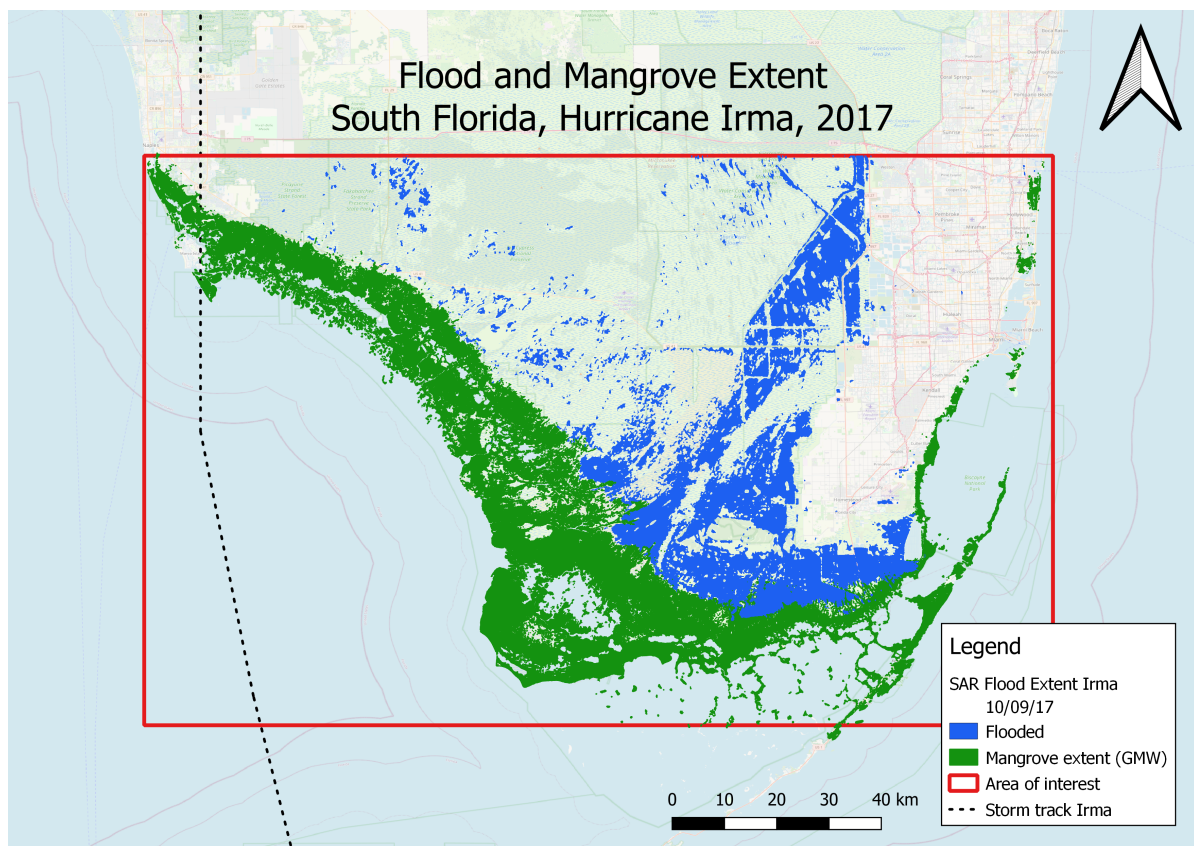


Figure 4.10: Map showing the flood extent detected following Hurricane Irma, as well as mangrove extent and Hurricane Irma's track.

The trajectory of Hurricane Irma, oriented from south to north plays a role as it determines where water is built up by the surge. While the mapped line in Figure 4.10 represents the center track of the storm, it is important to note that the area affected by high winds, waves, and storm surge extends beyond the immediate vicinity of this line. As shown in the Appendix in Figure C.3, the high wind speeds in the broad area surrounding the storm center affected the entire case study region, indicating that Hurricane Irma's track had an impact across a wide radius. So, even though the storm's eye did not pass directly over much of the case study area, the region still experienced major impacts. As such, the southwestern coast of Florida, closest to the storm's strongest wind fields, experienced high surge levels.

Another observation that can be made from Figure 4.10, is a grid-like pattern in the upper portion of the detected flood. This most likely reflects the influence of a nearby road and a network of human-made canals located within the Water Conservation Area. These canals segment the area into straight sections. Due to their permanent water presence, the canals exhibit no change in radar backscatter between pre- and post-flood imagery, and thus are not classified as flooded using the applied change detection method. The remaining flood extent is examined in detail through the further steps of the conceptual guideline.

4.4.2. Step 1: Identification of the coastal type

Based on the classification by Worthington, Zu Ermgassen, et al. (2020), the area of interest is identified as a lagoonal mangrove coast. This classification entails the presence of a shallow coastal shelf with a surrounding barrier system. The region's shallow bay has the ability to enhance storm surge. The presence of the barriers provides protection from wave action, creating rather calm wave conditions within the lagoon and in the mangrove forest. In addition to these marine aspects, the area also receives freshwater inflow, where drainage patterns show water flowing from the inland areas toward the southern coast (National Park Service, 2025a).

4.4.3. Step 2: Determination of the dominant hydrodynamic forcing

To determine the dominant hydrodynamic forcing contributing to the flood, storm surge height and wave conditions reported in literature are discussed, alongside a precipitation assessment based on the remote sensing tool.

Regarding surge, Lagomasino et al. (2021) reported that storm surge was a major driver of flooding during Hurricane Irma in South Florida. Cangialosi et al. (2021) documented storm surge heights ranging from 1.8 to 3.1 meters along the southwestern coast, as shown in Figure 4.11. Considering short waves, a map of significant wave height during Hurricane Irma, generated by ESA using Sentinel-1 radar data (see Figure C.4) shows that wave heights near the case study area remained below approximately 2.5 meters (ESA, 2017). Although the mapped area only partially overlaps with the case study region, the highest wave heights during Irma are clearly observed near Cuba, not along the Florida coastline. Similarly, Musinguzi et al. (2022) report that on the west coast of South Florida, the contribution of waves to the total water level is limited. This is primarily attributed to the presence of a wide continental shelf and a protected barrier system, which reduce significant wave heights along the western coast (Musinguzi et al., 2022). Therefore, it is likely that, mainly due to the sheltered coastal configuration, wave height added relatively less to the total water level than storm surge in this region during Hurricane Irma. Therefore, in the following steps of the conceptual guideline, the path is selected when surge is dominant over short waves in causing the flood extent.

In addition to coastal forcing, precipitation is considered as driver of the detected flood extent. Reports indicate that major precipitation occurred throughout Florida leading up to and during Hurricane Irma (Cangialosi et al., 2021). Most likely, the dominant drivers of flooding in the study area were a combination of storm surge and precipitation (Zhang et al., 2018). The contribution of precipitation is further touched upon in the following precipitation analysis. It is necessary to determine which parts of the detected flood extent resulted from precipitation and which were caused by storm surge, as only the latter can be influenced by mangroves.

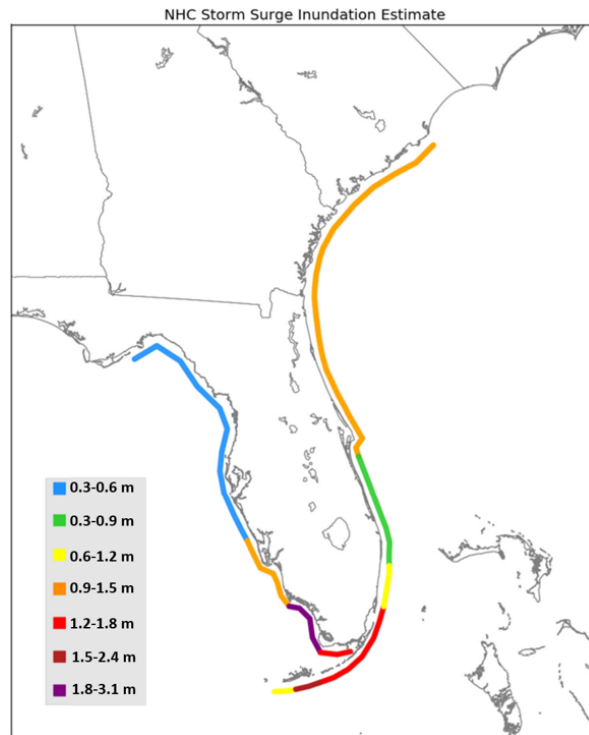


Figure 4.11: Storm surge height along the coast of Florida during Hurricane Irma (2017), measured in meters above ground level. The highest recorded surge occurred in the southwestern part of the state, where extensive mangrove forests are located, with inundation levels reaching 1.8-3.1 meters (Cangialosi et al., 2021).

Precipitation analysis

To further explore the drivers of the detected flood, the remote sensing tool is used to create a precipitation map in combination with an elevation map. This allows for an assessment of possible connections between rainfall accumulation and the locations where flooding was detected. Figure 4.12a presents cumulative precipitation over the six days preceding and including Hurricane Irma's landfall (September 5–10, 2017). Higher cumulative precipitation values, indicated in red, are concentrated in the northern and northeastern regions, whereas the southwestern areas, including much of the Everglades National Park, show relatively lower rainfall totals. The cumulative precipitation over this period ranged from a minimum of 34 mm to a maximum of 113 mm. A hotspot precipitation map, shown in red in Figure 4.12b, is created, highlighting areas where cumulative rainfall exceeded 75 mm. This threshold was selected as an estimate for conditions that could contribute to detectable flooding. It should be noted that this value represents a rough approximation, as various factors, such as soil saturation, substantially influence the amount of precipitation required to trigger flooding. The resulting hotspot map was then overlaid with the SAR-derived flood extent, shown in pink, in Figure 4.12b. Furthermore, the elevation of the study area is considered, as it influences water flow and accumulation, presented in Figure 4.12c. The elevation map is overlaid with the precipitation hotspot map and the SAR-derived flood extent in Figure 4.12d.

Figure 4.12c illustrates the predominantly flat terrain of South Florida. The flood extent appears to be largely confined to the lower elevation zone. In contrast, the areas identified as precipitation hotspots are mostly located at higher elevations. Reasoning from the maps of Figure 4.12, it is quite likely that precipitation in the hotspot areas drained toward the lower-lying regions where flooding was detected in the SAR imagery. The inland flooding in the detected flood map can likely be explained by precipitation runoff. The current drainage patterns in the region partly direct water southward towards the Everglades, where a portion of the detected flood extent is located. Since mangroves have a limited capacity to mitigate precipitation-induced flooding, the likelihood that they reduced the flood extent in the inland areas is therefore minimal. It remains uncertain to what extent coastal flooding contributed to the observed flood extent and whether it was influenced by mangroves. This is further explored through an analysis of elevation using the bathtub inundation model.

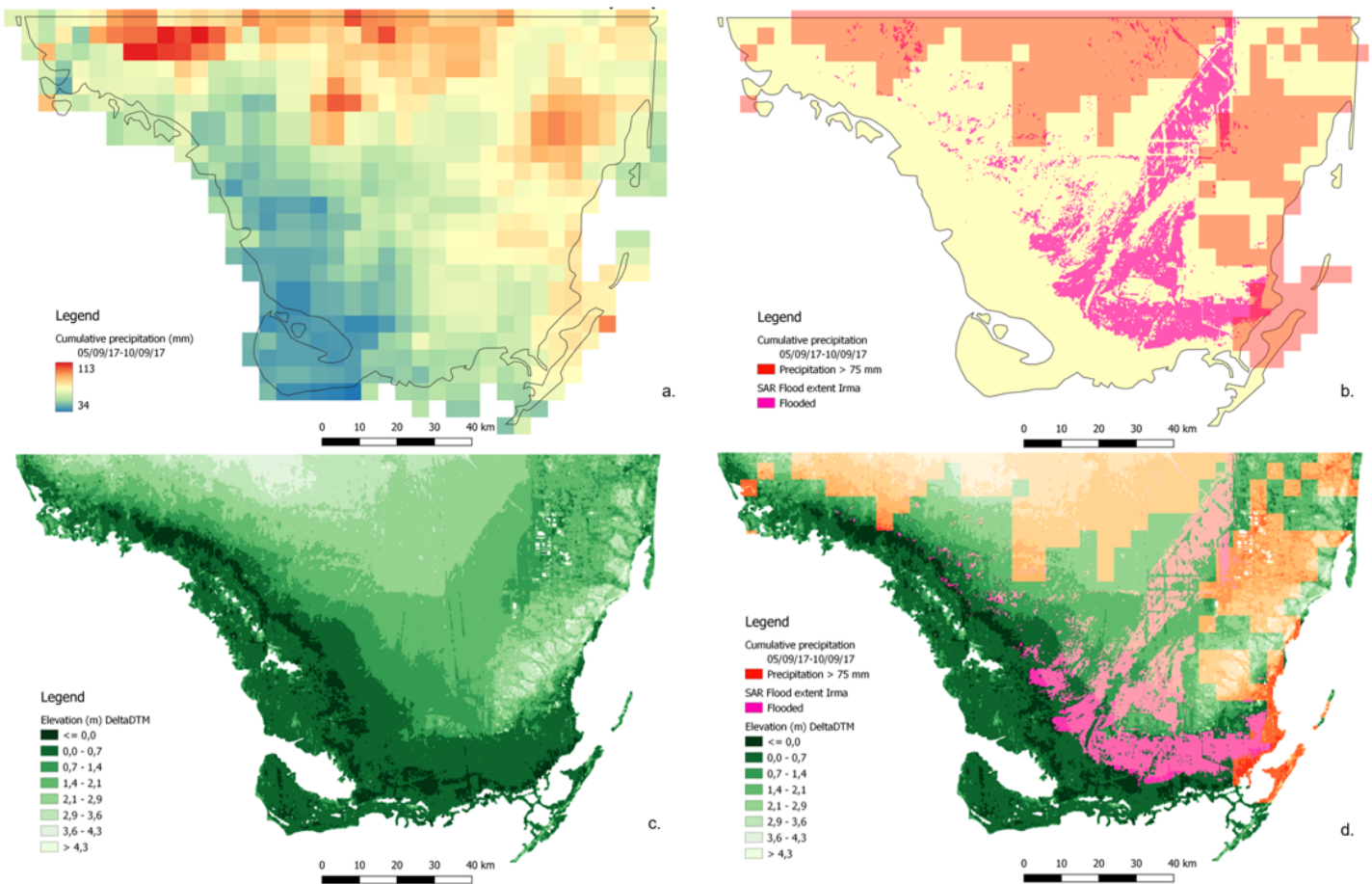


Figure 4.12: Precipitation, flood extent, and elevation in the area of interest for Hurricane Irma. (a) Cumulative precipitation (in mm) from 5 to 10 September 2017, leading up to landfall of Hurricane Irma. (b) Precipitation hotspot areas (red) exceeding 75 mm, derived from panel (a), overlaid with the SAR-derived flood extent on 10 September 2017 (pink). (c) Elevation map of the study area, derived from DeltaDTM (Pronk et al., 2024). (d) Combined visualization of the precipitation hotspot map and SAR-derived flood extent over the elevation map, allowing for spatial comparison between rainfall, flood, and topography.

Elevation analysis

To further explore which elements of the SAR-detected flood could have been caused by coastal flooding, a comparison is made between a SAR-derived flood extent and a bathtub inundation model flood extent. This serves also to explore whether there are indications of a potential relationship between flooding and the presence of mangroves.

Table 4.6 presents the flood extents in the bathtub inundation model for water level thresholds of 1, 2, 3, and 4 meters above MSL, visualized in Figure 4.13. These water levels were selected to simulate how the area would respond to progressively increasing flood stages within the area. In Figure 4.14, the flood extent derived from the bathtub inundation model for a 1-meter water level is compared to the SAR-detected flood extent. This 1-meter water level was selected for comparison, representing a safe estimate, as reported surge heights along the mangrove forest ranged between 1.8 and 3.1 meters at their peak. In the comparative map (Figure 4.14), three distinct areas are identified: Area 1 exhibits partial overlap between the SAR-derived and bathtub flood extents; Area 2 is characterized by flooding almost only in the SAR-derived map; and Area 3 shows near-complete agreement between both flood extent maps. Additionally, a map overlaying the road network with the two flood extents is included to account for potential physical barriers in the landscape that may have impeded inland flood propagation, shown in Figure 4.15. This spatial context helps identify areas where the bathtub model may overestimate flood extent due to its exclusion of such constraints.

Table 4.6: Comparison of flooded areas (ha) for different water levels in the bathtub model.

Water level in Bathtub model (m)	Flooded area (ha)
1	422,478
2	751,340
3	1,056,959
4	1,142,191

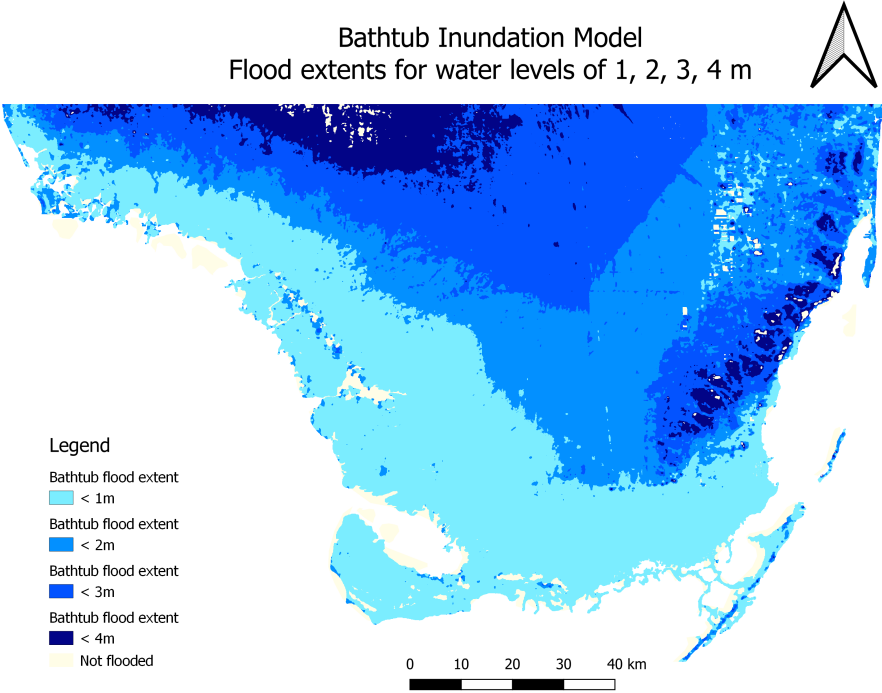


Figure 4.13: Bathtub inundation model flood extents for water levels of 1, 2, 3, and 4 meters above mean sea level (MSL), depicting inundation based purely on elevation.

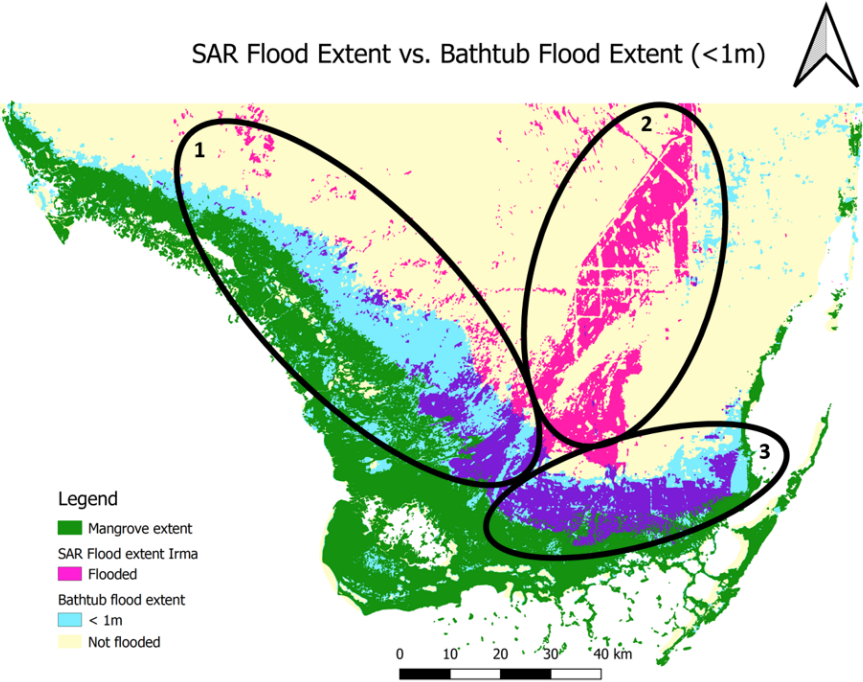


Figure 4.14: Flood extent comparison between SAR flood model and bathtub inundation model at 1m water level. The three circles entail three different areas which are examined. The SAR-derived flood extent is presented in pink, the bathtub model in blue, with areas of overlap between the SAR flood extent and the 1m bathtub model flood depicted in purple.

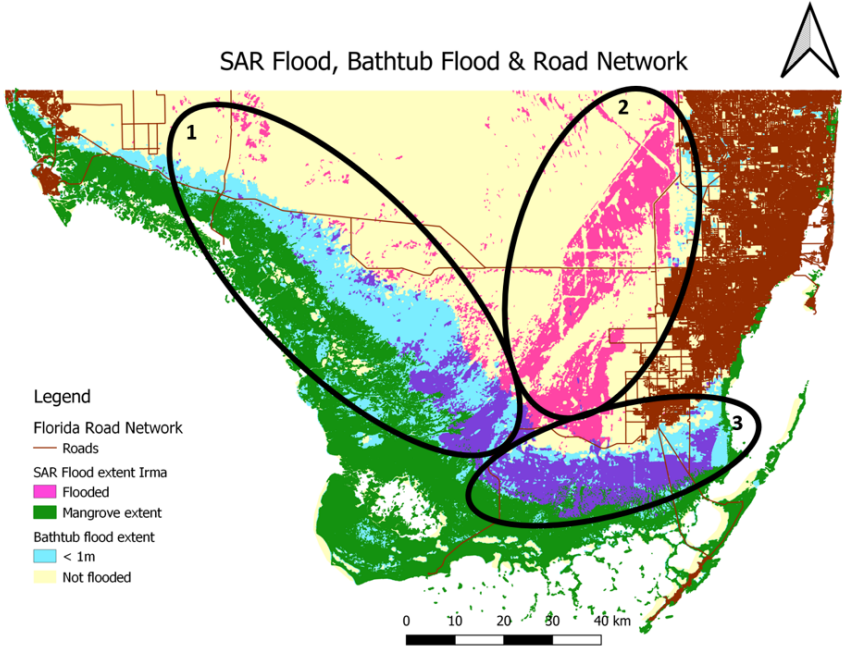


Figure 4.15: The road network is added to the flood extent comparison between the SAR derived flood extent and the bathtub model flood extent, as roads can be an indication of physical barriers.

4.4.4. Step 3A: Hydrodynamic variables

Surge height

As reported by Cangialosi et al. (2021), the southwestern coastline of the study area experienced storm surge heights ranging between 1.8 and 3.1 meters during Hurricane Irma. These values indicate high water levels, suggesting that a large portion of the mangrove forest was likely inundated. Given the low tidal range in the area, the observed storm surge height is relatively high. According to the conceptual guideline, mangroves attenuate lower storm surges more effectively, as then the surge energy interacts more with the structurally robust root systems. In this case, tree heights ranged from 4 to 18 meters, meaning that for shorter trees, not only the roots but also the stems, branches, and leaves were likely submerged during the event. While mangroves attenuate surge energy most effectively when flow is at their root level, higher water levels result in flow through more flexible vegetation components such as branches and leaves, which may reduce overall attenuation rates. Consequently, the surge height in this region may have limited the mangrove forest's reduction of flood extent.

Forward speed of the storm

The forward speed of a storm plays a role in the effectiveness of mangroves in attenuating storm surge. During previous storm events in the Everglades, Zhang et al. (2012) compared forward storm speeds of 11.2 m/s (fast-moving) versus 2.2 m/s (slow-moving) through the mangrove forest, showing that the slower-moving storm allowed for much more inland surge propagation and subsequent flooding compared to the faster moving storm, which was better attenuated by the mangroves.

In the case of Hurricane Irma, the estimated forward storm speed as it passed over the Everglades was approximately 3.6 m/s (Mersmann, 2017). When compared to the values mentioned by Zhang et al. (2012) in the same study area, this places Irma rather on the lower side in terms of forward storm speed, meaning that the surge may have been able to travel far inland, with a reduced attenuation rate due to the storm's relatively slow forward speed.

4.4.5. Step 4A: Ecological variables

Biomass and zonation

The spatial distribution of above-ground biomass is presented in Figure 4.16. As outlined in the conceptual guideline, above-ground biomass serves as a proxy for both the overall forest density and the structural complexity of individual trees, including the density of their root, stem, branch, and leaf systems. Increased roughness, introduced by these mangrove structural elements, dissipating energy from the surge, reducing its momentum and thereby slowing its inland propagation. This deceleration contributes to a reduction in peak water levels, which in turn may result in decreased flood depths and, ultimately, a smaller flood extent.

One clear observation is that above-ground biomass varies across the mangrove extent, with the highest biomass areas predominantly located along the seaward edge. This may reflect the dominance of pioneer mangrove species in this zone—species that exhibit higher biomass to withstand relatively greater wave exposure compared to inland mangroves. In the southwestern part of the study area, higher above-ground biomass along the seaward fringe suggests greater surge attenuation rates. This zonation of higher biomass on the seaward edge of the forest is favourable for storm attenuation rates as the attenuation of storm surge is the highest on the seaward boundary of the mangrove forest compared to areas further inland of the forest (McIvor et al., 2012b; Zhang et al., 2012).

In the southernmost part of the study area, biomass values appear particularly lower. The lower biomass in this zone likely indicates limited surge attenuation, which may result from either lower individual tree density, the presence of less structurally developed or different mangrove species, or a more sparsely distributed forest. In such cases, the vegetation applies less roughness to the surge, allowing greater water movement through the forest and therefore less flood reduction.

Forest width

To gain a general sense of the spatial scale of the mangrove forest in the study area, forest width was estimated at a location using QGIS. At this location, both the width of the high-biomass mangrove zone on the seaward side and the full width of the mangrove forest, from the seaward edge to the most landward presence, were measured, perpendicular to the coast. This location is shown in Figure 4.16.

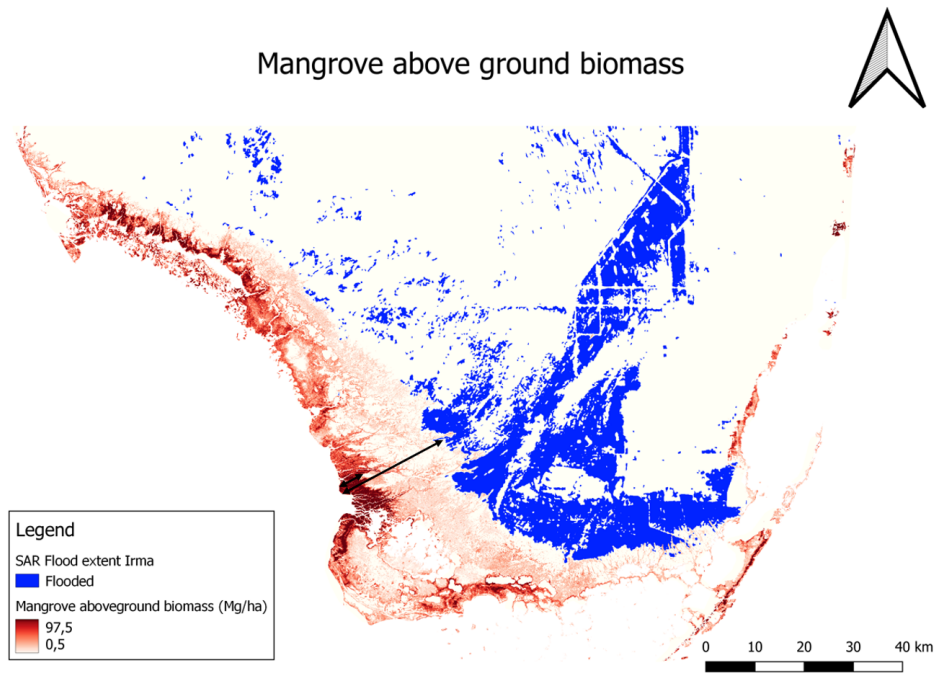


Figure 4.16: Mangrove above-ground biomass (Mg/ha) in the case study area. The two black arrows within the mangrove area indicate the locations where forest width is measured. The shorter arrow represents the width of the high-biomass mangrove zone, approximately 6 km, while the longer arrow reflects the total mangrove forest width, measuring around 25 km.

It is important to note that these measurements are intended only to provide an approximate order of magnitude. Developing a dedicated algorithm for mapping mangrove forest width is beyond the scope of this study.

The measured transects indicate mangrove forest width of approximately 6 km in the area with high biomass, and approximately 25 km for the full forest width Figure 4.16. Zhang et al. (2012) reported attenuation rates ranging from 40 to 50 cm/km in dense mangrove stands in the Everglades, based on field observations and numerical modelling of Hurricane Wilma, a previous hurricane event. Taking the attenuation rate of 50 cm/km for dense mangrove zones, a 3-meter storm surge would require approximately 6 km of forest width to be attenuated. The measured width of the high-biomass mangrove zone aligns well with this estimate, suggesting that, at least locally, the forest may provide sufficient width for surge attenuation.

In areas with lower biomass, characterized by a mixture of mangroves and open water, Zhang et al. (2012) documented a lower attenuation rate of 20 cm/km. Based on this rate, attenuating a 3-meter surge would require a minimum forest width of around 15 km. The measured width of the total mangrove forest, approximately 25 km, falls within this demand, further indicating that the forest width in the study area is within the correct order of magnitude to be able contribute to surge reduction.

The attenuation rates reported by Zhang et al. (2012) were deemed appropriate for use in this context, as they were calculated specifically for the Everglades region. Applying rates from other locations would be less reliable due to the sensitivity of surge attenuation to local factors such as elevation and vegetation structure. However, as the reported values were derived from a different storm event (Hurricane Wilma) they may reflect conditions specific to that event (like storm direction and forward speed) rather than Hurricane Irma.

While the mangrove forest width was measured perpendicular to the coastline, it is important to recognize that this may not fully capture the actual path of storm surge propagation. Given that the direction of the storm influences the orientation of surge movement through the forest, the effective distance traveled by the surge could differ from the measured perpendicular width.

4.4.6. Step 5A: Geomorphological variables

Coastal slope

As is characteristic of a lagoon-type coast, the bathymetry around the Everglades consists of shallow bays and a gentle slope. Tanaka (2008) suggests that a mild coastal slope of 1:500 is more effective for storm surge attenuation compared to a steeper slope of 1:100. Comparing these slopes to the Everglades, Stabenau et al. (2011) reported that the Everglades National Park mangrove region has an average elevation gradient of 5 cm per kilometer, equating to a slope of approximately 1:20,000. Examining the elevation data in Figure 4.12c, the expected pattern emerges: the mangrove belt along the southwestern coast is situated at low elevations, characterized by very gentle gradients. Given that a 1:500 slope has already been demonstrated to enhance surge attenuation relative to 1:100, the much lower gradient of the Everglades means that the coastal slope is favourable for storm surge attenuation.

Presence of channels and ponds

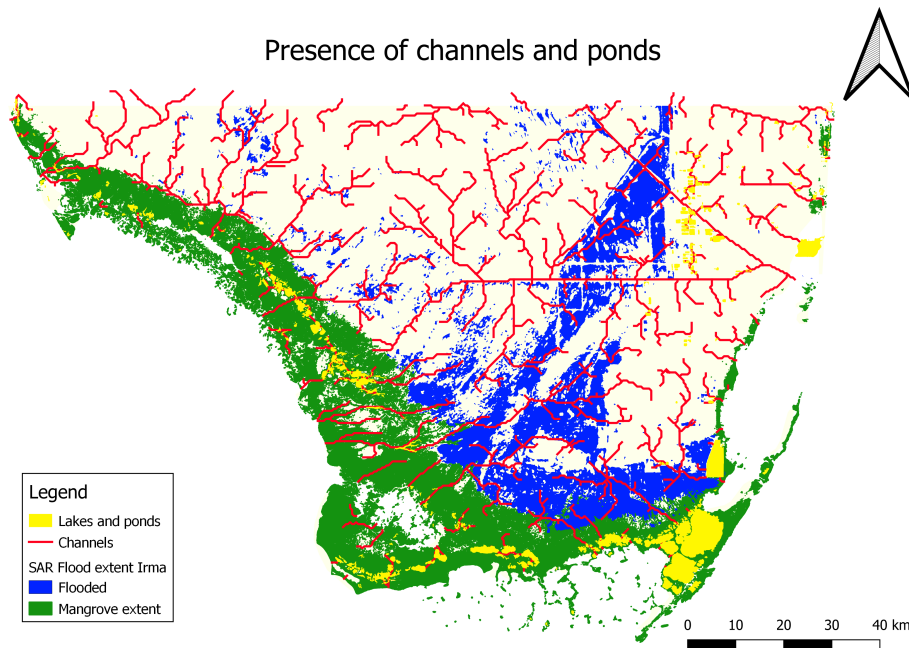


Figure 4.17: Presence of channels and ponds in the case study area. The red lines represent channels, while yellow areas indicate lakes and ponds.

Finally, the presence of channels and ponds in the case study area is considered, as shown in Figure 4.17. The mangrove belt along the southwestern coastline exhibits a range of ponds. Additionally, a variety of channels are visible within the mangrove area. As outlined in the conceptual guideline, the presence of channels and ponds reduces the capacity of mangroves to attenuate storm surge. Instead of being forced to pass through the mangrove forest, the surge propagates along these lower-resistance pathways, which reduces the frictional influence of the mangroves. As a result, the surge is less attenuated, allowing for greater water exchange and increased flood depth and extent. The clear presence of channels and ponds imposes limitations on the potential of mangroves to influence flood extent during Hurricane Irma.

4.5. Case study interpretation

Following the testing and refinement of the remote sensing tool and the application of the conceptual guideline to the case study, a synthesis of these elements is provided in this section. Walking through the branches of the conceptual guideline reveals that the case study area, classified as a lagoonal mangrove coast, experienced extensive flooding, driven by the hydrodynamic forcings of storm surge and rainfall associated with Hurricane Irma. The high surge level and low forward speed of the storm

may have reduced the mangroves' flood attenuation capacity. Mangrove biomass was concentrated at the seaward edge of the forest, which is favourable in terms of zonation. Forest width measured on the southwest coast appeared sufficient to be able to attenuate the surge, and the flat coastal slope further supports surge attenuation. However, the presence of channels and ponds reduces the overall surge attenuation potential of the mangrove forest by offering lower-roughness pathways. When compared to the bathtub model flood extent, three distinct areas within the SAR flood extent were identified. Thanks to the remote sensing tool, used in combination with the conceptual guideline, it was possible to identify Area 1 as the zone with the highest potential for mangrove influence on flood extent reduction within the case study. The reasoning for prioritizing further investigation in this area, as well as the limited relevance of the other areas, is outlined below.

Area 1

Area 1 should be prioritized in future research, as the remote sensing analysis suggests it is the most likely location where mangroves influenced flood extent. In this area, the SAR-derived flood extent only partially overlaps with the bathtub-modeled flood extent. Reported storm surge heights along this portion of the coastline ranged from 1.8 to 3.1 meters, higher than the 1-meter water level applied in the bathtub model. This raises the question of why the bathtub model indicates flooding in areas where no flooding is detected by the SAR analysis. One possible explanation could be that either physical barriers or surface roughness caused by mangroves, both not included in the bathtub model, may have limited the inland propagation of the surge wave.

To consider potential physical barriers, the road network is included, as roads are often constructed alongside or on top of levees. The road network map is shown alongside the two flood extents in Figure 4.15 and also shown separately in Figure C.2. Thus, roads may serve as a proxy for levee presence. In Area 1, like in the other areas, there are very few roads. While levees may exist without associated roads, there appear to be limited substantial physical barriers that would explain the difference between the bathtub flood and SAR flood in Area 1. The roughness applied by the mangrove vegetation may have reduced the energy and therefore propagation speed of the surge, limiting inland water exchange, leading to decreased flood depth and, subsequently, reduced flood extent in Area 1 in the SAR flood extent. The mangrove forest width, above-ground biomass, and zonation in Area 1 are favourable for attenuation. As the bathtub model does not account for roughness, this could be an explanation for the differences in flood extent, pointing to a notable influence of mangroves on flood reduction in Area 1. Alternatively, the discrepancy observed in Area 1 between the two flood extents may be attributed either to under-detection by the SAR-based method—stemming from conservative threshold settings that potentially excluded actual flooding—or to overestimation by the bathtub model, which does not account for other hydrodynamic processes such as drainage that, in reality, may have allowed floodwaters to recede from the area.

Area 2

Area 2 is considered less relevant for further investigation into mangrove–flood interactions. Here, the bathtub model does not indicate much flooding, while the SAR flood extent is clearly present. As discussed, it is plausible that this flooding resulted from precipitation accumulation rather than coastal flooding, with runoff collecting in lower-lying areas. The complete lack of overlap between the two flood models may suggest that this area of the SAR flood is attributable to precipitation-driven inundation. Furthermore, as shown in Figure 4.15, a road runs through the middle of Area 2 and another road is located below it, in Area 3. This southern road and its accompanying levee could act as a physical barrier that prevents surge, approaching from the south, from reaching the flood zone in Area 2. The road bisecting Area 2 further reduces the possibility that the northern portion of this area was affected by coastal flooding. These observations support the insight that flooding in Area 2 was primarily driven by precipitation. As mangroves have very limited influence on fluvial or pluvial flooding, Area 2 lies outside the spatial range of mangrove effectiveness.

Area 3

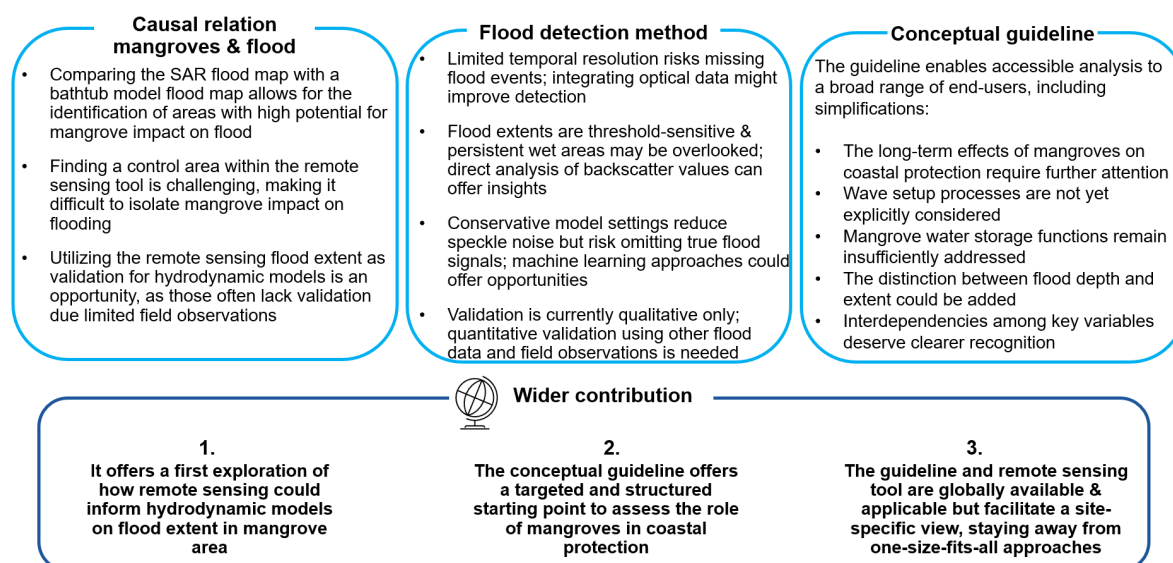
Area 3 is also unlikely to exhibit a substantial influence of mangroves on flood extent. The SAR-detected flood extent and the bathtub model flood extent exhibit almost complete overlap, which could mean that this area consists of mainly coastal flooding. If mangroves had meaningfully lowered the speed of the surge wave, a noticeable difference between the two flood extents would be expected. The similarity between the SAR-derived flood map and the bathtub inundation model, which does not account for

friction, suggests that mangroves had little attenuating effect in this area. Regarding the road network, Figure 4.15 shows that only a limited number of roads intersect the area covered by the bathtub flood extent, suggesting minimal obstruction to flood propagation in reality. In the northern part of Area 3, a road curves southward, which could potentially act as a flood barrier. However, both the SAR-derived and bathtub flood extents do not extend beyond this road, indicating that it likely did not influence flooding in this location. This lack of impact of mangroves on the flood may be attributed to the relatively low above-ground biomass in this section of the forest, implying sparser tree and root density. As a result, the friction exerted on the incoming surge is quite minimal, allowing the surge to propagate inland with limited resistance. Additionally, the forest width in Area 3 is considerably narrower than in Area 1. A wide mangrove belt is required to reduce surge given the long wavelength of storm surges.

Wrapping up, the remote sensing tool, combined with the conceptual guideline, proved effective in mapping flood extent and identifying areas with potential mangrove influence on flood extent in the case study. By integrating key variables, the approach highlighted Area 1 as the most promising location for further research on this matter. This demonstrates the added value of remote sensing in providing spatial flood extent data, which can help to inform numerical models. It supports a targeted research strategy by indicating where in-depth field and modeling efforts should be focused. As shown in the Everglades case, remote sensing offers an efficient starting point for assessing flood extent and mangrove contributions to coastal flood mitigation following tropical storms.

Discussion

Discussion overview



This study identified two gaps in the current understanding of the role of mangroves in coastal flood reduction under tropical storms: a knowledge gap concerning which variables influence flood extent reduction by mangroves, and a methodological gap in mapping flood extent due to limited validation data in mangrove regions.

To address the first gap, a conceptual guideline was developed to structure the key variables influencing flood reduction by mangroves, which mitigate flooding by slowing surge propagation, dissipating short wave energy, and storing water. The guideline first accounts for coastal typology (open coast, estuarine, lagoonal, deltaic), hydrodynamic forcing (surge, waves, precipitation), hydrodynamic characteristics (surge height, wave height, wave period, storm speed, water depth), ecological parameters (forest width, biomass, zonation), and geomorphological features (slope, channels).

To address the second gap, a remote sensing tool was developed in Google Earth Engine, making use of a change detection method using Sentinel-1 Synthetic Aperture Radar C-band data, which detects flood extent and visualizes relevant variables (mangrove extent, mangrove biomass, storm track, elevation, precipitation, and presence of channels) using globally available earth observation datasets.

Applied to Hurricane Irma (2017) in the Everglades National Park in Florida, the tool successfully mapped a flood extent of 168,811 hectares in the case study area and enabled visual analysis of variables identified in the guideline. The dry tests and initial qualitative validation of the tool yielded satisfactory results, making the output of the remote sensing tool suitable for informing the conceptual guideline in this case study. The area was classified as a lagoonal mangrove coast, with storm surge and precipitation identified as the primary drivers of the observed flood extent. Three distinct zones were identified: Area 1 was likely dominated by coastal flooding; Area 2 was primarily influenced by

precipitation-induced flooding, therefore lacking mangrove interaction; and Area 3 was also likely affected mainly by coastal flooding. Based on the comparison between the SAR-derived flood map and the bathtub model, Area 1 was identified as having high potential for mangrove-driven flood reduction. In this area, the bathtub model indicated flooding, while the SAR data did not, despite high surge levels. This could suggest effective attenuation, likely due to favourable conditions such as wide forest extent, high mangrove seaward biomass, and a flat coastal slope. However, the presence of multiple channels and high surge levels may have reduced the surge attenuation capacity of the mangroves in Area 1. In contrast, Area 3 showed low potential for mangrove impact, with an almost complete overlap between the SAR-derived and bathtub-model flood extents. This area is characterized by low forest width and biomass, both critical for reducing surge propagation speed, and thus limited the reduction of water exchange with the hinterland.

The application of the remote sensing tool and the conceptual guideline in the case study demonstrated the valuable contribution of remote sensing as validation input for hydrodynamic models and by identifying a high-potential area for mangrove influence on flood extent. It therefore provides both flood extent data and spatial prioritization to inform and guide subsequent numerical modeling efforts. Having covered the key findings, the following discussion considers the main limitations of the approach and offers potential avenues for improvement. The limitations include the causal relationship between flood extent and mangroves, constraints associated with the flood mapping tool, and simplifications within the conceptual guideline. Finally, the wider usability and contribution of this research to the field is reflected upon.

5.1. Causal relation between flood extent and mangroves

A first limitation of the remote sensing tool is that, while it allows for the spatial quantification of flood extent, it does not allow for causal attribution of flood reduction to mangrove presence. The observed flood patterns resulting from the remote sensing tool cannot be directly linked to the influence of mangroves without the use of a control area.

5.1.1. Comparison SAR- and bathtub model flood

An attempt was made to explore potential relationships between the flood extent and mangrove extent by comparing the SAR-derived flood map with a bathtub inundation model flood (Figure 4.14). In Area 1, the highest potential for mangrove impact on flood extent during Hurricane Irma was identified as the flood extent appeared to be primarily coastal-driven and was substantially smaller than the extent predicted by the bathtub inundation model.

However, alternative explanations for the difference in flood extents in Area 1 remain plausible due to uncertainties in both the SAR-derived and bathtub-modeled flood maps. The more limited extent in the SAR map may be attributed to conservative threshold settings and the exclusive use of backscatter decrease to detect flooding. Additionally, areas that are chronically waterlogged, common in wetland environments, may not appear as flooded in the SAR analysis if no major change in backscatter occurred between pre- and post-storm imagery. In the qualitative validation, Area 1 showed only moderate agreement with the flood maps from NOAA (2017) and Zhang et al. (2018), both of which indicated more flooding than the SAR-derived map, though with patchy extents. This discrepancy introduces uncertainty in the SAR flood map, suggesting that the observed differences with the bathtub model cannot be solely attributed to mangrove influence. Additionally, while almost no flooding in Area 1 during Irma overlapped with dry-season dry tests, many dry-test flood pixels appeared in locations not flooded during Irma. This indicates that the area, dominated by woody and emergent herbaceous wetlands, is prone to false positives, limiting the extent to which flood reduction can be attributed to mangroves alone. On the other hand, the bathtub model has its own limitations. While the limited presence of roads (used as proxies for levees) suggests minimal physical obstruction, the model does not account for drainage, other physical barriers, or water management infrastructure. As such, both flood maps carry inherent uncertainties that may explain the observed discrepancies apart from the presence of mangroves.

Uncertainties also exist in the classification of Area 2 as precipitation-driven and Area 3 as coastal flooding. Area 2 was labeled as precipitation-driven based on its proximity to precipitation hotspots, defined as areas receiving over 75 mm of cumulative rainfall in the six days leading up to Irma's land-

fall. However, this threshold is highly uncertain, as eventual flooding also depends on factors like soil moisture. A more detailed rainfall analysis should improve this assessment. Similarly, labeling Area 3 as coastal, based on its full overlap with the bathtub model, is limited by the fact that many false positives from the dry-season dry test also occurred in Area 3, primarily in emergent herbaceous wetlands. This raises doubts about the reliability of the flood signal in Area 3 and suggests that mangroves may have played a role after all. These uncertainties constrain the robustness of the current classification of Areas 2 and 3.

Therefore, the designation of Area 1 as a high-potential zone—and the exclusion of Areas 2 and 3 from further consideration of mangrove impact—is contingent upon several assumptions inherent in both the SAR-derived and bathtub-modeled flood maps. As such, a direct causal relationship between mangrove presence and observed flood extent cannot be definitively established. While the comparison of these two flood models provides valuable context, it does not support causal inference.

5.1.2. Control area

Including a control area in the remote sensing tool could offer possibilities for finding causal relations between mangroves and flood extent, yet finding such a control area turned out highly challenging. One option would be to compare flood events from two similar storms striking the same location, once with mangrove cover and once without, due to forest loss or regrowth. However, this is highly constrained by the rarity of identical storm tracks, as well as the limited time span of SAR satellite observations (Sentinel-1 since 2014). While mangrove degradation has occurred during this period, no suitable case was identified where an entire forest was lost between two comparable storms that would allow for such a control area. A second approach would involve comparing adjacent areas during the same storm, one with mangroves and one without. Yet this method is complicated by variations in elevation and geomorphology; mangrove forests are rarely bordered by uniformly structured non-mangrove areas, making direct comparisons unreliable. As such, while remote sensing is effective for flood extent mapping in mangrove area following tropical storms, it is currently not feasible to use it alone to isolate the specific contribution of mangroves to flood extent reduction.

5.1.3. Integration with hydrodynamic models

To overcome this limitation, remote sensing data should be combined with hydrodynamic models. Hydrodynamic models can simulate the physical processes of flooding and allow the effects of mangroves to be isolated, by switching 'on' and 'off' a roughness factor that accounts for mangrove presence. For example, Zhang et al. (2012) modelled the contribution of mangroves to surge attenuation during Hurricane Wilma (2005) in the Everglades. As mangroves are simplified to a set roughness coefficient, not accounting for different mangrove characteristics, Zhang et al. (2012) emphasize the importance of combining numerical models with observational data to validate the resulting flood extent. Another example is the study by Narayan et al. (2019), who modelled Hurricane Irma (2017) in the Everglades using a two-dimensional hydrodynamic model. Similarly to Zhang et al. (2012), mangroves were represented through a roughness coefficient. A no-mangrove scenario was included by assigning open-water friction values to the mangrove areas allowing for the isolated assessment of mangrove impact on flood extent (Narayan et al., 2019).

While these hydrodynamic models provide very useful insights and allow for extracting mangrove impact on flood extent, they are based on theoretical assumptions and face a major challenge of validating their resulting flood extents. Most hydrodynamic flood models have validation approaches that rely entirely on point-based measurements; Grimley et al. (2025) validate their SFINCS compound flood model against water level gauges. Similarly, Maymandi et al. (2022) evaluate their Delft3D-based compound flood model using tide gauges. These validation points are inherently limited in spatial coverage, and their reliability may be compromised by local sensor errors, maintenance gaps, or short data records. Moreover, such ground-based instrumentation is typically concentrated in populated and developed regions, potentially leaving many tropical coastlines, where mangroves are most prevalent, without adequate observational infrastructure for validation means.

This challenge in validating hydrodynamic models is precisely where the developed remote sensing tool demonstrates its added value. Remote sensing-derived flood maps can support hydrodynamic flood modeling in mangrove-dominated areas in two principal ways: (1) by identifying areas of interest

through comparison between the SAR-derived flood extent and the bathtub model output, thus indicating where numerical modeling efforts should be concentrated; and (2) by providing spatially continuous flood extent data for validation purposes. This targeted approach enables more efficient allocation of time and resources by avoiding unnecessary modeling in zones with limited potential for mangrove impact. Specific recommendations for actions in identified high-potential areas—including coupling with numerical models and additional field data collection—are detailed in chapter 7.

5.2. Flood detection method

Several limitations are inherent to the flood detection method presented in this study, including the satellite repeat cycle, the change detection technique, the sensitivity to threshold selection, modeling choices, and lack of quantitative validation.

5.2.1. Satellite repeat cycle

A key constraint lies in the timing of satellite overpasses. The Sentinel-1 satellite currently has a repeat cycle of approximately 12 days, as only Sentinel-1A remains operational since the deactivation of Sentinel-1B in 2022. Prior to that, with both satellites in orbit, the repeat cycle was about 6 days. This temporal resolution presents a challenge for flood mapping, as floodwaters can recede within a day. If the satellite overpass occurs more than a few days after the flood event, there is a high chance that floodwaters will have already drained, making the flood undetectable via SAR imagery.

In the case study of Hurricane Irma in the Everglades, the analysis benefited from the fortunate timing of a Sentinel-1 overpass coinciding with the day of landfall (10 September 2017). However, such alignment is quite rare. One potential solution is to supplement SAR observations with optical satellite imagery, such as Sentinel-2. While optical data is susceptible to cloud cover, it can offer complementary information when cloud-free scenes are available. This approach was demonstrated by Hamidi et al. (2023), who applied the Modified Normalized Difference Water Index (MNDWI) to detect floods in parallel with SAR-derived maps, enabling both validation and potential gap-filling when radar data was unavailable.

However, it remains highly questionable whether the use of optical remote sensing could substantially improve the temporal limitations currently faced as tropical cyclones are typically accompanied by extensive cloud systems. This constraint is emphasized in the work of Psomiadis et al. (2020), who utilized optical data solely for identifying permanent water bodies, but not for flood extent mapping and they identify cloud cover as the most important barrier in flood mapping using optical remote sensing. Similarly, Uddin et al. (2019) highlight that during flood periods in Bangladesh, average cloud cover reached 80%, making optical imagery unusable for capturing post-storm flood extent. Despite these challenges, optical remote sensing could support the identification of permanent water bodies in the pre-storm image. While SAR remains essential for capturing post-event flooding, the inclusion of optical data in the pre-event stage could provide a more robust baseline for flood extent detection.

5.2.2. Change detection limitations

A limitation of the flood detection method used in this study lies in its reliance on backscatter change detection between pre- and post-storm images. While this is effective for identifying event-driven flooding, it assumes that a flood only occurs where a change in backscatter is detected. This introduces a problem in wetland environments, such as the case study area, where water levels can naturally be rather high. Areas that were already saturated prior to the storm may not exhibit sufficient backscatter change and therefore remain undetected as flooded, even if they experienced substantial storm-driven flooding. To account for this, it could be insightful to first inspect absolute backscatter values for both pre- and post-storm images independently and to evaluate what constitutes typical backscatter values for different land cover types. This step should precede the application of change detection thresholds, helping to improve flood classification in persistently wet landscapes.

5.2.3. Threshold sensitivity

In the remote sensing tool, a pixel is classified as flooded when the ratio of post- to pre-event backscatter exceeds a predefined threshold value, which was set to 1.35 in the case study. A sensitivity analysis revealed that the detected flood extent is highly sensitive to the chosen threshold. Adjusting the thresh-

old from 1.35 to 1.25 resulted in a 41.3% increase in detected flooded area, while increasing it to 1.45 from 1.35 led to a 31.6% decrease in flood extent.

In the sensitivity analysis, lowering the threshold captures more flooded pixels, yet the additional area detected was found to be mostly spatially fragmented and affected by speckle noise. This also became evident in the dry tests where lower thresholds produced a substantial increase in false positives. For this reason, a more conservative threshold of 1.35 was deemed acceptable in this study to minimize the risk of misclassifying non-flooded pixels as flooded. Reflecting on the selected threshold, the qualitative comparison with the flood maps of Zhang et al. (2018) and NOAA (2017) suggests that the threshold value of 1.35 was indeed rather conservative. While the overall flood extent showed similar spatial patterns across the maps, the SAR-derived map produced in this study exhibited a smaller extent, meaning that the remote sensing tool has ignored actual flood extents that took place due to Hurricane Irma. However, the differences between the SAR flood map and the map of NOAA (2017) may also be attributed to variations in acquisition date, sensor type, and spatial resolution. While the choice for a stricter threshold may have led to an underestimation of the total flooded area, it did enhance confidence that the detected areas of the tool represent actual inundation, which was preferred for further interpretation of the flood extent.

To further address limitations associated with threshold-based flood mapping, advanced classification methods such as machine learning or deep learning could be explored. As Ghosh et al. (2024) note, traditional SAR-based flood mapping approaches, often suffer from classification errors due to the complex interaction between radar backscatter and diverse land surface conditions. They propose a deep learning approach which has demonstrated better accuracy in distinguishing flooded from non-flooded areas. However, the adoption of such advanced techniques would come at the cost of increased complexity and reduced accessibility. Unlike the current approach, which is implemented entirely within Google Earth Engine using open-access data, deep learning-based methods may have different requirements that may limit their widespread use, particularly in data-scarce contexts.

5.2.4. Model choices

Several methodological choices in this study introduce uncertainties in the flood detection results. While dry tests were used to test the flood detection method under non-flood conditions for three different years, these should be further expanded by including more data points from several other years. This would enable better identification of systematic false positives and help differentiate between flood-driven inundation and regular seasonal or rain-induced water accumulation. Furthermore, in the current case study, only ascending-orbit images were analyzed; incorporating both ascending and descending acquisitions in dry tests could improve insights in flood patterns. The inclusion of additional pre-storm imagery, spanning multiple years, could improve the quality of the baseline backscatter, potentially resulting in better change detection.

It is important to note that the parameter choices made, such as the change detection threshold, smoothing radius, and pixel connectivity criteria, are inherently dependent on the study's spatial scale. In this case, the Everglades mangrove region was analyzed over a broad area, with flooding assessed at a large scale. Accordingly, relatively coarse settings were applied: a smoothing radius of 200 meters and a connectivity threshold of 50 pixels. These choices were intended to reduce noise, prioritizing clarity of broader flood patterns over highly localized detection.

5.2.5. Validation

A key limitation of the current remote sensing-based flood mapping tool is that it lacks quantitative validation, due to the scope of this study. While an initial validation was performed qualitatively using two flood maps from literature (NOAA, 2017; Zhang et al., 2018), a further quantitative validation is essential to adjust the model where needed and to strengthen the reliability of the results and to allow the SAR-derived flood map to serve as credible input for numerical models. Specific recommendations on how this quantitative validation could be performed is provided in chapter 7.

5.3. Conceptual guideline

The conceptual guideline serves to structure the range of variables that influence whether mangroves are likely to reduce flood extent along a given coastline. While substantial research exists on the

topic, much of the knowledge remains fragmented. The guideline addresses this by organizing the relevant information into a structured framework, enabling users to form an initial assessment of the flood attenuation potential of mangroves at a specific site, offering a useful starting point. Yet, the guideline contains several simplifications regarding physical processes and therefore presents a more generalized representation of the following elements:

5.3.1. Long-term impact of mangroves on flood extent

This study focuses on the short-term effects of mangroves on flood extent. However, mangroves also exert major long-term influences on coastal flood reduction. Mangroves reduce bed shear stress and stabilize sediments through their root systems, thereby promoting sediment deposition and reducing erosion (Gijón Mancheño, 2022; Temmerman et al., 2022). These processes result in vertical surface elevation gain, which in turn lowers water depth, which then improves the capacity of mangroves to attenuate incoming surge and short waves (Gijón Mancheño, 2022). Additionally, mangroves prevent lateral erosion and therefore retreat of the coastline, impacting the coastline geometry (Pennings et al., 2021; Temmerman et al., 2022). Lastly, they also interact with the location and depth of channels (McIvor et al., 2012b). Together, these long-term processes shape the coastal landscape in ways that affect the degree to which mangrove coasts to reduce surge and short wave energy in the short term. The exclusion of these longer-term dynamics from the current guideline represents a limitation and may lead to an underestimation of the true flood protection potential of mangrove ecosystems.

5.3.2. Wave set-up

The elevated water level at a coast due to a tropical storm is often a combination of surge and set-up, yet the conceptual guideline does not cover this distinction (McIvor et al., 2012b). Determining the relative contribution of wave set-up versus storm surge to the total elevated water level is challenging. According to the numerical modeling study by Dean and Bender (2006), wave set-up can account for 30–60% of the peak water level during 100-year return period storms (McIvor et al., 2012b). In the case study of Hurricane Irma, the elevated water levels were attributed to storm surge. However, it is equally plausible that a substantial portion resulted from wave set-up, generated by wave breaking offshore of the mangroves. This ambiguity complicates the clear separation of flood drivers within the conceptual guideline, which is why set-up is currently not explicitly addressed. This limitation should be acknowledged when interpreting the guideline and evaluating the protective function of mangroves. Studies such as Van Rooijen et al. (2016), which explore the interaction between vegetation and wave set-up, provide valuable insights that should be more fully integrated into future iterations of the guideline.

5.3.3. Water storage function

While the conceptual guideline accounts for surge and short-wave attenuation, a notable limitation is the absence of the third mechanism by which mangroves influence flood extent: their water storage capacity (Temmerman et al., 2022). This refers to the ability of mangroves to temporarily retain water, thereby reducing water exchange and limiting inland flooding (Montgomery et al., 2019)

Through water retention in channels within mangrove forests, and via infiltration into the soil, water remains in the forest system rather than propagating further inland (Smolders et al., 2015). Leaving out this element from the conceptual guideline may lead to an underestimation of the flood extent reduction capacity provided by mangrove forests. As Montgomery et al. (2019) emphasize, the water storage function of mangrove forests may be as relevant in lowering peak water levels as the frictional resistance offered at the seaward edge of the forest. Future developments of the guideline should therefore seek to incorporate methods for quantifying this water storage mechanism (beyond forest width), to better reflect the contribution of mangrove forests' water storage function.

5.3.4. Flood depth vs. flood extent

It is essential to distinguish between flood depth and flood extent. This study focuses on flood extent, defined as the spatial area inundated due to a flood event, derived from satellite imagery using backscatter change metrics. In contrast, many of the variables included in the conceptual guideline are discussed primarily in terms of reductions in flood depth, expressed as an attenuation rate, which is the decrease in water level per distance through the forest. It is important to note that a reduction in flood depth does not directly imply a reduction in flood extent. The flood map generated by the re-

remote sensing tool, visualizes flood extent but provides no further information about the underlying flood depth. For example, when mangroves attenuate storm surge, they reduce the peak water level; however, this attenuation may not immediately manifest as a reduced flood extent. Instead, the first effect is a reduction in flood depth. This distinction is important when interpreting the conceptual guideline. Incorporating water level changes into the remote sensing tool could provide further opportunities, as recommended in more detail in chapter 7.

5.3.5. Interdependency between variables

A last limitation of the conceptual guideline is its omission of the interdependencies among hydrodynamic, geomorphological, and ecological variables. Some examples of such interdependencies among variables included in the guideline are outlined below, highlighting the intricate network of factors at play:

- **Geomorphological and hydrodynamic variables:** Tidal flats located in front of mangroves contribute to wave height reduction of up to 70% of the total reduction (Van Wesenbeeck et al., 2025). The coastal slope influences how waves shoal and break, impacting the short wave height approaching the mangrove forest.
- **Ecological and geomorphological variables:** Mangroves influence the vertical elevation (reducing water depth), slope, and presence of channels of the coastline (Gijón Mancheño, 2022). Lower water depth increases the relative contribution of root structures to the attenuation, which is favourable for the attenuation of short waves and surge. The presence of tidal channels can sustain elevated surge levels further inland. Mangroves, by maintaining these channels, may indirectly reduce their own capacity to attenuate storm surge (McIvor et al., 2012b).
- **Interdependent hydrodynamic variables:** The degree to which incoming short waves are attenuated is influenced by the underlying surge height and general water depth (McIvor et al., 2012b). Higher surge levels elevate the short waves, leading to increased interaction between short waves and the upper parts of mangrove vegetation (e.g., branches and leaves rather than roots), which in turn reduces short wave energy attenuation.

In addition to these interdependencies, the representation of flood drivers in the guideline as strictly binary—either surge or short waves—is another notable limitation. In reality, storm-induced flooding is typically driven by a combination of multiple hydrodynamic components. While the guideline separates these drivers to facilitate variable-specific analysis, it should be noted that actual flood dynamics result from the superposition and interaction of both surge and wave processes. While acknowledging the limitations of the guideline, it remains usable for gaining an initial understanding of the system before engaging in complex modelling or fieldwork.

5.4. Wider contribution

Zooming out, this thesis contributes to the broader field of the research on mangrove-induced flood attenuation under tropical storm conditions by taking first steps in applying remote sensing to detect flood extent within mangrove areas. This offers three key benefits.

First, it constructs a more complete picture of the elements influencing flood extent and mangrove interaction, something not currently achievable with hydrodynamic models or field-based observations alone. The conceptual guideline developed in this study, when informed with remote sensing outputs, provides an accessible way to consider variables that affect whether mangroves are likely to reduce flooding. It offers a practical entry point to preliminarily assess the potential role of mangroves in coastal protection, as was demonstrated in the application of the conceptual guideline to the case study. Moreover, the approach helps identify areas with high potential impact of mangroves on flood extent, thereby guiding where to focus more resource-intensive studies.

Second, the developed remote sensing tool can be used to validate numerical models in the appointed high potential areas. Unlike traditional field validation methods, which rely on sparse point-based data such as tide gauges, the remote sensing tool provide full spatial coverage flood maps. These can serve as valuable comparisons for numerical model outputs. While the presented remote sensing approach remains at an early, exploratory stage, it lays out a first pipeline for remote sensing to be integrated into further flood assessments in mangrove areas, as it was shown successful at detecting flood extent in the Everglades mangrove area following Hurricane Irma. A key strength of the remote sensing tool

is its reliance on open-access, globally available datasets and freely accessible processing platform. This ensures that the method can be replicated and applied in low-resource areas.

Finally, both the remote sensing tool and the conceptual guideline are globally applicable whilst promoting a site-specific approach. The guideline is intentionally constructed to branch into different coastal typologies, mangrove structures, and hydrodynamic conditions, which can be assessed at different locations using the remote sensing tool. This prevents the tendency to treat mangroves as one-size-fits-all flood protection strategies. Doing so overlooks the context-dependent nature of these ecosystems. On the contrary, to successfully integrate mangroves in coastal protection, a tailored application and site-specific understanding is required, an objective to which both the conceptual guideline and the remote sensing tool contribute.

Conclusion

Conclusion overview

What can remote sensing contribute to the assessment of flood extent and the potential flood-reducing role of mangroves during tropical storms?

Which geomorphological, ecological, and hydrodynamic variables impact the potential of mangroves to reduce flood extent following tropical storms



The following aspects influence mangrove impact on flood extent:

- Coastal type (open coast, lagoonal, estuarine, deltaic)
- Dominant hydrodynamic forcing (surge, short waves, precipitation)
- Hydrodynamic variables: surge height, forward storm speed, short wave height & period, water level
- Ecological variables: forest width, above-ground biomass, zonation
- Geomorphological variables: coastal slope, presence of channels

How can remote sensing be used to detect flood extent in mangrove areas following tropical storms?



The remote sensing tool for mapping flood extent in mangrove areas includes the following elements:

- Radar remote sensing: SAR C-band Sentinel-1 imagery, output resolution of 10m
- Backscatter change detection method for flood mapping
- Processing in Google Earth Engine
- Integration of EO datasets: Mangrove extent, biomass, storm track, channel presence, precipitation, elevation

How can the approach, applied to the Everglades during Hurricane Irma, inform hydrodynamic models of flood extent and relevant variables under tropical storm conditions?



- The remote sensing tool successfully mapped a flood extent of 168,811 ha & visualized relevant variables
- Area 1 is identified as high potential area for mangrove impact on flood extent, based on comparison SAR- and bathtub model flood extent
- The detected flood extent and identified high potential area can inform hydrodynamic models in this area by providing full coverage flood validation data, as alternative to limited point-based ground validation

This thesis explored the contribution of earth observations to assess flood extent and relevant variables affecting attenuation in mangrove area following tropical storms. Regarding the first subquestion, it is concluded that hydrodynamic, ecological, and geomorphological variables impact flood extent reduction by mangroves during tropical storms. A conceptual guideline was developed to structure these variables and to assess the potential impact that mangroves can have on flood extent at a specific coast following a tropical storm. The conceptual guideline firstly highlights the importance of accounting for coastal typology and the dominant hydrodynamic forcing of the flood. Regarding hydrodynamic variables, surge height, the forward storm speed, short wave height and period, and water level were found of impact on mangroves' ability to reduce flood extent. For the ecological variables, the forest width, above-ground mangrove biomass and species zonation were identified as influential parameters for flood attenuation by mangroves. Lastly, geomorphological variables, including the coastal slope and the presence of channels and ponds, were considered crucial to account for when assessing mangrove impact on flood extent.

Addressing the second subquestion, it was concluded that a backscatter change detection approach using Sentinel-1 C-band Synthetic Aperture Radar (SAR) data, processed in Google Earth Engine, can be used to detect flood extent in mangrove areas following tropical storms. This approach is integrated in a remote sensing tool that maps flood extent and incorporates open-access earth observation

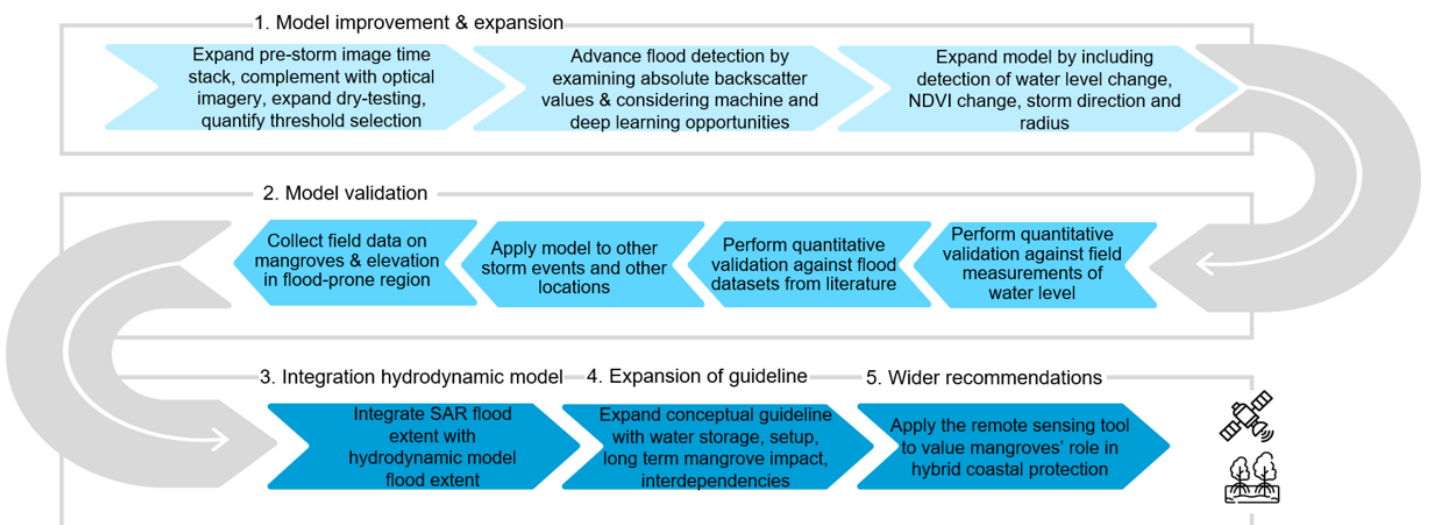
datasets on mangrove extent, mangrove above-ground biomass, storm track, and channel presence. Furthermore, a bathtub inundation model and precipitation data is integrated in the remote sensing tool for further contextualization of flood extent.

Concerning the third subquestion, applied on the case study of Hurricane Irma in the Everglades National Park, the remote sensing tool mapped flood extent and informed the conceptual guideline on relevant variables. The remote sensing tool estimated a flood extent of 168,811 hectares within the defined area of interest which showed spatial resemblance with flood maps in literature to a large extent. Several model parameters were tested and refined, resulting in a final change detection threshold value of 1.35 for flood detection, which is on the conservative side, and likely the one of the causes for discrepancies between the derived flood map and flood maps from literature. Dry tests in non-flooded periods showed an average of only 2% of the flood extent detected during hurricane Irma. Applying the conceptual guideline on the case study highlighted the lagoonal coastal type and considered precipitation and surge as the dominant hydrodynamic forcings leading to the flood. Comparison of the SAR-derived flood map with precipitation data and the bathtub model flood extent enabled differentiation between rainfall-driven and coastal flooding. It also identified a high-potential area for mangrove impact, where the two flood extents diverged. In this area, high seaward-edge mangrove biomass, sufficient forest width, and a gentle coastal slope favour surge attenuation. However, factors such as the presence of channels, low storm forward speed, and high surge levels may have reduced the impact of mangroves on flood extent. The remote sensing tool, through its effective detection of flood extent and visualization of key variables, can complement hydrodynamic models by identifying high-potential areas and providing full-coverage validation data. Hydrodynamic models are capable of isolating the impact of mangroves on flood extent, and the remote sensing tool strengthens these models by supplying observational, globally available data, enhancing their typically limited ground-based validation efforts.

Ultimately, addressing the main research question, the combination of the conceptual guideline, the remote sensing tool, and case study application illustrates how remote sensing can effectively detect flood extent in mangrove area following tropical storms, while pointing out high potential areas and visualizing important variables for attenuation by mangroves. This approach not only enhances the contextual understanding of variables influencing attenuation by offering a more comprehensive view of the factors involved, but more importantly, it establishes a first exploration toward leveraging remote sensing for the critically needed validation of flood extent maps generated by numerical models. By making use of free and globally available datasets, remote sensing is accessible to data-scarce tropical regions where mangroves are located and could offer invaluable flood-reducing benefits.

Recommendations

Recommendations roadmap



Based on the limitations identified in the discussion, recommendations for future research are proposed. These recommendations are outlined in a roadmap consisting of five steps. The first step involves further improvement and expansion of the remote sensing tool. The second step is to carry out additional validation. Once the tool has been thoroughly verified and validated, the third step is to integrate it with a numerical model. The fourth step focuses on improving the conceptual guideline for creating a more complete understanding of the system. Finally, the fifth step involves formulating broader recommendations to explore the long-term applicability of the developed conceptual guideline and remote sensing tool.

1. Model improvement and expansion

In response to the limitations identified in the flood detection method, several recommendations are proposed to improve and expand the flood mapping tool.

- **Enhancement of the pre-storm image timestack:** The pre-storm image timestack should be expanded to include a greater number of SAR images, coming from multiple years and dates, while remaining within the same season (dry or rainy). This expanded timestack will reduce the influence of random noise by averaging across a broader dataset, thereby producing a more stable baseline scenario for non-flooded conditions. The pre-storm image timestack can be further improved by incorporating optical satellite imagery. Although post-storm optical imagery is comprised by cloud cover, pre-storm optical data can come in useful for characterizing permanent water bodies in the non-flooded baseline scenario. As Psomiadis et al. (2020) demonstrated, the SAR-based pre-storm image can be complemented and compared with an optical pre-storm composite, using indices such as the MNDWI.

- **Expansion of dry testing:** To further assess the reliability of the flood mapping tool, the dry testing phase should be expanded by incorporating additional years into the test. For dry tests conducted during the dry season, increasing the number of data points in the test can help to identify specific locations or land cover types that are more prone to false positives. Applying statistical analysis to these results could enable the estimation of the probability of false positives. Pixels that consistently appear as flooded during dry-season testing, despite the absence of flood events, can then be flagged and removed from future analyses. For dry tests conducted during the rainy season, also over multiple years and dates, it might become possible to identify areas that are regularly affected by rainfall-induced flooding. Recognizing these patterns is valuable for interpreting flood extent imagery from storm events, as it can help differentiate between the dominant hydrodynamic drivers, rainfall versus storm surge, behind the observed flooding. Importantly, both dry-season and rainy-season dry tests should be complemented with imagery from the descending satellite pass, as the current analysis relies solely on ascending pass imagery. This may reveal other patterns of false positives that are not present in the ascending data.
- **Quantitative threshold sensitivity analysis and selection:** A quantitative threshold sensitivity analysis should be conducted to enhance the threshold selection. This can be achieved by applying a confusion matrix, which evaluates the model's performance in terms of false positives, false negatives, true positives, and true negatives. By quantifying these metrics, the threshold selection process can be made more data-driven, rather than the qualitative threshold selection performed in this study.
- **Advancing flood detection techniques:** The flood detection itself can be reconsidered as the current change detection approach has certain limitations, particularly in areas that are persistently moist, such as wetlands. To address this, it is recommended to first examine the absolute radar signal values before applying the change detection ratio. In addition, the potential benefits of machine learning approaches should be explored for flood detection from remote sensing imagery (J. Li et al., 2022a). Studies have demonstrated the effectiveness of methods such as Support Vector Machine, decision trees, and object-oriented classification in flood detection from satellite data (Liu et al., 2020; Tang et al., 2018). Moreover, the integration of deep learning techniques, particularly convolutional neural networks, could offer further advancements (J. Li et al., 2022a; Y. Li et al., 2018).
- **Integration of water level change, NDVI change, storm radius:**
 - In addition to mapping flood extent, it would be beneficial to include water level change in the remote sensing tool. This can be achieved using InSAR (Interferometric Synthetic Aperture Radar) observations, which detect changes in the surface based on phase differences of the radar signals. Such methods allow for the estimation of water level changes and have been applied in previous studies (Oliver-Cabrera & Wdowinski, 2016; Zhang et al., 2018)
 - Incorporating NDVI (Normalized Difference Vegetation Index) change, before and after a storm event, could provide insight into the impact of a tropical storm on mangrove forest health. NDVI is a spectral index, retrieved from optical satellite imagery and is an indicator of vegetation health, it makes use of the near-infrared and the red band of the electromagnetic spectrum (Singh & Schoenmakers, 2023). Including NDVI change in the flood mapping tool can help assess storm-induced mangrove damage and highlight areas of strong storm interaction with mangrove zones. Prior research has explored this approach, including studies of NDVI change of mangroves after tropical storms in Mozambique (Singh & Schoenmakers, 2023) and Hurricane Irma in the Everglades (Lagomasino et al., 2021).
 - The storm track itself is already included in the model but incorporating the radius of storm impact along its track into the tool could provide additional value. Visualizing the storm's trajectory and spatial reach may support a clearer distinction between coastal flooding and flooding driven by rainfall.

2. Model validation

The following steps are suggested for the further validation of the remote sensing tool:

- **Quantitative validation against flood datasets:** Currently, the flood extent generated by the

model is compared qualitatively to flood maps from Zhang et al. (2018) and NOAA (2017). To strengthen this validation, it is recommended to obtain the original datasets used in these studies and conduct a quantitative evaluation, allowing for a better understanding of where the model performs well and where adjustments are necessary in the model settings.

- **Quantitative validation against field measurements:** In the Everglades, a network of water level gauges is present (USGS, 2025). This provides a valuable opportunity for quantitative validation of the SAR-derived flood extent maps using field-based measurements. A representative sample of points should be selected—for example, ten points within the detected flooded area and ten outside of it. For each of these points, water level data should be examined over a period surrounding the storm event. A statistical analysis should be conducted to determine whether the recorded water levels at those points were significantly high, allowing for an assessment of whether those areas were indeed flooded. Such an approach builds on the validation methodology of Zhang et al. (2018). However, rather than simply noting that water levels were elevated during the storm event, this validation should be expanded through formal statistical evaluation.
- **Application of the model to other storm events:** Firstly, the model should be applied to additional tropical storm events within the Everglades region. For instance, Hurricane Ian, a Category 4 storm that made landfall in the case study area in 2022, caused flooding and would be an appropriate case for further testing (Gahtan et al., 2024). Beyond the Everglades, the model should also be applied to other regions affected by tropical storms to test its transferability. By applying the model to varied events and locations, it should be assessed whether model parameters need adjustment for different environments.

Several criteria must be met when selecting new locations and events:

- Presence of a mangrove forest
- Occurrence of a tropical storm with documented flooding due to the event
- Availability of Sentinel-1 imagery shortly after the event

Potential test cases include:

- Hurricanes Maria (2017) and Fiona (2022) in Puerto Rico (Yu & Gao, 2024)
 - Hurricane Dorian (2019) in the Bahamas (Cerrai et al., 2020)
 - Hurricane Amphan (2020) in the Sundarbans region of Bangladesh (Halder & Bandyopadhyay, 2022)
 - Multiple events in the Philippines, a region including extensive mangrove cover and high tropical storm frequency (Menéndez et al., 2018)
- **Field data collection:** In the Everglades, as well as in other regions where the model may be applied, field data collection is helpful to provide contextual insight on the geomorphological, hydrodynamic, and ecological conditions of the site for the outputs of the remote sensing tool and conceptual guideline. As demonstrated by Horstman et al. (2014), various types of field observations are valuable regarding wave attenuation by mangroves:
 - Geomorphological data collection: To ground-truth the elevation retrieved from the satellite data, an elevation survey should be performed. This can provide information on the coastal slope and serve as a reference point to which both water level and canopy height can be referenced. To assess the long-term impact of mangroves on coastal protection, sediment data should also be collected; sediment traps can be installed to measure sedimentation rates (Horstman et al., 2014).
 - Ecological data collection: Various characteristics of the mangrove forest can be derived by classifying species, measuring canopy height and stem diameter, as outlined by Horstman et al. (2014). These parameters provide insight into forest width, zonation, and above-ground biomass.
 - Hydrodynamic data collection: Pressure sensors can be installed along a transect through the mangrove forest. From the resulting data, a wave energy density spectrum can be

generated, allowing the retrieval of variables such as significant wave height and wave period (Horstman et al., 2014).

3. Integration with hydrodynamic model

To address the limitation of establishing causal relationships between mangrove presence and flood extent, the remote sensing tool—once properly tested, verified, and validated as outlined above—should be used to validate numerical flood models.

- **Comparison of flood extents:** Narayan et al. (2019) developed a numerical model of Hurricane Irma in the Everglades. These modelled flood extents should be compared with those produced by the remote sensing tool as means of validation of the numerically modelled flood extent. Specifically, the scenarios with and without mangrove coverage should be overlaid with the SAR flood map to assess where the numerical model may overestimate or underestimate the coastal protection value of mangroves. In addition to comparing flood extents, it can be valuable to explore how the ecological variables integrated into the remote sensing tool can improve the representation of mangroves in the numerical model. Currently, models often apply a uniform roughness value across the entire mangrove forest area, ignoring variations in zonation or biomass (McIvor et al., 2012b; Narayan et al., 2019). The ecological spatial variability provided by the remote sensing tool may help refine these inputs.

4. Expansion of the conceptual guideline

As noted in the discussion, certain concepts were excluded from the current conceptual guideline to maintain its accessibility for a broad range of end users and to serve as an initial tool for gaining insight. However, for more advanced applications, the guideline should be expanded to include the following additional components:

- **The interdependencies** between the variables in the guideline should be made explicit.
- **The water storage capacity** of mangroves should be incorporated to avoid underestimating its role in reducing flood extent (Montgomery et al., 2019).
- **The interaction between wave set-up and mangroves** should be clearly addressed (Van Rooijen et al., 2016).
- **The long-term contribution** of mangroves to coastal protection should be included (McIvor et al., 2013).

5. Wider recommendations

In addition to the specific recommendations that follow directly from the limitations of the current model, broader recommendations are proposed to guide future research and application.

An important direction for further exploration is the potential role of the remote sensing flood mapping tool and the conceptual guideline in the design of hybrid coastal protection strategies. Hybrid coastal protection refers to the combination of natural elements, such as mangroves, with engineered structures, such as levees (van Zelst et al., 2021). Because effective surge attenuation by mangroves requires wide forest belts, and such space is increasingly limited due to deforestation, aquaculture, and urbanization, combining mangroves with coastal protection structures (e.g. with mangroves on the foreshore of levees), may offer a more feasible solution in many locations (Van Wesenbeeck et al., 2025).

As mangroves can attenuate storm surge and short waves, the required levee height can be reduced, which in turn leads to cost savings in coastal defence projects (van Zelst et al., 2021). Since the remote sensing tool can help validate numerical models and provide a more complete picture of the variables involved, the developed tool and guideline, once further advanced, can support estimations of the flood depth reduction provided by mangroves. This would enable decision-makers and designers, particularly in data-scarce regions, to better understand how much levee height, and therefore cost, can be saved, before having to commit to resource-heavy field observations. Such insights can help stimulate the restoration and maintenance of mangroves, ensuring their continued valuable contribution to coastal protection and the many ecosystem services they provide for people and nature.

References

- Amani, M., Moghimi, A., Mirmazloumi, S. M., Ranjgar, B., Ghorbanian, A., Ojaghi, S., Ebrahimi, H., Naboureh, A., Nazari, M. E., Mahdavi, S., Moghaddam, S. H. A., Asiyabi, R. M., Ahmadi, S. A., Mehravar, S., Mohseni, F., & Jin, S. (2022). Ocean Remote Sensing Techniques and Applications: A Review (Part I). *Water*, *14*(21), 3400. <https://doi.org/10.3390/w14213400>
- Bates, P. D., Quinn, N., Sampson, C., Smith, A., Wing, O., Sosa, J., Savage, J., Olcese, G., Neal, J., Schumann, G., Giustarini, L., Coxon, G., Porter, J. R., Amodeo, M. F., Chu, Z., Lewis Gruss, S., Freeman, N. B., Houser, T., Delgado, M., ... Krajewski, W. F. (2021). Combined Modeling of US Fluvial, Pluvial, and Coastal Flood Hazard Under Current and Future Climates. *Water Resources Research*, *57*(2). <https://doi.org/10.1029/2020WR028673>
- Bosboom, J., & Stive, M. (2023). *Coastal dynamics*. (Vol. 68). TUDelftOpen. <https://doi.org/DOI10.5074/T.2021.001>
- Bunting, P., Rosenqvist, A., Hilarides, L., Lucas, R. M., Thomas, N., Tadono, T., Worthington, T. A., Spalding, M., Murray, N. J., & Rebelo, L.-M. (2022). Global Mangrove Extent Change 1996–2020: Global Mangrove Watch Version 3.0. *Remote Sensing*, *14*(15), 3657. <https://doi.org/10.3390/rs14153657>
- Cangialosi, J., Latto, A., & Berg, R. (2021, September). *Tropical Cyclone Report: Hurricane Irma* (tech. rep.). National Hurricane Center. https://www.nhc.noaa.gov/data/tcr/AL112017_Irma.pdf
- Cascadia CoPes Hub. (2024). Understanding Compound Flooding.
- Cerrai, D., Yang, Q., Shen, X., Koukoulas, M., & Anagnostou, E. N. (2020). Brief communication: Hurricane Dorian: automated near-real-time mapping of the “unprecedented” flooding in the Bahamas using synthetic aperture radar. *Natural Hazards and Earth System Sciences*, *20*(5), 1463–1468. <https://doi.org/10.5194/nhess-20-1463-2020>
- Choe, Y., & Schuett, M. A. (2020). Stakeholders’ perceptions of social and environmental changes affecting Everglades National Park in South Florida. *Environmental Development*, *35*, 100524. <https://doi.org/10.1016/j.envdev.2020.100524>
- Cracknell, A. (2007). *Introduction to Remote Sensing*.
- Dalrymple, R. A., Kirby, J. T., & Hwang, P. A. (1984). Wave Diffraction Due to Areas of Energy Dissipation. *Journal of Waterway, Port, Coastal, and Ocean Engineering*, *110*(1), 67–79. [https://doi.org/10.1061/\(ASCE\)0733-950X\(1984\)110:1\(67\)](https://doi.org/10.1061/(ASCE)0733-950X(1984)110:1(67))
- Das, S. C., Thammineni, P., & Ashton, E. C. (2022, January). *Mangroves: Biodiversity, Livelihoods and Conservation*. Springer Nature. <https://doi.org/10.1007/978-981-19-0519-3>
- Dean, R. G., & Bender, C. J. (2006). Static wave setup with emphasis on damping effects by vegetation and bottom friction. *Coastal Engineering*, *53*(2-3), 149–156. <https://doi.org/10.1016/J.COASTALENG.2005.10.005>
- Duke, N. C., Lo, E., & Sun, M. (2002). Global distribution and genetic discontinuities of mangroves - Emerging patterns in the evolution of *Rhizophora*. *Trees - Structure and Function*, *16*(2-3), 65–79. <https://doi.org/10.1007/s00468-001-0141-7>
- Eilander, D., Couasnon, A., Leijnse, T., Ikeuchi, H., Yamazaki, D., Muis, S., Dullaart, J., Haag, A., Winsemius, H. C., & Ward, P. J. (2023). A globally applicable framework for compound flood hazard modeling. *Natural Hazards and Earth System Sciences*, *23*(2), 823–846. <https://doi.org/10.5194/nhess-23-823-2023>
- EOS Data Analytics. (2023, July). Normalized Difference Water Index (NDWI).
- ESA. (2017, October). Wave height during Hurricane Irma. https://www.esa.int/Applications/Observing_the_Earth/Copernicus/Sentinel-1/Sentinel-1_sees_through_hurricanes
- Febrianto, S., Rahman, A., Jati, O. E., Wirasatriya, A., Muskananfolo, M. R., & Latifah, N. (2025). Machine learning for mangrove species distribution using Sentinel 2 satellite image in Segara Anakan, Cilacap Region, Indonesia. *Regional Studies in Marine Science*, *81*, 103984. <https://doi.org/10.1016/j.rsma.2024.103984>

- Feller & Sitnik. (1996). *Mangrove Ecology: A Manual for a Field course* (tech. rep.). Smithsonian Institution.
- Fitzpatrick, P. (1999). *Natural disasters: Hurricanes: A reference handbook*. Bloomsbury Publishing USA.
- Flather, R. (2001). Storm Surges. In *Encyclopedia of ocean sciences* (pp. 2882–2892). Elsevier. <https://doi.org/10.1006/rwos.2001.0124>
- Florida Museum. (2022, April). Everglades Restoration. <https://www.floridamuseum.ufl.edu/earth-systems/blog/tell-me-about-everglades-restoration/>
- Friebel, H. C. (2016). Storm Surges. In *Encyclopedia of estuaries. encyclopedia of earth sciences series*. (pp. 622–623). Springer, Dordrecht. https://doi.org/10.1007/978-94-017-8801-4_{ }67
- Friess, D. A., Rogers, K., Lovelock, C. E., Krauss, K. W., Hamilton, S. E., Lee, S. Y., Lucas, R., Primavera, J., Rajkaran, A., & Shi, S. (2019). The State of the World's Mangrove Forests: Past, Present, and Future. *Annual Review of Environment and Resources*, 44(1), 89–115. <https://doi.org/10.1146/annurev-environ-101718-033302>
- Fritz, H. M., & Blount, C. (2007). *CHAPTER 2 PROTECTION FROM CYCLONES Thematic paper: Role of forests and trees in protecting coastal areas against cyclones* (tech. rep.).
- Gahtan, J., Knapp, K., Schreck, C., Diamond, H., Kossin, J., & Kruk, M. (2024). *International Best Track Archive for Climate Stewardship (IBTrACS) Project, Version 4.01* (tech. rep.). OAA National Centers for Environmental Information.
- Ghosh, B., Garg, S., Motagh, M., & Martinis, S. (2024). Automatic Flood Detection from Sentinel-1 Data Using a Nested UNet Model and a NASA Benchmark Dataset. *PFG – Journal of Photogrammetry, Remote Sensing and Geoinformation Science*, 92(1), 1–18. <https://doi.org/10.1007/s41064-024-00275-1>
- Gijón Mancheño, A. (2022). *Restoring mangroves with structures Improving the mangrove habitat using local materials* [Doctoral dissertation, TUDelft]. <https://doi.org/10.4233/uuid:ed292367-ed2b-4bd3-a236-9f10d9c01da8>
- Gijón Mancheño, A., Herman, P. M., Jonkman, S. N., Kazi, S., Urrutia, I., & van Ledden, M. (2021). Mapping mangrove opportunities with open access data: A case study for Bangladesh. *Sustainability (Switzerland)*, 13(15). <https://doi.org/10.3390/su13158212>
- Gijón Mancheño, A., Vuik, V., Van Wesenbeeck, B., Jonkman, S. N., Moll, R., Kazi, S., Urrutia, I., & van Ledden, M. (2022, October). *Wave Reduction by Mangroves during Cyclones in Bangladesh: Implementing Nature-Based Solutions for Coastal Resilience*. <https://doi.org/10.1596/1813-9450-10240>
- Gijsman, R., Horstman, E. M., van der Wal, D., Friess, D. A., Swales, A., & Wijnberg, K. M. (2021, July). Nature-Based Engineering: A Review on Reducing Coastal Flood Risk With Mangroves. <https://doi.org/10.3389/fmars.2021.702412>
- Giri, C., Ochieng, E., Tieszen, L. L., Zhu, Z., Singh, A., Loveland, T., Masek, J., & Duke, N. (2011). Status and distribution of mangrove forests of the world using earth observation satellite data. *Global Ecology and Biogeography*, 20(1), 154–159. <https://doi.org/10.1111/j.1466-8238.2010.00584.x>
- Giri, C. (2021, February). Recent advancement in mangrove forests mapping and monitoring of the world using earth observation satellite data. <https://doi.org/10.3390/rs13040563>
- Google Earth Engine. (2025). Sentinel-1 Algorithms. <https://developers.google.com/earth-engine/guides/sentinel1>
- Gorelick, N., Hancher, M., Dixon, M., Ilyushchenko, S., Thau, D., & Moore, R. (2017). Google Earth Engine: Planetary-scale geospatial analysis for everyone. *Remote Sensing of Environment*, 202, 18–27. <https://doi.org/10.1016/j.rse.2017.06.031>
- Granek, E. F., & Ruttenberg, B. I. (2007). Protective capacity of mangroves during tropical storms: a case study from 'Wilma' and 'Gamma' in Belize. *Marine Ecology Progress Series*, 343, 101–105. <https://doi.org/10.3354/MEPS07141>
- Grimley, L. E., Sebastian, A., Leijnse, T., Eilander, D., Ratcliff, J., & Luettich, R. (2025). Determining the Relative Contributions of Runoff, Coastal, and Compound Processes to Flood Exposure Across the Carolinas During Hurricane Florence. *Water Resources Research*, 61(3). <https://doi.org/10.1029/2023WR036727>
- Gunderson, L., & Light, S. S. (2007). Adaptive management and adaptive governance in the everglades ecosystem. *Policy Sciences*, 39(4), 323–334. <https://doi.org/10.1007/s11077-006-9027-2>

- Halder, B., & Bandyopadhyay, J. (2022). Monitoring the tropical cyclone 'Yass' and 'Amphan' affected flood inundation using Sentinel-1/2 data and Google Earth Engine. *Modeling Earth Systems and Environment*, 8(3), 4317–4332. <https://doi.org/10.1007/s40808-022-01359-w>
- Hamidi, E., Peter, B. G., Munoz, D. F., Moftakhari, H., & Moradkhani, H. (2023). Fast Flood Extent Monitoring With SAR Change Detection Using Google Earth Engine. *IEEE Transactions on Geoscience and Remote Sensing*, 61, 1–19. <https://doi.org/10.1109/TGRS.2023.3240097>
- Hamilton, S. (2020). *Mangroves and Aquaculture: A Five Decade Remote Sensing Analysis of Ecuador's Estuarine Environments*. <http://www.springer.com/series/8795>
- Han, X., Feng, L., Hu, C., & Kramer, P. (2018). Hurricane-Induced Changes in the Everglades National Park Mangrove Forest: Landsat Observations Between 1985 and 2017. *Journal of Geophysical Research: Biogeosciences*, 123(11), 3470–3488. <https://doi.org/10.1029/2018JG004501>
- Harris, D. (1963). *Characteristics of the hurricane storm surge* (Vol. No. 48). Weather Bureau.
- Hawkins, S. J. (2020). *Oceanography and marine biology : an annual review. Volume 58*. CRC Press.
- Herrera-Silveira, J., Teutli-Hernandez, C., Secaira-Fajardo, F., Braun, R., Bowman, J., Geselbracht, L., Musgrove, M., Rogers, M., Schmidt, J., Robles-Toral, P. J., Canul-Cabrera, J., & Guerra-Cano, L. (2022). Hurricane Damages to Mangrove Forests and Post-Storm Restoration Techniques and Costs. *The Nature Conservancy, Arlington, VA*. <https://doi.org/10.13140/RG.2.2.15961.39525>
- Horstman, E., Dohmen-Janssen, C., Narra, P., van den Berg, N., Siemerink, M., & Hulscher, S. (2014). Wave attenuation in mangroves: A quantitative approach to field observations. *Coastal Engineering*, 94, 47–62. <https://doi.org/10.1016/j.coastaleng.2014.08.005>
- Ihinegbu, C., Mönnich, S., & Akukwe, T. (2023, April). Scientific Evidence for the Effectiveness of Mangrove Forests in Reducing Floods and Associated Hazards in Coastal Areas. <https://doi.org/10.3390/cli11040079>
- IPCC. (2021, July). Weather and Climate Extreme Events in a Changing Climate. In *Climate change 2021 – the physical science basis contribution of working group I to the sixth assessment report of the intergovernmental panel on climate change* (pp. 1513–1766). Cambridge University Press. <https://doi.org/10.1017/9781009157896.013>
- IPCC. (2023, July). Ocean, Cryosphere and Sea Level Change. In *Climate change 2021 – the physical science basis* (pp. 1211–1362). Cambridge University Press. <https://doi.org/10.1017/9781009157896.011>
- Ji, T., & Li, G. (2020). Contemporary monitoring of storm surge activity. *Progress in Physical Geography: Earth and Environment*, 44(3), 299–314. <https://doi.org/10.1177/0309133319879324>
- Kasmalkar, I., Wagenaar, D., Bill-Weilandt, A., Choong, J., Manimaran, S., Lim, T. N., Rabonza, M., & Lallemand, D. (2024). Flow-tub model: A modified bathtub flood model with hydraulic connectivity and path-based attenuation. *MethodsX*, 12, 102524. <https://doi.org/10.1016/j.mex.2023.102524>
- Krauss, K. W., Doyle, T. W., Doyle, T. J., Swarzenski, C. M., From, A. S., Day, R. H., & Conner, W. H. (2009). Water level observations in mangrove swamps during two hurricanes in Florida. *Wetlands*, 29(1), 142–149. <https://doi.org/10.1672/07-232.1>
- Krauss, K. W., & Osland, M. J. (2019). Tropical cyclones and the organization of mangrove forests: a review. *Annals of Botany*. <https://doi.org/10.1093/aob/mcz161>
- Kundu, S., Lakshmi, V., & Torres, R. (2022). Flood Depth Estimation during Hurricane Harvey Using Sentinel-1 and UAVSAR Data. *Remote Sensing*, 14(6), 1450. <https://doi.org/10.3390/rs14061450>
- Lagomasino, D., Fatoyinbo, T., Castañeda-Moya, E., Cook, B., Montesano, P., Neigh, C., Corp, L., Ott, L., Chavez, S., & Morton, D. (2021). Storm surge and ponding explain mangrove dieback in southwest Florida following Hurricane Irma. *Nature Communications*, 12(1), 4003. <https://doi.org/10.1038/s41467-021-24253-y>
- Lehner, B., Messenger, M. L., Korver, M. C., & Linke, S. (2022). Global hydro-environmental lake characteristics at high spatial resolution. *Scientific Data*, 9(1), 351. <https://doi.org/10.1038/s41597-022-01425-z>
- Li, J., Ma, R., Cao, Z., Xue, K., Xiong, J., Hu, M., & Feng, X. (2022a). Satellite Detection of Surface Water Extent: A Review of Methodology. *Water*, 14(7), 1148. <https://doi.org/10.3390/w14071148>
- Li, J., Ma, R., Cao, Z., Xue, K., Xiong, J., Hu, M., & Feng, X. (2022b). Satellite Detection of Surface Water Extent: A Review of Methodology. *Water*, 14(7), 1148. <https://doi.org/10.3390/w14071148>

- Li, X., Han, G., Yang, J., & Wang, C. (2023). Remote Sensing Analysis of Typhoon-Induced Storm Surges and Sea Surface Cooling in Chinese Coastal Waters. *Remote Sensing*, *15*(7), 1844. <https://doi.org/10.3390/rs15071844>
- Li, Y., Zhang, H., Xue, X., Jiang, Y., & Shen, Q. (2018). Deep learning for remote sensing image classification: A survey. *WIREs Data Mining and Knowledge Discovery*, *8*(6). <https://doi.org/10.1002/widm.1264>
- Linke, S., Lehner, B., Ouellet Dallaire, C., Ariwi, J., Grill, G., Anand, M., Beames, P., Burchard-Levine, V., Maxwell, S., Moidu, H., Tan, F., & Thieme, M. (2019). Global hydro-environmental sub-basin and river reach characteristics at high spatial resolution. *Scientific Data*, *6*(1), 283. <https://doi.org/10.1038/s41597-019-0300-6>
- Liu, Q., Huang, C., Shi, Z., & Zhang, S. (2020). Probabilistic River Water Mapping from Landsat-8 Using the Support Vector Machine Method. *Remote Sensing*, *12*(9), 1374. <https://doi.org/10.3390/rs12091374>
- Maurya, K., Mahajan, S., & Chaube, N. (2021, December). Remote sensing techniques: mapping and monitoring of mangrove ecosystem—a review. <https://doi.org/10.1007/s40747-021-00457-z>
- Maymandi, N., Hummel, M. A., & Zhang, Y. (2022). Compound Coastal, Fluvial, and Pluvial Flooding During Historical Hurricane Events in the Sabine–Neches Estuary, Texas. *Water Resources Research*, *58*(12). <https://doi.org/10.1029/2022WR033144>
- Mazda, Y., Magi, M., Ikeda, Y., Kurokawa, T., & Asano, T. (2006). Wave reduction in a mangrove forest dominated by *Sonneratia*. *Wetlands Ecology and Management*, *14*(4), 365–378.
- Mclvor, A., Spencer, T., Moller, I., & Spalding, M. (2013). *The response of mangrove soil surface elevation to sea level rise* (tech. rep.). Natural Coastal Protection Series: Report 3. <https://www.conservationgateway.org/ConservationPractices/Marine/crr/library/Documents/mangrove-surface-elevation-and-sea-level-rise.pdf>
- Mclvor, A., Spencer, T., Spalding, M., Lacambra, C., & Möller, I. (2015). Mangroves, Tropical Cyclones, and Coastal Hazard Risk Reduction. In *Coastal and marine hazards, risks, and disasters* (pp. 403–429). Elsevier Inc. <https://doi.org/10.1016/B978-0-12-396483-0.00014-5>
- Mclvor, A., Spencer, T., Möller, I., & Spalding, M. (2012a). Reduction of wind and swell waves by mangroves. *Natural Coastal Protection Series: Report 1*.
- Mclvor, A., Spencer, T., Möller, I., & Spalding, M. (2012b). Storm Surge Reduction by Mangroves. *Natural Coastal Protection Series: Report 2*.
- Meijer, J. R., Huijbregts, M. A. J., Schotten, K. C. G. J., & Schipper, A. M. (2018). Global patterns of current and future road infrastructure. *Environmental Research Letters*, *13*(6), 064006. <https://doi.org/10.1088/1748-9326/aabd42>
- Mendez, F. J., & Losada, I. J. (2004). An empirical model to estimate the propagation of random breaking and nonbreaking waves over vegetation fields. *Coastal Engineering*, *51*(2), 103–118. <https://doi.org/10.1016/j.coastaleng.2003.11.003>
- Menéndez, P., Losada, I. J., Beck, M. W., Torres-Ortega, S., Espejo, A., Narayan, S., Díaz-Simal, P., & Lange, G.-M. (2018). Valuing the protection services of mangroves at national scale: The Philippines. *Ecosystem Services*, *34*, 24–36. <https://doi.org/10.1016/j.ecoser.2018.09.005>
- Mersmann, K. (2017, September). Irma (Atlantic Ocean). https://www.nasa.gov/centers-and-facilities/goddard/irma-atlantic-ocean/?utm_source=chatgpt.com
- Mo, Y., Simard, M., & Hall, J. W. (2023). Tropical cyclone risk to global mangrove ecosystems: potential future regional shifts. *Frontiers in Ecology and the Environment*, *21*(6), 269–274. <https://doi.org/10.1002/fee.2650>
- Montgomery, J. M., Bryan, K. R., Mullarney, J. C., & Horstman, E. M. (2019). Attenuation of Storm Surges by Coastal Mangroves. *Geophysical Research Letters*, *46*(5), 2680–2689. <https://doi.org/10.1029/2018GL081636>
- Montgomery, J., Bryan, K., & Coco, G. (2022). The role of mangroves in coastal flood protection: The importance of channelization. *Continental Shelf Research*, *243*, 104762. <https://doi.org/10.1016/j.csr.2022.104762>
- Murakami, H., Levin, E., Delworth, T. L., Gudgel, R., & Hsu, P.-C. (2018). Dominant effect of relative tropical Atlantic warming on major hurricane occurrence. *Science*, *362*(6416), 794–799. <https://doi.org/10.1126/science.aat6711>
- Musinguzi, A., Reddy, L., & Akbar, M. K. (2022). Evaluation of Wave Contributions in Hurricane Irma Storm Surge Hindcast. *Atmosphere*, *13*(3), 404. <https://doi.org/10.3390/atmos13030404>

- Narayan, S., Thomas, C. J., & Shepard, C. C. (2019). *Valuing the Flood Risk Reduction Benefits of Florida's Mangroves* (tech. rep.). <https://www.researchgate.net/publication/336903145>
- Nasr, A. A., Wahl, T., Rashid, M. M., Camus, P., & Haigh, I. D. (2021). Assessing the dependence structure between oceanographic, fluvial, and pluvial flooding drivers along the United States coastline. *Hydrology and Earth System Sciences*, 25(12), 6203–6222. <https://doi.org/10.5194/hess-25-6203-2021>
- National Park Service. (2025a). Geology Everglades National Parc. <https://www.nps.gov/ever/learn/nature/evergeology.htm>
- National Park Service. (2025b, January). Restoring America's Everglades. <https://www.evergladesrestoration.gov/>
- National Weather Service. (2017). Hurricane Irma Local Report. <https://www.weather.gov/mfl/hurricaneirma>
- Needham, H., & Keim, B. (2011, September). Storm surge: Physical processes and an impact scale. In *Recent hurricane research—climate, dynamics, and societal impacts* (pp. 385–406). <https://doi.org/10.5772/15925>
- Nelson. (2014). *Tropical Cyclones* (tech. rep.). Tulane University. https://www2.tulane.edu/~sanelson/New_Orleans_and_Hurricanes/tropical_cyclones.htm
- Nelson, A., Reuter, H., & Gessler, P. (2009). Chapter 3 DEM Production Methods and Sources. [https://doi.org/10.1016/S0166-2481\(08\)00003-2](https://doi.org/10.1016/S0166-2481(08)00003-2)
- NOAA. (2017, September). NOAA Satellites and Aircraft Monitor Catastrophic Floods from Hurricanes Harvey & Irma. <https://www.nesdis.noaa.gov/news/noaa-satellites-and-aircraft-monitor-catastrophic-floods-hurricanes-harvey-irma#:~:text=NOAA%20GOES-16%20and%20Suomi%20NPP%20monitored%20the%20flooding,first%20responders%20determine%20where%20to%20focus%20their%20efforts.>
- NOAA. (2018, September). One Year After Hurricane Irma: How Data Helped Track the Storm. <https://www.nesdis.noaa.gov/news/one-year-after-hurricane-irma-how-data-helped-track-the-storm>
- NOAA. (2024, November). El Niño & La Niña (El Niño-Southern Oscillation).
- Oliver-Cabrera, T., & Wdowinski, S. (2016). InSAR-Based Mapping of Tidal Inundation Extent and Amplitude in Louisiana Coastal Wetlands. *Remote Sensing*, 8(5), 393. <https://doi.org/10.3390/rs8050393>
- Orem, W. H., Fitz, C., Krabbenhoft, D. P., Poulin, B. A., Varonka, M. S., & Aiken, G. R. (2020). Ecosystem-Scale Modeling and Field Observations of Sulfate and Methylmercury Distributions in the Florida Everglades: Responses to Reductions in Sulfate Loading. *Aquatic Geochemistry*, 26(3), 191–220. <https://doi.org/10.1007/s10498-020-09368-w>
- Ottinger, M., & Kuenzer, C. (2020). Spaceborne L-Band Synthetic Aperture Radar Data for Geoscientific Analyses in Coastal Land Applications: A Review. *Remote Sensing*, 12(14), 2228. <https://doi.org/10.3390/rs12142228>
- Parkinson, R. W., & Wdowinski, S. (2022). Accelerating sea-level rise and the fate of mangrove plant communities in South Florida, U.S.A. *Geomorphology*, 412, 108329. <https://doi.org/10.1016/j.geomorph.2022.108329>
- Parvathy, K., & Bhaskaran, P. (2017). Wave attenuation in presence of mangroves: A sensitivity study for varying bottom slopes. *The International Journal of Ocean and Climate Systems*, 8(3), 126–134. <https://doi.org/10.1177/1759313117702919>
- Pelckmans, I., Belliard, J.-P., Gourgue, O., Dominguez-Granda, L. E., & Temmerman, S. (2024). Mangroves as nature-based mitigation for ENSO-driven compound flood risks in a large river delta. *Hydrology and Earth System Sciences*, 28(6), 1463–1476. <https://doi.org/10.5194/hess-28-1463-2024>
- Pena-Regueiro, J., Sebastiá-Frasquet, M., Estornell, J., & Aguilar-Maldonado, J. (2020). Sentinel-2 Application to the Surface Characterization of Small Water Bodies in Wetlands. *Water*, 12(5), 1487. <https://doi.org/10.3390/w12051487>
- Pennings, S. C., Glazner, R. M., Hughes, Z. J., Kominoski, J. S., & Armitage, A. R. (2021). Effects of mangrove cover on coastal erosion during a hurricane in Texas, USA. *Ecology*, 102(4). <https://doi.org/10.1002/ecy.3309>

- Pham, T., Yokoya, N., Bui, D., Yoshino, K., & Friess, D. (2019). Remote Sensing Approaches for Monitoring Mangrove Species, Structure, and Biomass: Opportunities and Challenges. *Remote Sensing*, *11*(3), 230. <https://doi.org/10.3390/rs11030230>
- Pramudya, F. S., Pan, J., Devlin, A. T., & Lin, H. (2021). Enhanced Estimation of Significant Wave Height with Dual-Polarization Sentinel-1 SAR Imagery. *Remote Sensing*, *13*(1), 124. <https://doi.org/10.3390/rs13010124>
- Primavera, J., dela Cruz, M., Montilijao, C., Consunji, H., dela Paz, M., Rollon, R., Maranan, K., Samson, M., & Blanco, A. (2016). Preliminary assessment of post-Haiyan mangrove damage and short-term recovery in Eastern Samar, central Philippines. *Marine Pollution Bulletin*, *109*(2), 744–750. <https://doi.org/10.1016/j.marpolbul.2016.05.050>
- Primavera, J., Friess, D., Van Lavieren, H., & Lee, S. (2018, January). The mangrove ecosystem. In *World seas: An environmental evaluation volume iii: Ecological issues and environmental impacts* (pp. 1–34). Elsevier. <https://doi.org/10.1016/B978-0-12-805052-1.00001-2>
- Pronk, M., Hooijer, A., Eilander, D., Haag, A., de Jong, T., Voudoukas, M., Vernimmen, R., Ledoux, H., & Eleveld, M. (2024). DeltaDTM: A global coastal digital terrain model. *Scientific Data*, *11*(1), 273. <https://doi.org/10.1038/s41597-024-03091-9>
- Psomiadis, E., Diakakis, M., & Soulis, K. X. (2020). Combining SAR and optical earth observation with hydraulic simulation for flood mapping and impact assessment. *Remote Sensing*, *12*(23), 1–29. <https://doi.org/10.3390/rs12233980>
- Quang Bao, T. (2011). Effect of mangrove forest structures on wave attenuation in coastal Vietnam. *Oceanologia*, *53*(3), 807–818. <https://doi.org/10.5697/oc.53-3.807>
- Rivera-Monroy, V. H., Kristensen, E., Lee, S. Y., & Twilley, R. R. (2017, January). *Mangrove ecosystems: A global biogeographic perspective: Structure, function, and services*. Springer International Publishing. <https://doi.org/10.1007/978-3-319-62206-4>
- Rodriguez, A. F., Gerber, S., & Daroub, S. H. (2020). Modeling soil subsidence in a subtropical drained peatland. The case of the everglades agricultural Area. *Ecological Modelling*, *415*, 108859. <https://doi.org/10.1016/j.ecolmodel.2019.108859>
- Romañach, S. S., DeAngelis, D. L., Koh, H. L., Li, Y., Teh, S. Y., Raja Barizan, R. S., & Zhai, L. (2018, March). Conservation and restoration of mangroves: Global status, perspectives, and prognosis. <https://doi.org/10.1016/j.ocecoaman.2018.01.009>
- Saintilan, N., Khan, N. S., Ashe, E., Kelleway, J. J., Rogers, K., Woodroffe, C. D., & Horton, B. P. (2020). Thresholds of mangrove survival under rapid sea level rise. *Science*, *368*(6495), 1118–1121. <https://doi.org/10.1126/science.aba2656>
- Samuele, D. P., Federica, G., Filippo, S., & Enrico, B.-M. (2022). A simplified method for water depth mapping over crops during flood based on Copernicus and DTM open data. *Agricultural Water Management*, *269*, 107642. <https://doi.org/10.1016/j.agwat.2022.107642>
- Sánchez-Núñez, D., Mancera Pineda, J., & Osorio, A. F. (2020). From local-to global-scale control factors of wave attenuation in mangrove environments and the role of indirect mangrove wave attenuation. *Estuarine, Coastal and Shelf Science*, *245*, 106926. <https://doi.org/10.1016/j.ecss.2020.106926>
- Sanders, B. F., Wing, O. E. J., & Bates, P. D. (2024). Flooding is Not Like Filling a Bath. *Earth's Future*, *12*(12). <https://doi.org/10.1029/2024EF005164>
- SentiWiki. (2024). Sentinel-1. <https://sentiwiki.copernicus.eu/web/sentinel-1>
- Sheng, Y. P., & Zou, R. (2017). Assessing the role of mangrove forest in reducing coastal inundation during major hurricanes. *Hydrobiologia*, *803*(1), 87–103. <https://doi.org/10.1007/s10750-017-3201-8>
- Simard, M., Fatoyinbo, T., Smetanka, C., Rivera-Monroy, V., Castaneda, E., Thomas, N., & Van der Stocken, T. (2019). *Global Mangrove Distribution, Aboveground Biomass, and Canopy Height* (tech. rep.). ORNL DAAC. Oak Ridge Tennessee.
- Simard, M., Zhang, K., Rivera-Monroy, V. H., Ross, M. S., Ruiz, P. L., Castañeda-Moya, E., Twilley, R. R., & Rodriguez, E. (2006). Mapping Height and Biomass of Mangrove Forests in Everglades National Park with SRTM Elevation Data. *Photogrammetric Engineering & Remote Sensing*, *72*(3), 299–311. <https://doi.org/10.14358/PERS.72.3.299>
- Singh, M., & Schoenmakers, E. (2023). Comparative Impact Analysis of Cyclone Ana in the Mozambique Channel Using Satellite Data. *Applied Sciences*, *13*(7), 4519. <https://doi.org/10.3390/app13074519>

- Smith, R., & Montgomery, M. (2023). *Tropical Cyclones: Observations and basic processes* (Vol. 4). Elsevier.
- Smolders, S., Plancke, Y., Ides, S., Meire, P., & Temmerman, S. (2015). Role of intertidal wetlands for tidal and storm tide attenuation along a confined estuary: a model study. *Natural Hazards and Earth System Sciences*, 15. <https://doi.org/10.5194/nhess-15-1659-2015>, 2015
- Spalding, M., McIvor, A., Tonneijck, H., Tol, S., & van Eijk, P. (2014). *Mangroves for coastal defence Guidelines for coastal managers & policy makers* (tech. rep.). Wetlands International and The Nature Conservancy. www.nature.org.
- Spalding, M., & Parrett, C. L. (2019). Global patterns in mangrove recreation and tourism. *Marine Policy*, 110, 103540. <https://doi.org/10.1016/j.marpol.2019.103540>
- Stabenau, E., Engel, V., Sadle, J., & Pearlstine, L. (2011). Sea-level rise: Observations, impacts, and proactive measures in Everglades National Park. *Park Science*, 28(2).
- Tanaka, K. (2008). Effectiveness and limitation of the coastal vegetation for storm surge disaster mitigation. *Investigation report on the storm surge disaster by Cyclone Sidr in 2007, Bangladesh*.
- Tang, L., Liu, W., Yang, D., Chen, L., Su, Y., & Xu, X. (2018). Flooding Monitoring Application Based on the Object-oriented Method and Sentinel-1A SAR Data. *Journal of Geo Information Science*, 20, 377–384.
- Temmerman, S., Horstman, E. M., Krauss, K. W., Mullarney, J. C., Pelckmans, I., & Schoutens, K. (2022). Marshes and Mangroves as Nature-Based Coastal Storm Buffers. <https://doi.org/10.1146/annurev-marine-040422>
- Todd, M. J., Muneeppeerakul, R., Pumo, D., Azalee, S., Miralles-Wilhelm, F., Rinaldo, A., & Rodriguez-Iturbe, I. (2010). Hydrological drivers of wetland vegetation community distribution within Everglades National Park, Florida. *Advances in Water Resources*, 33(10), 1279–1289. <https://doi.org/10.1016/j.advwatres.2010.04.003>
- Tomlinson, P. B. (2016, October). *The Botany of Mangroves*. Cambridge University Press. <https://doi.org/10.1017/CBO9781139946575>
- Tran, T. V., Reef, R., & Zhu, X. (2022). A Review of Spectral Indices for Mangrove Remote Sensing. *Remote Sensing*, 14(19), 4868. <https://doi.org/10.3390/rs14194868>
- UCAR. (2024). How hurricanes form. <https://scied.ucar.edu/learning-zone/storms/how-hurricanes-form#:~:text=As%20it%20rises%2C%20the%20air, because%20of%20the%20Earth's%20rotation>.
- Uddin, K., Matin, M. A., & Meyer, F. J. (2019). Operational flood mapping using multi-temporal Sentinel-1 SAR images: A case study from Bangladesh. *Remote Sensing*, 11(13). <https://doi.org/10.3390/rs11131581>
- UN-SPIDER. (2025). Flood Mapping and Damage Assessment Using Sentinel-1 SAR Data in Google Earth Engine. <https://www.un-spider.org/advisory-support/recommended-practices/recommended-practice-google-earth-engine-flood-mapping/step-by-step#Step%208:%20Change%20detection>
- U.S. Geological Survey (USGS). (2024). *Annual National Land Cover Database (NLCD) Collection 1 Products* (tech. rep.).
- USGS. (2025). Everglades Depth Estimation Network. <https://sofia.usgs.gov/eden/index.php>
- van Bijsterveldt, C. E. J., Herman, P. M. J., van Wesenbeeck, B. K., Ramadhani, S., Heuts, T. S., van Starrenburg, C., Tas, S. A. J., Triyanti, A., Helmi, M., Tonneijck, F. H., & Bouma, T. J. (2023). Subsidence reveals potential impacts of future sea level rise on inhabited mangrove coasts. *Nature Sustainability*, 6(12), 1565–1577. <https://doi.org/10.1038/s41893-023-01226-1>
- van Zelst, V. T., Dijkstra, J. T., van Wesenbeeck, B. K., Eilander, D., Morris, E. P., Winsemius, H. C., Ward, P. J., & de Vries, M. B. (2021). Cutting the costs of coastal protection by integrating vegetation in flood defences. *Nature Communications*, 12(1). <https://doi.org/10.1038/s41467-021-26887-4>
- Van Coppelolle, R., Schwarz, C., & Temmerman, S. (2018). Contribution of Mangroves and Salt Marshes to Nature-Based Mitigation of Coastal Flood Risks in Major Deltas of the World. *Estuaries and Coasts*, 41(6), 1699–1711. <https://doi.org/10.1007/s12237-018-0394-7>
- Van Rooijen, A. A., McCall, R. T., van Thiel de Vries, J. S. M., van Dongeren, A. R., Reniers, A. J. H. M., & Roelvink, J. A. (2016). Modeling the effect of wave-vegetation interaction on wave setup. *Journal of Geophysical Research: Oceans*, 121(6), 4341–4359. <https://doi.org/10.1002/2015JC011392>

- Van Wesenbeeck, B. K., van Zelst, V. T. M., Antolinez, J. A. A., & de Boer, W. P. (2025). Quantifying uncertainty in wave attenuation by mangroves to inform coastal green belt policies. *Communications Earth & Environment*, 6(1), 258. <https://doi.org/10.1038/s43247-025-02178-4>
- Van Wesenbeeck, B. K., Wolters, G., Antolínez, J. A. A., Kalløe, S. A., Hofland, B., de Boer, W. P., Çete, C., & Bouma, T. J. (2022). Wave attenuation through forests under extreme conditions. *Scientific Reports*, 12(1), 1884. <https://doi.org/10.1038/s41598-022-05753-3>
- Vanama, V. S., Rao, Y. S., & Bhatt, C. M. (2021). Change detection based flood mapping using multi-temporal Earth Observation satellite images: 2018 flood event of Kerala, India. *European Journal of Remote Sensing*, 54(1), 42–58. <https://doi.org/10.1080/22797254.2020.1867901>
- Vitousek, S., Barnard, P. L., Fletcher, C. H., Frazer, N., Erikson, L., & Storlazzi, C. D. (2017). Doubling of coastal flooding frequency within decades due to sea-level rise. *Scientific Reports*, 7(1), 1399. <https://doi.org/10.1038/s41598-017-01362-7>
- von Storch, H., & Woth, K. (2008). Storm surges: perspectives and options. *Sustainability Science*, 3(1), 33–43. <https://doi.org/10.1007/s11625-008-0044-2>
- Vousdoukas, M. I., Voukouvalas, E., Mentaschi, L., Dottori, F., Giardino, A., Bouziotas, D., Bianchi, A., Salamon, P., & Feyen, L. (2016). Developments in large-scale coastal flood hazard mapping. *Natural Hazards and Earth System Sciences*, 16(8), 1841–1853. <https://doi.org/10.5194/nhess-16-1841-2016>
- Wang, J., Aouf, L., & Badulin, S. (2021). Retrieval of wave period from altimetry: Deep learning accounting for random wave field dynamics. *Remote Sensing of Environment*, 265, 112629. <https://doi.org/10.1016/j.rse.2021.112629>
- Wikimedia Commons Andrew Tappert. (2007a). Avicennia Germinans Everglades National Park. https://upload.wikimedia.org/wikipedia/commons/c/c5/Avicennia_germinans-everglades_natl_park.jpg
- Wikimedia Commons Andrew Tappert. (2007b). Red mangrove Everglades National Park. https://en.wikipedia.org/wiki/File:Red_mangrove-everglades_natl_park.jpg#filelinks
- Wingard, G. L., Bergstresser, S. E., Stackhouse, B. L., Jones, M. C., Marot, M. E., Hoefke, K., Daniels, A., & Keller, K. (2020). Impacts of Hurricane Irma on Florida Bay Islands, Everglades National Park, USA. *Estuaries and Coasts*, 43(5), 1070–1089. <https://doi.org/10.1007/s12237-019-00638-7>
- Worthington, T., Andradi-Brown, D., Bhargava, R., Buelow, C., Bunting, P., Duncan, C., Fatoyinbo, L., Friess, D., Goldberg, L., Hilarides, L., Lagomasino, D., Landis, E., Longley-Wood, K., Lovelock, C., Murray, N., Narayan, S., Rosenqvist, A., Sievers, M., Simard, M., ... Spalding, M. (2020, May). Harnessing Big Data to Support the Conservation and Rehabilitation of Mangrove Forests Globally. <https://doi.org/10.1016/j.oneear.2020.04.018>
- Worthington, T., & Spalding, M. (2014). *Mangrove Restoration Potential* (tech. rep.). USDA Forest Service. www.globalmangrovetwatch.org
- Worthington, T., Zu Ermgassen, P., Friess, D., Krauss, K., Lovelock, C., Thorley, J., Tingey, R., Woodroffe, C., Bunting, P., Cormier, N., Lagomasino, D., Lucas, R., Murray, N., Sutherland, W., & Spalding, M. (2020). A global biophysical typology of mangroves and its relevance for ecosystem structure and deforestation. *Scientific Reports*, 10(1). <https://doi.org/10.1038/s41598-020-71194-5>
- Xie, D., Schwarz, C., Kleinhans, M. G., Zhou, Z., & van Maanen, B. (2022). Implications of Coastal Conditions and Sea Level Rise on Mangrove Vulnerability: A Bio-Morphodynamic Modeling Study. *Journal of Geophysical Research: Earth Surface*, 127(3). <https://doi.org/10.1029/2021JF006301>
- Yancho, J. M. M., Jones, T. G., Gandhi, S. R., Ferster, C., Lin, A., & Glass, L. (2020). The google earth engine mangrove mapping methodology (Geemmm). *Remote Sensing*, 12(22), 1–35. <https://doi.org/10.3390/rs12223758>
- Yu, M., & Gao, Q. (2024). Assessment of Surface Inundation Monitoring and Drivers after Major Storms in a Tropical Island. *Remote Sensing*, 16(3), 503. <https://doi.org/10.3390/rs16030503>
- Zhang, Liu, H., Li, Y., Xu, H., Shen, J., Rhome, J., & Smith, T. J. (2012). The role of mangroves in attenuating storm surges. *Estuarine, Coastal and Shelf Science*, 102-103, 11–23. <https://doi.org/10.1016/j.ecss.2012.02.021>
- Zhang, Wdowinski, Oliver-Cabrera, Koirala, Jo, & Osmanoglu. (2018). Mapping the extent and magnitude of severe flooding induced by hurricane Irma with multi-temporal Sentinel-1 SAR and

- InSAR observations. *International Archives of the Photogrammetry, Remote Sensing and Spatial Information Sciences - ISPRS Archives*, 42(3), 2237–2244. <https://doi.org/10.5194/isprs-archives-XLII-3-2237-2018>
- Zscheischler, J., Westra, S., van den Hurk, B. J. J. M., Seneviratne, S. I., Ward, P. J., Pitman, A., AghaKouchak, A., Bresch, D. N., Leonard, M., Wahl, T., & Zhang, X. (2018). Future climate risk from compound events. *Nature Climate Change*, 8(6), 469–477. <https://doi.org/10.1038/s41558-018-0156-3>

Additional theory

A.1. Mangroves

A.1.1. Distribution

Mangroves can typically be found between latitudes of 30° N and 30° S (Primavera et al., 2018). Their worldwide distribution is thought to be constrained by major ocean currents and the 20°C seawater isotherm during winter months (Giri et al., 2011). Zooming in on a typical mangrove environment, these habitats are often protected from strong wind and sea waves (Das et al., 2022). Mangroves thrive in intertidal zones, areas located between mean sea level (MSL) and the high-water mark, along coastlines, river deltas and estuarine systems (Giri et al., 2011). They are situated in tropical climates with minimal seasonality, resulting in high humidity and stable temperatures (Das et al., 2022). Annual temperature of mangrove habitat averages typically between 27°C and 30°C, providing the right climatic conditions (Das et al., 2022).

Globally, the total area of mangroves in 2020 was estimated at 147,359 km², with a 3.4% loss compared to 1996, as reported by Bunting et al. (2022). This estimate is based on data from the the Global Mangrove Watch, which detected mangrove cover with L-band Synthetic Aperture Radar (SAR) data with an accuracy of 87.4% (Bunting et al., 2022). The majority of mangroves are situated in Southeast Asia, where also 47% of the total net mangrove loss occurred (Bunting et al., 2022). Overall, Western Asia, Eastern Asia, and the Caribbean experienced the largest percentage of mangrove losses (Bunting et al., 2022). Bunting et al. (2022) notes that mangrove losses between 1996 and 2020 were twice as large as mangrove growth but highlights that losses were particularly high at the start of this period, indicating that the rate of mangrove loss may have decelerated. Despite this, Giri et al. (2011) emphasizes that mangrove ecosystems remain highly vulnerable to various threats, with their total global coverage now reduced to less than half of its historical extent (Giri et al., 2011).

A.1.2. Classification

Mangrove species have created specific strategies and adaptations to navigate their environmental challenges, resulting in the presence of different species in distinct ecological settings (Primavera et al., 2018, Das et al., 2022). Key environmental pressures driving these adaptations include tidal inundation and the linked varying salinity levels (Primavera et al., 2018). Despite this range of evolutionary developments, only a relatively small number of mangrove species have been described, with estimates ranging from 60 to 70 species (Primavera et al., 2018). Yet, the number of recognized mangrove species differs across the literature, largely due to their unconventional taxonomic classification (Hamilton, 2020). As shown in Figure 2.1, the Indo-West Pacific region has a higher species diversity than the Atlantic-East Pacific region (Das et al., 2022, Rivera-Monroy et al., 2017).

Among the most common species are the red mangrove (*Rhizophora*) and the black mangrove (*Avicennia*) (Romañach et al., 2018, Duke et al., 2002). A primary distinction between these species lies in their root systems, which are crucial to their ecological function and hydrodynamic resilience. *Rhizophora* species are characterized by their prop roots, which form a dense, criss-crossing network above the ground (Mclvor et al., 2012a). These roots provide stability in soft substrates and play a role in wave attenuation by creating drag forces that dissipate wave energy. This makes *Rhizophora* an effective pioneer species. *Avicennia* species possess pneumatophores, which are vertical, straw-like roots extending 20–30 cm above the soil surface (Mclvor et al., 2012a). These structures facilitate air exchange in oxygen-poor environments, enabling *Avicennia* to thrive seaward.

The zonation of these species on a coastal cross-section is governed by biotic and abiotic factors, such as tidal inundation patterns and salinity (Tomlinson, 2016). The specific zonation differs per region. In the Atlantic-East Pacific region, *Rhizophora* can typically be found in the lower coastal areas, where its prop roots help stabilize against tidal forces, acting as a coastal buffer. *Avicennia* is generally found higher up the coastal zone (Feller and Sitnik, 1996). Conversely, in the Indo-West Pacific region, the *Avicennia* is often a pioneer and grows at the most seaward position (Feller and Sitnik, 1996).

Another approach to classifying mangroves is based on their coastal type, presented by Worthington, Zu Ermgassen, et al. (2020), who categorize mangroves based on their geomorphic setting, which defines their spatial distribution. This classification divides mangrove coasts into four main types: open coast, lagoonal coast, deltaic coast, and estuarine coast (Worthington, Zu Ermgassen, et al., 2020).

Open coast (21.0% of global mangrove forests, 28,493 km²)

Open coasts are wave-dominated systems. However, because mangroves require relatively mild hydrodynamic conditions, they are often found in somewhat sheltered locations (Worthington, Zu Ermgassen, et al., 2020). These coasts typically feature an uninterrupted shoreline, with absence of rivers and channels, with no major fluvial sediment input shaping the coastal morphology (Bosboom & Stive, 2023). The primary sediment source is marine-derived (Bosboom & Stive, 2023). Open coasts often have a steeper continental shelf, which limits storm surge enhancement compared to shallower coastal settings.

Lagoonal coast (11.0% of global mangrove forests, 14,993 km²)

Lagoonal coasts are also wave-influenced but experience greater protection from barrier systems. These barriers, which form parallel to the coastline (Worthington, Zu Ermgassen, et al., 2020), provide shelter, creating shallow and calm conditions. Similar to open coasts, rivers and channels are limitedly present, and the primary sediment source is marine deposition (Bosboom & Stive, 2023). However, the shallow nature of lagoons makes them more prone to storm surge, as water can accumulate and inundate the coast more easily.

Estuarine coast (27.5% of global mangrove forests, 37,411 km²)

Estuarine coasts are tidally dominated environments, typically exhibiting a funnel-shaped morphology with tidal flows in both directions (Worthington, Zu Ermgassen, et al., 2020). These systems often have large catchment areas, and experience high levels of precipitation (Worthington, Zu Ermgassen, et al., 2020). Due to their estuarine nature, sediment dynamics are influenced by a combination of tidal transport, river discharge, and marine processes.

Deltaic coast (40.5% of global mangrove forests, 54,972 km²)

Deltaic coasts are river-dominated environments, characterized by extensive fluvial sediment deposition that forms “fan-shaped alluvial plains” (Worthington, Zu Ermgassen, et al., 2020). These coasts have numerous channels, which allow storm surges to penetrate far inland. Unlike wave-dominated systems, river and tidal forces play a much greater role in shaping deltaic mangrove forests. The shallow coastal shelf and channelized landscape have the ability to enhance storm surge propagation.

A.1.3. Ecosystem services

Mangroves provide a wide range of ecosystem services to humans and its surrounding environment (Hawkins, 2020). The diverse services mangroves provide can typically be divided into four categories: provisioning, regulating, supporting, and cultural services (Spalding et al., 2014).

Provisioning ecosystem services include food and water resources, as mangroves act as breeding grounds for fish, crabs, shrimps, and oysters, making them productive fishing areas that support the livelihoods of tens of millions of people (Spalding et al., 2014). In addition, mangroves provide essential resources, such as timber used for construction, fuel, and other products. The dense, durable wood from mangroves has long been valued for building houses and producing charcoal, supporting local economies and generating employment opportunities (Spalding et al., 2014).

Regulating ecosystem services involve coastal protection, as mangroves help prevent coastlines from eroding and reduce short wave and storm surge energy (Spalding et al., 2014, Worthington, Andradi-Brown, et al., 2020). Their intricate root systems gather and stabilize sediments, while dissipating wave energy and therefore providing protection from extreme weather events (Bosboom and Stive, 2023).

Supporting ecosystem services offered by mangroves include water purification and carbon storage. Mangroves help filter pollution in estuaries through algae and bacteria, which remove toxins from the water (Spalding et al., 2014). Additionally, mangroves play a crucial role in long-term carbon sequestration, as their waterlogged, anaerobic, and saline soils allow them to store carbon for millennia (Spalding et al., 2014). Mangrove forests can store up to four times more carbon than terrestrial tropical forests, making them essential for climate regulation (Worthington, Andradi-Brown, et al., 2020).

Cultural ecosystem services include the spiritual and recreational value of mangroves. They offer opportunities for tourism, with activities such as boating and wildlife watching being particularly popular (Worthington, Andradi-Brown, et al., 2020). These cultural and recreational benefits add to the overall importance of mangroves for coastal communities and economies.

A.1.4. Threats

Mangroves are currently facing numerous threats, both anthropogenic and natural, that have accelerated their degradation and loss worldwide (Granek and Ruttenberg, 2007).

Land cover conversion

One of the primary drivers of mangrove deforestation has been land use changes, particularly the conversion of mangrove areas for aquaculture. This phenomenon, especially prevalent since the 1970s, has been responsible for substantial mangrove loss, particularly in Southeast Asia and South America (Worthington and Spalding, 2014, Friess et al., 2019). In these regions, more than 50% of the mangrove forests have been converted to aquaculture ponds (Friess et al., 2019). As Bosboom and Stive (2023) note, reforestation is challenging due to the vulnerability of young mangrove trees and the degradation of local ecosystems.

Agricultural expansion also contributes to the deforestation of mangroves. Throughout Southeast Asia, Africa, and South America, substantial mangrove areas have been cleared to make way for growing rice and coconuts (Worthington and Spalding, 2014, Friess et al., 2019). This is a trend seen across tropical regions, where the demand for agricultural land often surpasses the need to conserve mangrove ecosystems (Friess et al., 2019).

Urbanization and infrastructure development along coastlines have also contributed to mangrove loss. Coastal cities have seen mangrove destruction to make room for expanding cities, ports, and other infrastructure (Worthington and Spalding, 2014). This type of development typically leads to the clearing of mangrove forests, which can then no longer protect the coastline from erosion and flooding (Worthington and Spalding, 2014). As the population density in these regions is expected to increase significantly in the coming decades, so too will the pressure on coastal ecosystems, including mangroves, for urban development and agriculture. This growth heightens the risk of flooding, increasing the need for sustainable coastal management strategies to protect both human communities and mangrove ecosystems (Van Coppenolle et al., 2018).

Overexploitation

Overexploitation of mangroves for timber, fuelwood, and charcoal has also led to large-scale deforestation, particularly in regions like Africa, Latin America, and parts of Southeast Asia (Friess et al., 2019). This leaves many areas vulnerable to erosion (Friess et al., 2019).

Climate change and subsidence

Climate change poses a significant threat to mangrove ecosystems. Two key aspects of climate change, sea level rise and the increasing severity of tropical storms, are particularly impactful. Sea level rise (SLR) can destabilize mangrove ecosystems by causing permanent inundation of their habitats (Parkinson and Wdowinski, 2022). For example, Parkinson and Wdowinski (2022) predict that, due to accelerating SLR, the majority of South Florida's mangrove ecosystems will be submerged by 2100. However, as Xie et al. (2022) highlight, the impact of SLR is site-specific, depending on locally varying factors such as waves, tides and sediment availability. Whether sedimentation occurs, and thus whether mangroves have the ability to adapt to rising seas, depends on the local interplay between SLR, tidal dynamics, wave activity, and mangrove growth or decline (Xie et al., 2022). In micro-tidal environments, even small amounts of SLR can lead to mangrove retreat, whereas in macro-tidal environments, with generally stronger waves and tides, mangroves tend to establish higher up the coastline, extending the timeline before SLR becomes a critical factor (Xie et al., 2022). Despite these site-specific nuances,

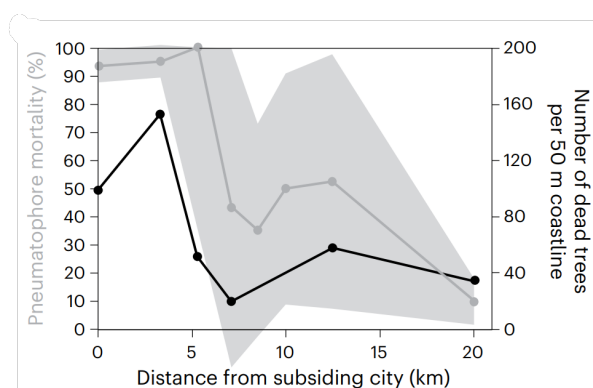


Figure A.1: This graph illustrates the relationship between distance from a subsiding city and mangrove mortality. Pneumatophore mortality (%) (gray line, left axis) and tree mortality per 50 m of coastline (black line, right axis) were measured along a distance from a subsiding city. The results show that higher water depths due to RSLR, which align with the distance from the subsiding city, correspond to increased mortality (van Bijsterveldt et al., 2023)

the vulnerability of mangroves to SLR is evident. As emphasized by Saintilan et al. (2020), mangroves are likely unable to keep up with a relative SLR higher than 6.1 mm per year. It cannot be ruled out that this limit is exceeded in the tropics in a high-emission scenario (Saintilan et al., 2020).

Furthermore, climate change is expected to increase the severity of tropical storms (Van Coppenolle et al., 2018). Stronger storms lead to more extensive flooding, which works on top of the impacts of sea level rise by further disrupting mangrove habitat conditions. Moreover, tropical storms can cause severe damage to mangrove forests. For example, Typhoon Haiyan in the Philippines generated a storm surge of 7.4 meters, leading to tree mortality in mangrove forests directly impacted by the storm, as researched by Primavera et al. (2016). However, mangroves also exhibit natural resilience, as sprouts and seeds can emerge in the aftermath of a storm, supporting forest recovery (Primavera et al., 2016). As a result of climate change, the combination of rising sea levels with increasingly severe storms increases the vulnerability of mangrove ecosystems (McIvor et al., 2015).

Adding on to the mentioned effects of climate change, subsidence further poses a threat to mangrove forests through relative sea level rise (RSLR), which combines both land sinking and rising sea levels. Subsidence refers to the settling of the Earth's surface, caused by both natural processes and human activities, with groundwater extraction being a major contributor. van Bijsterveldt et al. (2023) measured subsidence rates of 8 to 20 cm per year along a 20-kilometer coastline near Semarang, Central Java, Indonesia.

While mangroves can adapt to RSLR to a certain extent, their ability to do so depends on sediment availability and sediment deficits are often the reality (van Bijsterveldt et al., 2023). In response to higher water levels caused by subsidence, mangroves attempt to adapt by elongating their pneumatophores and developing new root structures, as van Bijsterveldt et al. (2023) points out. van Bijsterveldt et al. (2023) demonstrated that mangroves can tolerate RSLR rates of up to 4.3 cm per year if sufficient sediment is present. However, when sediment supply is inadequate, the forest cannot keep pace with RSLR rates larger than the previously mentioned 6.1 mm per year, leading to mangrove retreat (Saintilan et al., 2020; van Bijsterveldt et al., 2023). The impact of subsidence on mangrove forests is evident in tree and pneumatophore mortality on the seaward side of the forest, shown in Figure A.1 (van Bijsterveldt et al., 2023). Ultimately, the lateral erosion caused by subsidence threatens both mangrove ecosystems and the coastal communities that rely on them (van Bijsterveldt et al., 2023).

A.2. Tropical storms

As mangroves are located in the tropical zone, it is relevant to look at tropical storms specifically. In general, tropical storms are weather systems that are created over warm ocean waters in the tropical zone (McIvor et al., 2015). As summarized by von Storch and Woth (2008), tropical cyclones “are huge, thermodynamic machines that transform heat, mainly sucked from a very warm sea surface, into kinetic energy, i.e., wind” (von Storch and Woth, 2008, p34).

A.2.1. Physical conditions

For a tropical storm to develop, the following key ingredients must be present (UCAR, 2024):

1. High ocean temperatures
2. Warm, moisture-rich atmospheric air
3. Low air pressure
4. Low wind shear

These conditions are typically found near the equator, between latitudes 5° and 20° , where ocean temperatures exceed 26.5°C (McIvor et al., 2012b). However, tropical storms cannot form directly at the equator due to the lack of a Coriolis effect, which is essential for the rotation of the storm (UCAR, 2024). The mentioned latitudes present the ideal balance between warm ocean waters, where air rises, and enough Coriolis force to create the low pressure areas (Needham and Keim, 2011).

Tropical storms develop through two distinct stages, beginning with the genesis stage. During this stage, tropical disturbances form and evolve into tropical depressions (Fitzpatrick, 1999). A tropical disturbance refers to a collection of thunderstorms over the ocean that persists for at least 24 hours (Fitzpatrick, 1999). These disturbances arise in regions where air converges, forcing it to rise due to the lack of an outlet for downward movement (Fitzpatrick, 1999). As the air rises, it cools, leading to the condensation of water vapor into clouds (UCAR, 2024). The Coriolis effect then applies a rotational motion to the rising air, creating the characteristic circular pattern of tropical storms (UCAR, 2024). The system is classified as a tropical depression once the spread out thunderstorms form together into a closed circulation with wind speeds below 17 m/s (Smith and Montgomery, 2023). The genesis stage often spans several days (Fitzpatrick, 1999).

The second stage of tropical storm development is the intensification stage, during which a tropical depression evolves into a tropical storm, and ultimately a hurricane (Fitzpatrick, 1999). If the key ingredients persist, the tropical depression can intensify into a tropical storm. As energy is continuously transferred from the warm ocean to the atmosphere, the air warms further, creating a low-pressure center. This draws in surrounding air, as air naturally moves from areas of higher to lower pressure (Fitzpatrick, 1999). This process generates a positive feedback loop: the warming of the vertical column of air reduces pressure at the storm center, which in turn pulls in more air at lower levels, further strengthening the cyclonic system (Fitzpatrick, 1999). As this feedback loop continues, the storm intensifies, becoming a tropical storm with wind speeds between 17 and 32 m/s, and eventually a hurricane when wind speeds exceed 33 m/s (Smith and Montgomery, 2023).

As noted earlier, tropical storms derive their energy from warm ocean waters and the surrounding atmospheric air. When a storm moves over land or cooler ocean waters, it loses strength due to the reduction of its main energy source (UCAR, 2024). When a storm reaches land, it is referred to as making landfall. Although a storm's intensity decreases upon landfall, it can still deliver significant amounts of precipitation that extend far inland (Smith and Montgomery, 2023).

Climate change impacts the severity of tropical storms, though its effect on their frequency is minimal (IPCC, 2021; Krauss & Osland, 2019). According to IPCC (2021), the energy sources that fuel tropical storms, warm ocean waters and warm, moist air, are amplified by climate change. Warmer oceans and air contribute to stronger winds (Murakami et al., 2018). An increase in atmospheric moisture results in heavier rainfall, as warmer air can hold more water vapor (IPCC, 2021).

A.2.2. Classification of tropical storms

The naming of tropical storms depends on their geographic location (Fitzpatrick, 1999). In the Atlantic and Northern Pacific, they are referred to as hurricanes. In the Northwest Pacific, they are called typhoons, and in the South Pacific and Indian Ocean, they are known as cyclones. Tropical storms are further categorized by their intensity, defined as the maximum sustained wind speed near the surface (Smith and Montgomery, 2023). The Saffir-Simpson Hurricane Wind Scale is most often used for this purpose, shown in Figure A.2 (McIvor et al., 2015, Smith and Montgomery, 2023).

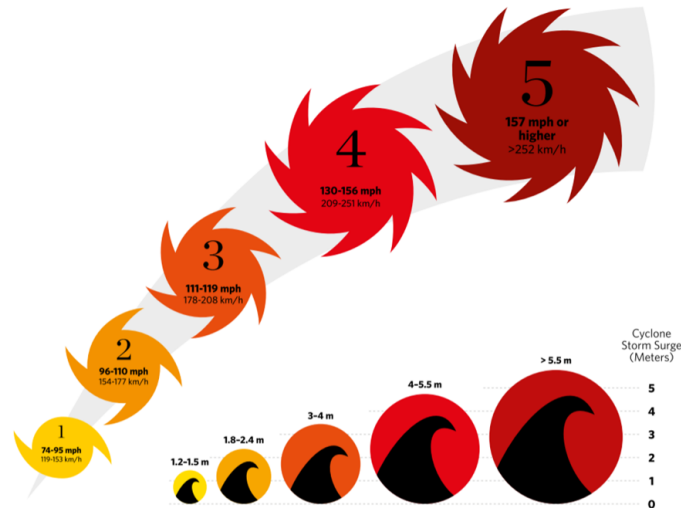


Figure A.2: Relationship between wind speed categories and storm surge heights based on the Saffir-Simpson Hurricane Wind Scale. The figure illustrates the five intensity levels, ranging from Category 1 (119–153 km/h) to Category 5 (≥ 252 km/h), along with their associated storm surge heights. Higher wind speeds generally correspond to greater surge levels, though variability exists (Herrera-Silveira et al., 2022).

A.2.3. Consequences of tropical storms

Tropical storms can cause damage through winds, rainfall, surge, and waves (Nelson, 2014). Each of these three elements has distinct impacts. Strong winds can damage buildings, agricultural land, and natural areas. Heavy rainfall can inundate low-lying regions and cause rivers to overflow their banks, leading to flooding. Storm surges, on the other hand, result in coastal flooding, posing a threat to people living in coastal areas, coastal infrastructure and ecosystems, which is often accompanied by short wind waves traveling on top of the surge.

The extent of the damage following from tropical storms depends on several factors, including the storm's category (wind speed), its direction, and its duration (Nelson, 2014). Higher wind speeds typically lead to more destruction, while the angle of the storm's path affects the scale and location of damage. Finally, the duration of the storm plays a critical role; the longer a storm persists, the greater the cumulative damage it can cause (Nelson, 2014).

Furthermore, it is crucial to examine the specific effects of tropical storms on mangrove forests. Tropical storms can cause substantial damage to mangrove forests due to the combined effects of high wind speeds, storm surge, waves, and water ponding (Krauss & Osland, 2019; Mo et al., 2023). According to Mo et al. (2023), storm intensity plays a crucial role in determining mangrove damage. The extent of damage shows high spatial variability as it not only depends on storm factors, such as distance to the storm center, the storm pathway and previous storm events, but also on geomorphological and ecological parameters (Krauss & Osland, 2019). Notably, mangrove species seem to exhibit different levels of storm resilience (Mo et al., 2023). While mangroves have the potential to recover from tropical storms over time, severe storms can result in tree mortality and large-scale forest degradation (Krauss & Osland, 2019). The risk of mangrove damage due to tropical storms is further influenced by climate change, with regional variations in storm intensity affecting mangrove ecosystems in diverse ways (Mo et al., 2023).

A.2.4. Flood types

Tropical storms can bring winds, rainfall, waves, and storm surges. These drivers can lead to different types of floods: *coastal flooding* caused by storm surges and short waves, *pluvial flooding* due to heavy rainfall, and *fluvial flooding* from river overflow (Nasr et al., 2021). When two or more of the flood types occur at the same time it is referred to as compound flooding (Eilander et al., 2023). Zscheischler et al. (2018) define compound events as “the combination of multiple drivers and/or hazards that together increase societal or environmental risk.” In the low-lying coastal areas where mangroves are situated,

it is particularly challenging to analyze the specific contributions of pluvial, fluvial, and coastal flooding to the overall flood extent, especially when regarding mangrove contribution to flood reduction (Bates et al., 2021). Only recent studies (Eilander et al., 2023), have developed globally applicable models to account for compound flooding, highlighting the complexity of understanding its impacts.

As Pelckmans et al. (2024) demonstrated in estuaries, it is important to recognize that mangroves primarily have an impact on coastal flooding, with limited impact on fluvial flooding (Pelckmans et al., 2024). Therefore, when interpreting detected flood extents through remote sensing, it should be taken into account that there might be parts of the flood extent on which mangroves could not have much impact.

A.3. Coastal flooding

A.3.1. Coastal flooding without mangroves

In the absence of mangroves, the individual hydrodynamic elements contributing to the total water level (TWL) are discussed. A more detailed examination of storm surge, set-up and run-up is provided in the main text, as these are specifically enhanced by tropical storms. These elements together can contribute to coastal flood extent.

Sea-level rise

Sea-level rise (SLR) presents a long-term element that alters the mean sea level (MSL). Yet, its contribution to the TWL can vary regionally and temporally as short-term, smaller-scale fluctuations such as tides and waves may dominate over local SLR effects (Vitousek et al., 2017). The impact of SLR depends on its ratio to the tidal range and surge height, influencing how strongly it affects different regions. In areas with milder tidal climates, such as the tropics where mangroves are predominantly located, smaller tides may result in SLR having a greater relative effect (Vitousek et al., 2017). Nonetheless, in hurricane-prone areas such as the Caribbean Sea and the Gulf of Mexico, the effect of extreme weather events is still likely to overshadow the effects of SLR (Vitousek et al., 2017). The magnitude of SLR is subject to uncertainty, as reflected in the diverging scenarios outlined in the IPCC report (IPCC, 2023). Projections for 2100 indicate an increase varying between 0.28 m to 1.02 m relative to the 1995–2014 average (IPCC, 2023, Bosboom and Stive, 2023).

Tide

In addition to SLR, the *tide* causes periodic fluctuation of the TWL. The tide results from the gravitational interactions between the earth and the moon and the earth and the sun (Bosboom and Stive, 2023). Tides are predominantly classified as either semi-diurnal, with two high and two low tides occurring every 24 hours, or diurnal, with one high and one low tide within the same period (Bosboom and Stive, 2023). Tides influence coastal flood extent, as higher water levels during high tide allow the TWL to reach further inland compared to low tide, thereby impacting the extent of flooding along the coast.

Seasonal climate anomalies

Furthermore, various *seasonal climate anomalies*, driven by teleconnection patterns, add to the TWL (Vitousek et al., 2017). Among these patterns, the El Niño-Southern Oscillation (ENSO) is the most well-known. ENSO-related deviations in MSL arise from the interactions between global atmospheric circulation changes and oceanic processes, which influence water temperature, wind patterns, and precipitation (NOAA, 2024). In particular, changes in water temperature lead to thermal expansion, resulting in SLR. This effect is especially pronounced in regions such as Peru and Ecuador, where ENSO events can cause sea-level increases of 40 cm, contributing to potential coastal flooding (Pelckmans et al., 2024).

Surge

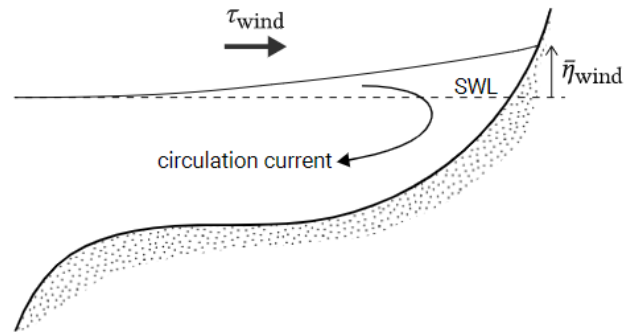


Figure A.3: Wind-driven surge during a tropical storm. The elevated water level at the coast balances the wind shear stress (Bosboom & Stive, 2023).

Wave set-up

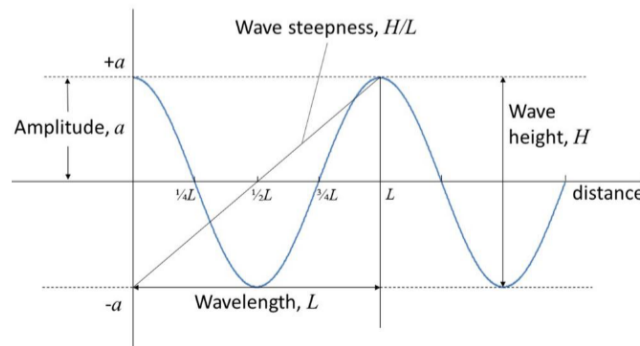


Figure A.4: Illustration of the characteristics of a linear short wave (McIvor et al., 2012a). The wave is described by its wave height (H), which is the vertical distance between the crest and the trough, and its amplitude (a), which represents half of the wave height. The wavelength (L) denotes the horizontal distance between two consecutive wave crests. The wave steepness (H/L) is a key parameter that influences wave breaking and energy dissipation.

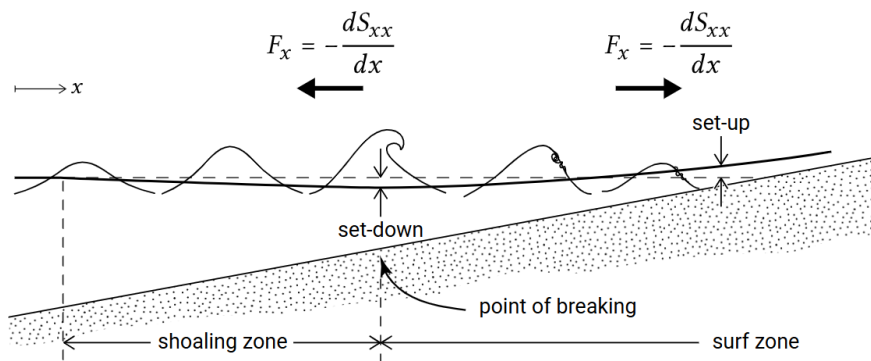


Figure A.5: Schematic illustration of wave set-up resulting from gradients in radiation stresses due to wave breaking (Bosboom & Stive, 2023).

A.3.2. Coastal flooding with mangroves

Surge attenuation by mangroves

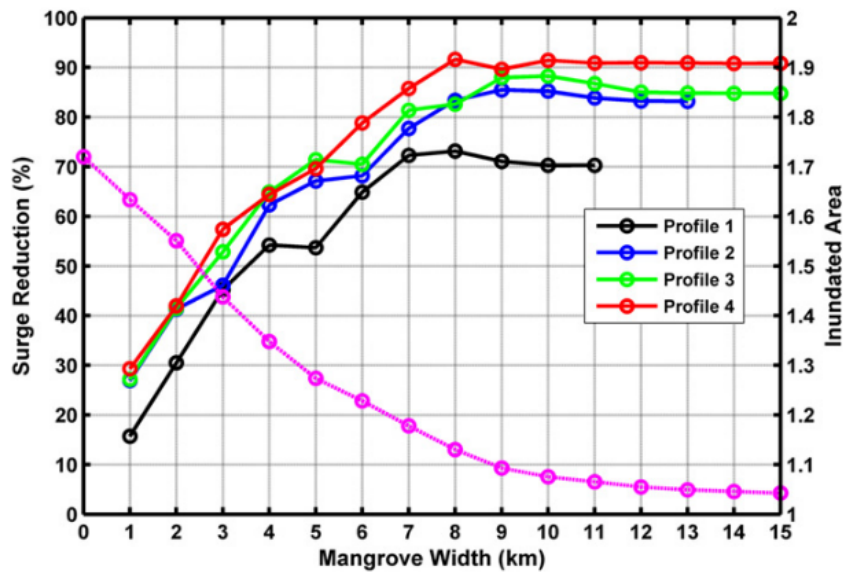


Figure A.6: Relation between mangrove forest width and reduction in storm surge height and inundated area for four different shoreline profiles along the Gulf Coast of South Florida, United States during Hurricane Wilma in 2005 (Zhang et al., 2012). The maximum surge height across the four sites reached approximately 4 meters. The graph illustrates that wider mangrove forests result in greater surge height- and inundated area reduction, with the most significant attenuation occurring within the first few kilometers of the forest. This relationship is non-linear as the rate of reduction decreases as forest width increases.

Short wave attenuation by mangroves

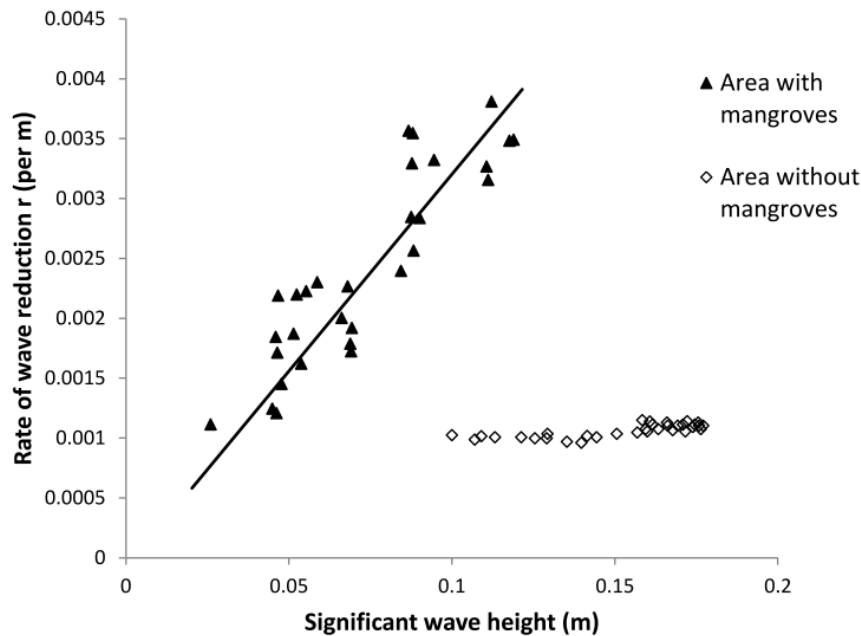


Figure A.7: Relation between incoming significant wave height and wave attenuation rate when water levels are at branch and leaf height, based on measurements from Mazda et al. (2006) (McIvor et al., 2012a). The results indicate that for small waves with significant wave heights ranging between 11 and 16 cm, when the water level reaches the branches and leaves of mangrove trees, the rate of wave attenuation is higher for larger incoming wave heights in areas with mangroves, while areas without mangroves show consistently low attenuation rates.

How much wave energy is attenuated by 100 m of mangrove forest?

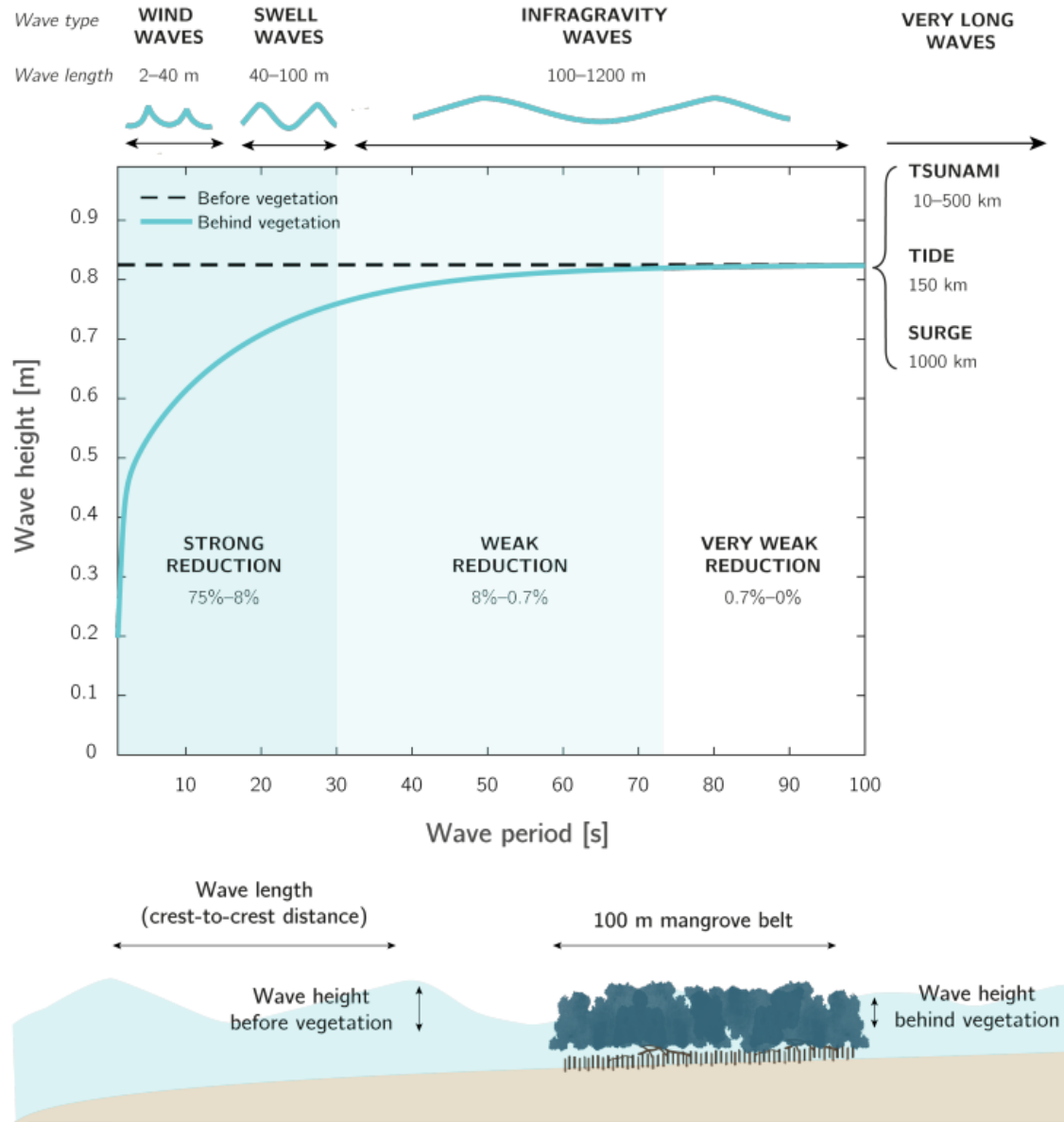


Figure A.8: Wave attenuation by a 100 m wide mangrove forest as a function of wave period and wavelength (Gijón Mancheño, 2022). The figure demonstrates that shorter-period waves (e.g., wind and swell waves) experience stronger attenuation, whereas longer-period waves are attenuated less effectively. This highlights the dependence of wave energy dissipation on wave length, emphasizing the effectiveness of mangroves in reducing short-wave energy.

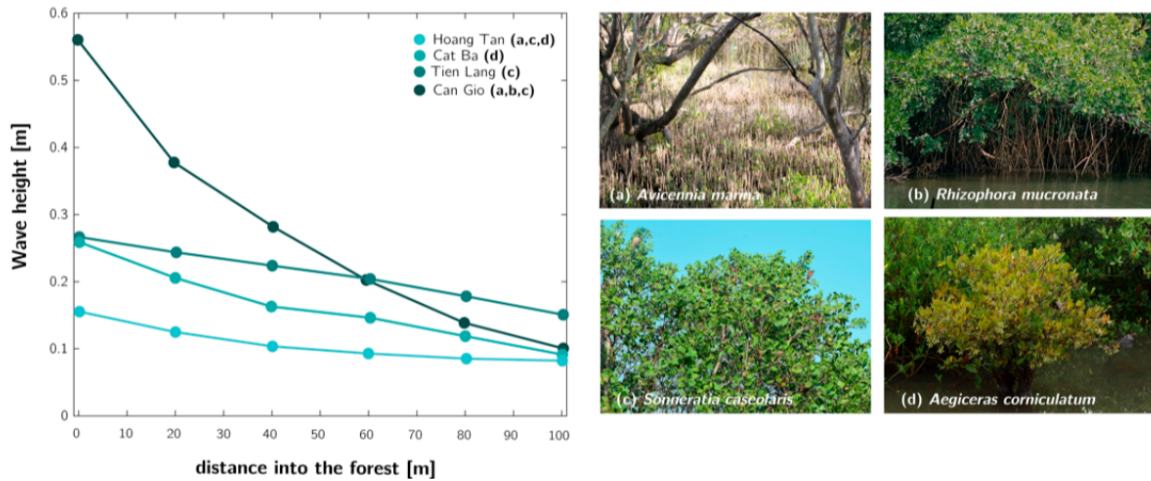


Figure A.9: Relation between forest width and short wave height reduction at four different sites: Cat Ba, Hoang Tan, Tien Lang, and Can Gio (Gijón Mancheño et al., 2021; Quang Bao, 2011). The graph illustrates that as waves travel deeper into the mangrove forest, their height progressively decreases. However, it can be seen that wave attenuation is not only dependent on forest width; it is also influenced by the characteristics of the mangrove forest, including tree density, vegetation height, and species composition (Gijón Mancheño et al., 2021).

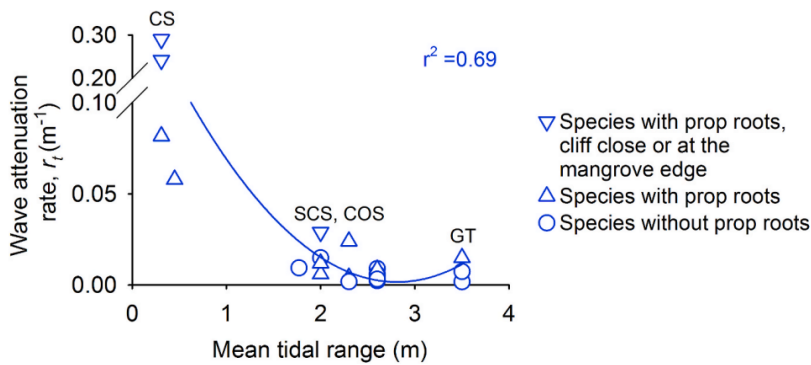


Figure A.10: Relation between wave attenuation rate and mangrove root type (Sánchez-Núñez et al., 2020). The graph illustrates how the wave attenuation rate is influenced by the root structure of mangrove species. Mangroves with prop roots (e.g., *Rhizophora*) exhibit higher attenuation rates compared to species without prop roots (e.g., *Avicennia*, which have pneumatophores).

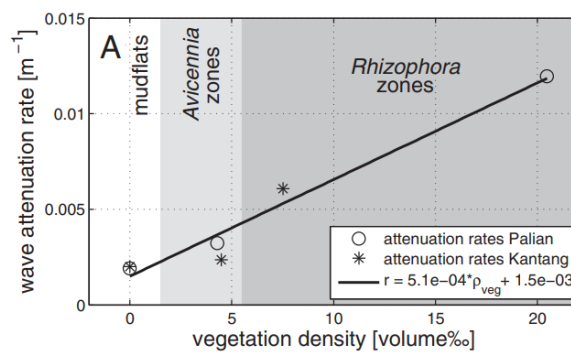


Figure A.11: Relation between wave attenuation rate and vegetation density (Horstman et al., 2014). The graph illustrates that wave attenuation rate increases with higher vegetation density, demonstrating the positive correlation between forest density and wave energy dissipation. The transition from *Avicennia* to *Rhizophora* zones further emphasizes the role of species-specific structures in wave attenuation.

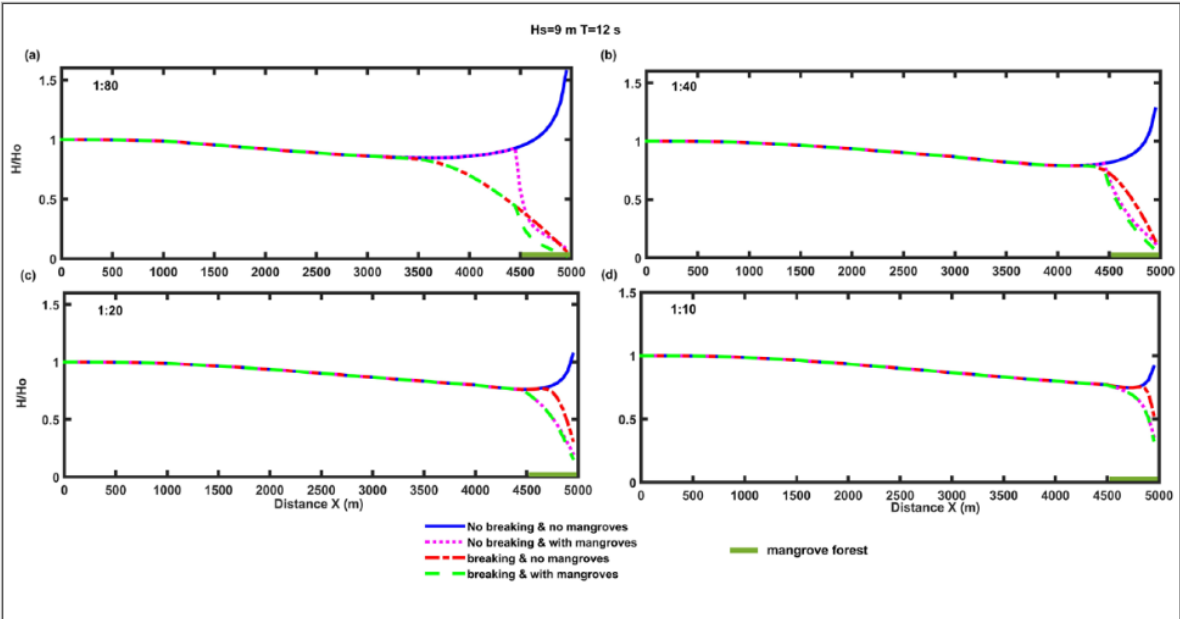


Figure A.12: Wave height reduction for different slopes under breaking and non-breaking wave conditions, with and without mangroves: (a) 1:80, (b) 1:40, (c) 1:20, and (d) 1:10 (Parvathy and Bhaskaran, 2017). The results show that milder slopes facilitate greater wave attenuation due to prolonged interaction between waves and mangrove vegetation. Mangroves enhance wave dissipation, as indicated by the increased reduction in wave height represented by the green and pink dashed lines compared to cases without mangroves.

A.4. Variables included in conceptual guideline

Table A.1: Variables included in the conceptual guideline

Category	Variable	Units
Ecological variables	Forest width	Meters: Measured from the coast inland, representing the distance waves and surge travel through the mangroves
	Mangrove biomass	Megagrams per hectare (Mg/ha): Above-ground biomass per unit area, representing structural complexity and forest density
	Species zonation	Categorical: Distribution of mangrove species across the shore profile
Geomorphological variables	Coastal slope	Ratio
	Presence of channels and ponds	Binary (present/absent)
Hydrodynamic variables	Surge height	Meters: Maximum height of the storm surge
	Forward speed of the tropical storm	Meters per second: Speed of storm propagation
	Short wave height	Meters: Distance between the crest and the trough of wind waves
	Short wave period	Seconds: Time interval between successive wave crests
	Water depth	Meters: Depth of the water during the storm

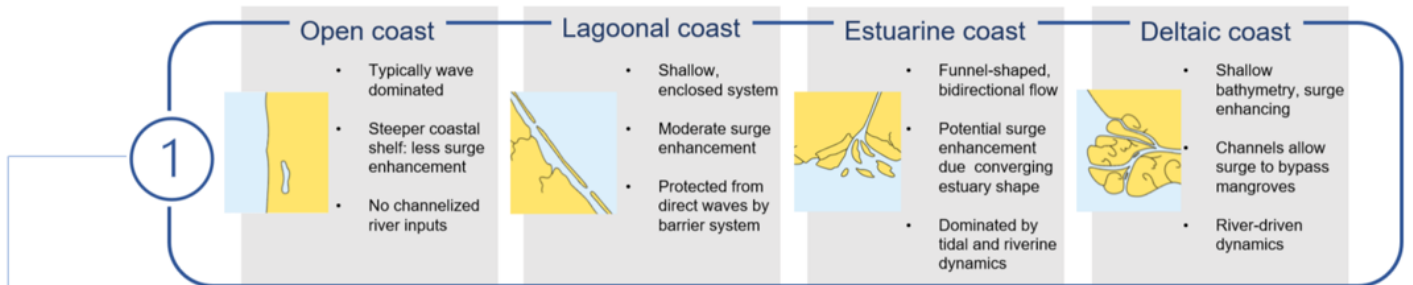
A.5. Conceptual guideline

Step 0: Identify the flood extent

What is the spatial extent of the flood caused by the tropical storm?

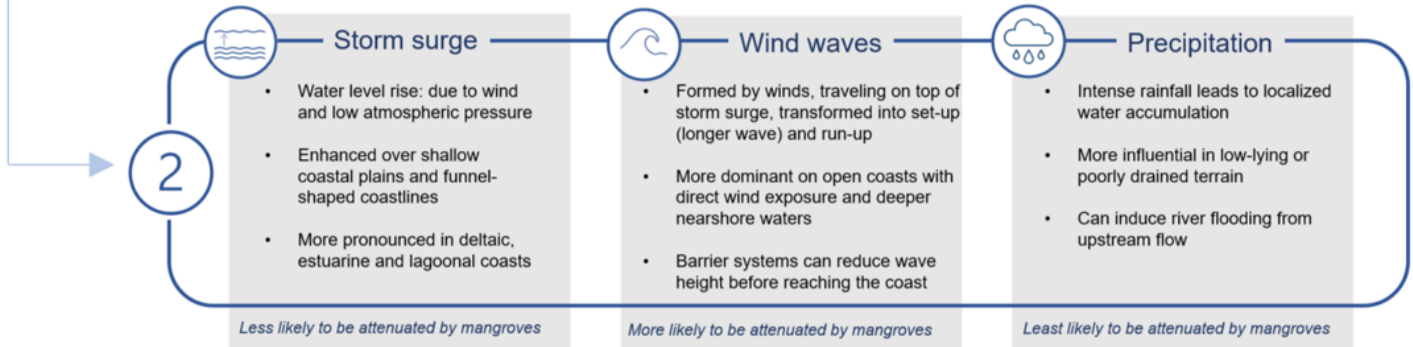
Step 1: Identify the mangrove coastal type

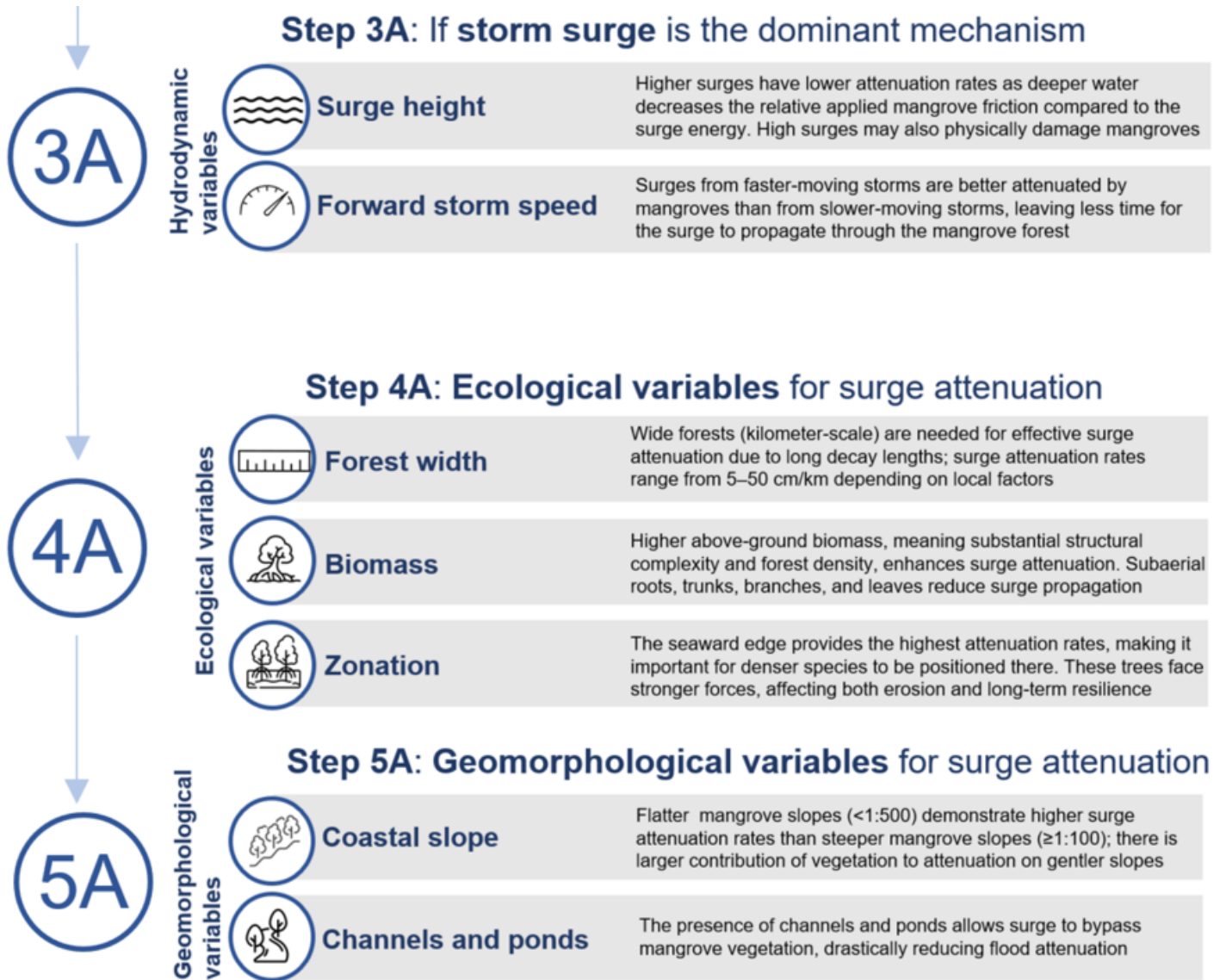
What is the coastal type where the mangrove forest is located?



Step 2: Determine the dominant hydrodynamic forcing

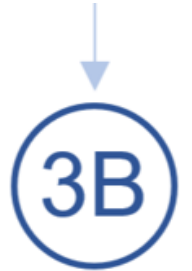
Which hydrodynamic forcing contributes most to flood extent during a tropical storm at this location?





Step 3B: If wind waves are the dominant mechanism

Hydrodynamic variables	 Wave height	Larger incoming wave heights experience higher attenuation rates than smaller incoming wave heights
	 Wave period	Short-period waves (~20 s) are attenuated more effectively by mangroves than longer-period waves
	 Water depth	Attenuation lowers with higher water depth, as the energy-dissipating parts of mangroves (the roots), occupy a relatively smaller part of the water column, reducing overall wave energy dissipation



Step 4B: Ecological variables for wave attenuation

Ecological variables	 Forest width	Forest widths of at least 500 meters are required for a 75% reduction of short wave energy, regardless of other variables. For narrower widths, attenuation depends on other factors involved
	 Biomass	Higher above-ground biomass raises wave attenuation rates due to high forest density and structural complexity. Forests with extensive prop roots, branches, and stems provide greater dissipation
	 Zonation	Wave energy is most effectively attenuated at the seaward forest edge. Dense species being located seaward is beneficial for attenuation rates and for sediment stabilization



Step 5B: Geomorphological variables for wave attenuation

Geomorphological variables	 Coastal slope	Mild slopes (1:80–1:40) allow for more wave attenuation by mangroves, showing exponential decay, compared to more gradual, lower reduction on steeper slopes (1:10)
	 Channels and ponds	Unlike with surge, the presence of channels and ponds does not substantially impact short wave attenuation



B

Additional remote sensing information

Remote sensing refers to the process of gathering information on objects or areas from a distance, typically using satellites, aircrafts, or drones. In principal, it involves detecting and measuring radiation reflected or emitted from the Earth's surface. This can be analysed to reveal characteristics of the detected object, such as land cover, temperature or vegetation health. Remote sensing offers advantages such as the ability to acquire data over large areas, providing detailed information on a global scale. This makes remote sensing an effective tool for applications as water monitoring (J. Li et al., 2022b). In general, remote sensing can be divided into passive and active remote sensing. The main example of a passive form of remote sensing is optical remote sensing and for active remote sensing, radar remote sensing is the most common.

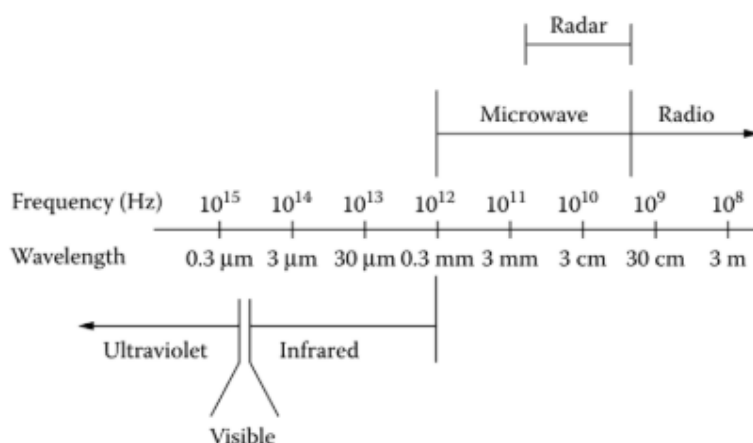


Figure B.1: The electromagnetic (EM) spectrum, showing the range of wavelengths and frequencies used in remote sensing. Optical remote sensing relies on visible (RGB), near-infrared (NIR), and shortwave infrared (SWIR) regions, while active radar operates in the microwave range (Cracknell, 2007).

B.1. Optical remote sensing

Optical remote sensing uses sunlight reflected from the Earth's surface to collect data, as shown in Figure B.2 (Cracknell, 2007). Optical remote sensing can detect the visible (RGB), near infrared (NIR) and shortwave infrared (SWIR) parts of the EM spectrum, shown in Figure B.1. These spectral bands, which refers to a specific range of wavelengths within the EM spectrum that is detected or measured by a sensor, allow for the observation of various surface features (Cracknell, 2007). When sunlight hits the Earth's surface, different features (like vegetation, water bodies, and landforms) reflect and absorb light differently depending on their material properties. Satellites equipped with optical sensors detect these variations in reflected radiation, which can be processed to create images made up of pixels. Optical remote sensing platforms, like satellites (e.g., Sentinel-2, Landsat), provide raster images that consist of pixels, with each pixel containing reflectance data from multiple spectral bands. The precision and detail of these images are contingent upon the spatial, spectral, and temporal resolutions of the

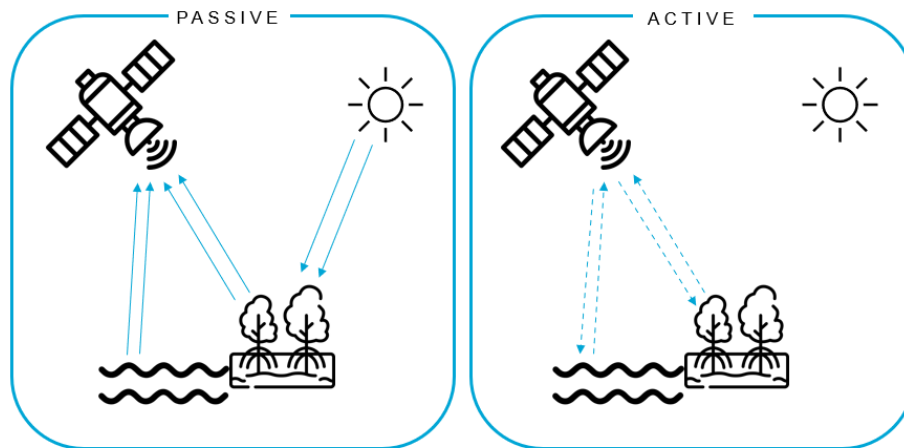


Figure B.2: Illustration of the difference between passive (a) and active (b) remote sensing. Passive sensors detect reflected sunlight. Active sensors emit their own signals and detect the backscattered response, allowing them to operate independently of sunlight and cloud cover, including during nighttime.

sensor, with compromises between the level of detail, the scope of coverage, and the frequency of observations.

B.2. Radar remote sensing

Radar remote sensing represents an active form of remote sensing, as shown in Figure B.2, whereby microwave signals (electromagnetic radiation), depicted in Figure B.1, are emitted and subsequently reflected from the Earth's surface (Ottinger & Kuenzer, 2020). In contrast to passive systems depending on sunlight, radar is capable of functioning independently of lighting conditions and can penetrate clouds (Cracknell, 2007). As the signals reach the surface, they are reflected back to the sensor, which is known as backscatter. The level of backscatter is influenced by the moisture content and the roughness of an object. Areas with a higher moisture content and greater surface roughness will result in a stronger backscatter signal. These variations in backscatter intensity can be measured, allowing features on Earth, such as water bodies, to be identified. The ability to detect differences in surface characteristics, regardless of weather and light conditions, makes radar an essential tool for this research.

Given its ability to operate independently of sunlight and cloud cover, radar remote sensing, specifically Synthetic Aperture Radar (SAR), offers strong potential for flood monitoring following tropical storms. SAR systems operate across different frequency bands, most notably X-band, C-band, and L-band, each with distinct wavelengths: X-band has the shortest wavelength, followed by C-band, and L-band has the longest (Ottinger & Kuenzer, 2020). As illustrated in Figure B.3, this results in different canopy penetration capabilities. For example, shorter wavelengths like C-band may not fully penetrate dense vegetation canopies, which limits their ability to detect surface water beneath forests (Ottinger & Kuenzer, 2020). Furthermore, SAR systems can transmit and receive signals in different polarizations (vertical or horizontal) resulting in polarization combinations such as VV, VH, HV, or HH (Ottinger & Kuenzer, 2020). Among the SAR frequency bands, the C-band is the one that is freely accessible, provided by the European Copernicus program through the Sentinel-1 mission. C-band SAR is widely used in the literature to detect floods in coastal regions (Ottinger & Kuenzer, 2020).

Figure B.4 illustrates how backscatter responses differ across land surface types. In areas with no or very low vegetation (shown in the two bottom rows), surface water creates a smooth surface that reflects radar energy away from the sensor, resulting in reduced backscatter (Ottinger & Kuenzer, 2020). Drops in backscatter intensity compared to pre-event conditions may indicate flooding. However, in densely vegetated areas such as mangrove forests, C-band radar signals often cannot penetrate the canopy (such as in subfigure a in Figure B.4), meaning that flooding beneath dense tree cover may not result in any change at all in backscatter compared to the dry state (Zhang et al., 2018). Conversely, in less densely tall vegetated forest the presence of water can actually increase backscatter through a

double-bounce effect, like in Figure B.4c (Zhang et al., 2018).

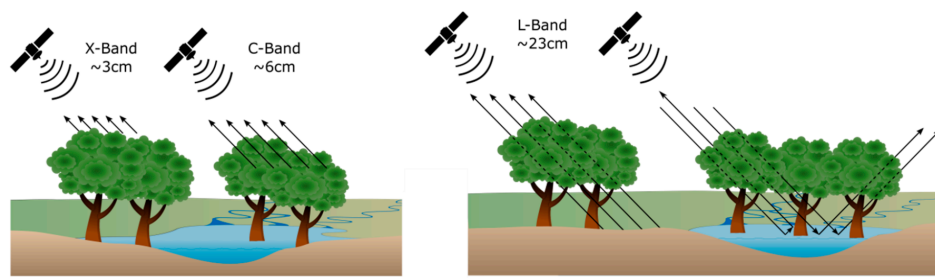


Figure B.3: Illustration of Synthetic Aperture Radar (SAR) wavelength bands (X, C, and L), highlighting how varying wavelengths penetrate vegetation to different extents, thereby influencing the ability to detect surface water beneath forest canopies (Ottinger & Kuenzer, 2020)

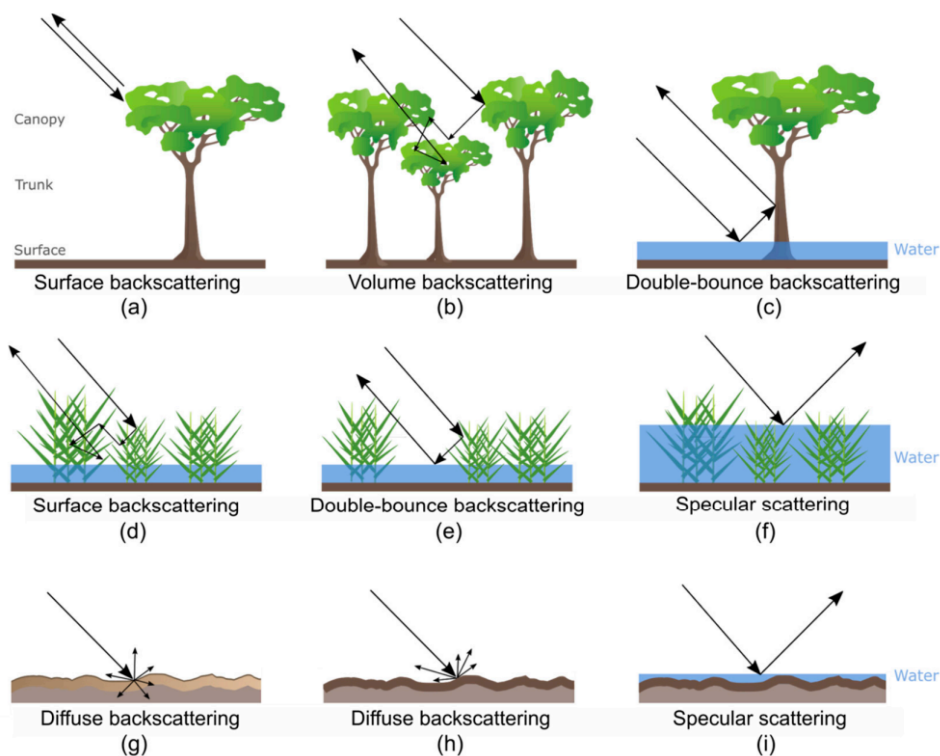


Figure B.4: Overview of radar backscattering mechanisms across varying surface types and inundation levels, illustrating how vegetation height and surface water influence backscatter signals (Ottinger & Kuenzer, 2020)

B.3. Sentinel-1 mission

Sentinel-1 is part of the Copernicus Programme, an initiative of the European Space Agency (ESA) and the European Commission (EC) (SentiWiki, 2024). The Sentinel-1A satellite was brought in orbit in 2014, followed by Sentinel-1B in 2016, forming a two-satellite constellation (SentiWiki, 2024). Each satellite follows a 12-day repeat cycle, when both satellites were in orbit, their phased orbits provided an effective 6-day repeat cycle at the equator, with shorter revisit times at higher latitudes due to orbital overlap, as shown in Figure B.5. However, following the end of the mission of Sentinel-1B in 2021, only Sentinel-1A remains operational, resulting in a 12-day repeat cycle globally, as shown in Figure B.6, though coverage remains more frequent at higher latitudes (SentiWiki, 2024). Among the four available imaging modes of Sentinel-1, the Interferometric Wide (IW) swath mode is the primary acquisition mode for land observations and is used for flood mapping in this study (SentiWiki, 2024). IW mode captures data with a spatial resolution of 5 m by 20 m and a 250 km swath width, balancing high-resolution imaging with broad spatial coverage (SentiWiki, 2024).

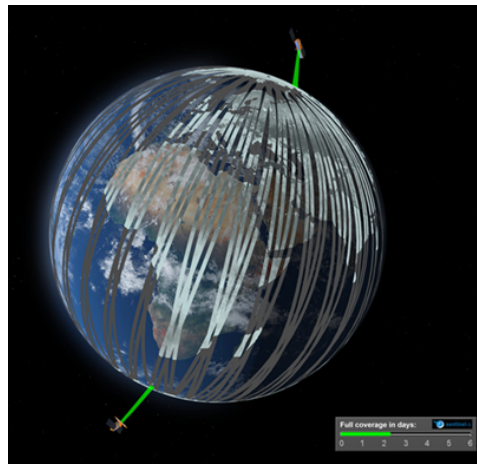


Figure B.5: Sentinel-1 constellation when both Sentinel-1A and Sentinel-1B were in orbit, which a combined repeat cycle of 6 days. Following the decommissioning of Sentinel-1B in 2021, only Sentinel-1A remains, resulting in a 12-day repeat cycle globally, with more frequent observations in high-latitude regions due to overlap (SentiWiki, 2024).

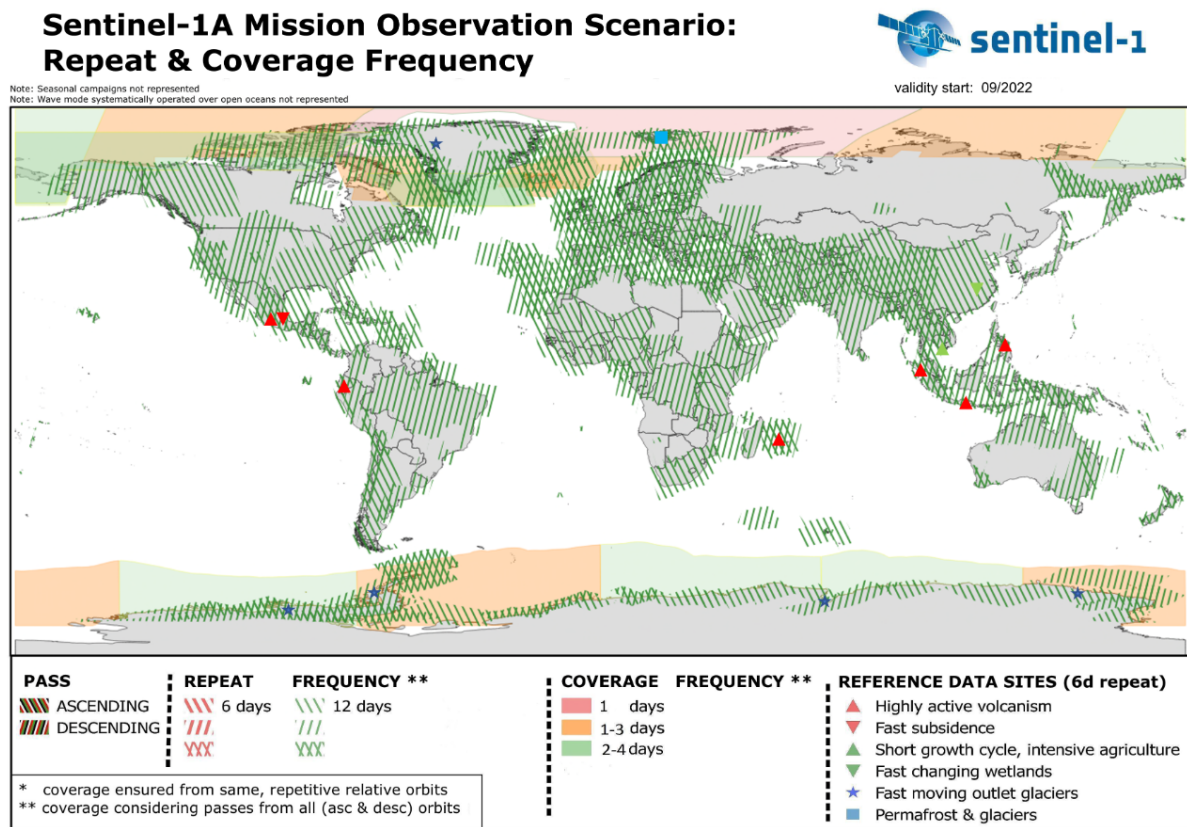


Figure B.6: Sentinel-1 observation scenario showing pass direction and revisit frequency since the decommissioning of Sentinel-1B in 2021. The map highlights the global coverage pattern, with a 12-day repeat cycle at the equator and increased repeat cycles at higher latitudes (SentiWiki, 2024)

B.4. Observable metrics of variables

To explore the potential of remote sensing in assessing flood extent and the possible attenuation effects of mangroves, it is evaluated whether the variables identified in the guideline can be detected through observable metrics. An explanation of these variables, along with their corresponding remote sensing metrics and references, is presented in this section and summarized in Table B.1. This suggests that many of the variables can be detected through remote sensing.

Table B.1: Variables, their observable metrics, and literature sources.

Variable (units)	Observable metric	Literature reference
Flooded area (m²)	<p><u>Optical</u>: Change detection with NDWI, where flood extent is the difference between pre- and post-event water maps. (# pixels where $NDWI > 0.2$ and $NDWI_{post} - NDWI_{pre} > 0$).</p> <p><u>Radar</u>: Change detection using SAR, where flood extent is mapped as # pixels where post-event backscatter is at least 1.35 times lower than pre-event backscatter. ($\sigma_{post}^0 / \sigma_{pre}^0 > 1.35$).</p>	UN-SPIDER, 2025, EOS Data Analytics, 2023, Uddin et al., 2019, J. Li et al., 2022b, Psomidis et al., 2020
Mangrove forest width (m)	Distance inland from the shoreline, based on # pixels where $NDVI > 0.3$.	Giri, 2021, Tran et al., 2022
Mangrove biomass (Mg/ha)	Biomass = $f(\text{canopy height})$; empirical relation used to link biomass and canopy height, which is detected with airborne LiDAR	Pham et al., 2019; Simard et al., 2019; Simard et al., 2006
Species zonation (Categorical)	Classification of species zones using optical data and NDVI, combined with machine learning algorithms	Febrianto et al., 2025; Pham et al., 2019
Water depth (m)	<u>Bathtub model</u> : Water depth calculated as $H_{depth} = H_w - H_{DEM}$. With water bodies detected using either optical or radar imagery.	Samuele et al., 2022, Kundu et al., 2022

(Table continues on next page)

(Table continued from previous page)

Variable (units)	Observable metric	Literature reference
Surge height (m)	Measured using satellite altimetry, which detects sea surface height anomalies before and after a storm, with surge height calculated as $H_{\text{surge}} = H_{\text{SSHA, post-storm}} - H_{\text{SSHA, pre-storm}}$.	X. Li et al., 2023, Ji and Li, 2020
Forward speed of storm (m/s)	Tracking temporal changes in surge height by analyzing multiple satellite acquisitions over time, determining how long elevated water levels persist.	X. Li et al., 2023, Ji and Li, 2020
Wave height (m)	Derived from SAR image spectra using the azimuth cut-off wavelength (λ_{co}) and dominant wavelength (λ_p), based on: $H_s = C \frac{0.3608}{\beta \sqrt{8} \sqrt{\tanh(2\pi d / \lambda_p)}} \lambda_{co} \sqrt{\lambda_p}$.	Pramudya et al., 2021
Wave period (s)	Estimated using satellite altimetry-derived significant wave height H_s , gradient and standard deviation of H_s as input for a deep neural network.	Wang et al., 2021
Presence of channels (Binary)	Identified as permanent small water bodies where NDWI > 0.3 in a majority of images in a multi-temporal Sentinel-2 time series.	Pena-Regueiro et al., 2020
Coastal slope (m/m)	Computed from DEM data as slope = $\frac{\Delta h}{\Delta x}$, where Δh is the elevation change and Δx is the horizontal distance.	A. Nelson et al., 2009

Variable: Flooded area (m²)

Flood extent mapping using remote sensing relies on optical and radar imagery (J. Li et al., 2022b). While optical data offers high spatial and spectral resolution, it is often hindered by cloud cover, making SAR an alternative option during tropical storms. Machine learning techniques, such as support vector machines and random forests, further enhance classification accuracy (Halder & Bandyopadhyay, 2022). Psomiadis et al. (2020) found that integrating both SAR and optical data improves flood mapping accuracy, with thresholding and index-based methods proving effective. However, high temporal resolution is needed to capture peak flooding. Uddin et al. (2019) demonstrated that Sentinel-1 SAR achieves 96.44% accuracy for rapid flood mapping when combined with pre-event Landsat 8 imagery. Their method proved effective in data-scarce regions, highlighting the benefits of cloud-based platforms like Google Earth Engine (GEE).

An accessible radar flood mapping methodology is one developed by the United Nations Platform for Space-based Information for Disaster Management and Emergency Response (UN-SPIDER) (UN-SPIDER, 2025). This approach utilizes Sentinel-1 SAR data in Google Earth Engine (GEE) to perform change detection by comparing pre- and post-event images. The method calculates a difference raster, where each pixel represents the degree of backscatter change over time, with high values meaning large change (typically corresponding to flooding) while low values represent minimal change (UN-SPIDER, 2025). A threshold of 1.35, found by trial and error, is utilized to classify flooded pixels and produce a binary flood map (UN-SPIDER, 2025).

For optical flood mapping, the Normalized Difference Water Index (NDWI) is widely used to detect surface water (J. Li et al., 2022b). NDWI is computed as (EOS Data Analytics, 2023):

$$\text{NDWI} = \frac{\text{Green} - \text{NIR}}{\text{Green} + \text{NIR}} \quad (\text{B.1})$$

In which 'Green' represents the reflectance in the green spectral band, which enhances the contrast between water and land, and 'NIR' (Near-Infrared) is the reflectance in the near-infrared band, which water strongly absorbs.

According to EOS Data Analytics (2023), NDWI values above 0.2 can be seen as water. Thus, a threshold of NDWI > 0.2 is commonly applied in flood studies to delineate inundated areas.

Variable: Mangrove forest width (m)

Mangrove forest width can be determined by mapping mangrove extent and measuring the inland distance from the shoreline using spatial analysis tools. Giri (2021) highlighted that mangroves exhibit distinct spectral signatures in the visible red, near-infrared (NIR), and mid-infrared bands, enabling their detection through remote sensing.

One of the most widely used approaches for mangrove extent detection is the Normalized Difference Vegetation Index (NDVI), which leverages differences in vegetation reflectance properties (Tran et al., 2022). NDVI is calculated as (Tran et al., 2022):

$$\text{NDVI} = \frac{\text{NIR} - \text{Red}}{\text{NIR} + \text{Red}} \quad (\text{B.2})$$

In which 'NIR' represents the near-infrared reflectance, which is strongly reflected by vegetation, and 'Red' is the visible red reflectance, which is absorbed by chlorophyll.

Tran et al. (2022) reported that 82% of mangrove mapping studies utilize NDVI, with a threshold of NDVI > 0.3 achieving an accuracy of 83% for mangrove classification. Beyond, machine learning techniques are increasingly being applied, with Random Forest classifiers demonstrating over 92% accuracy in mangrove extent detection (Tran et al., 2022).

Variable: Mangrove above-ground biomass (Mg/ha)

Biomass can be mapped using remote sensing, as demonstrated by Simard et al. (2006), who estimated canopy height from airborne LiDAR and DEM data, and applied an empirical relationship between canopy height and biomass. More recent studies, such as Pham et al. (2019), highlight a wider

range of approaches, including the use of optical and radar data combined through machine learning techniques. These methods incorporate vegetation indices, backscatter coefficient extraction, and InSAR for improved biomass estimation (Pham et al., 2019).

Variable: Zonation

Zonation refers to the spatial distribution of mangrove species and biomass. In terms of species mapping, Pham et al. (2019) outlined several remote sensing approaches, highlighting the potential of machine learning techniques to overcome limitations of traditional methods. Febrianto et al. (2025) demonstrated the effectiveness of Sentinel-2 imagery for mangrove species classification using Support Vector Machines (SVM) and Random Forest (RF) algorithms, with NDVI identified as a useful metric for estimating mangrove density.

Variable: Water depth (m)

Radar and optical imagery in combination with digital elevation models (DEMs) or digital terrain models (DTMs) can be used to derive water depth with remote sensing. Samuele et al. (2022) used Sentinel-1 SAR data combined with a DTM to detect flood depth. Their methodology involved comparing pre- and post-event Sentinel-1 images and applying the Otsu thresholding approach for water detection (Samuele et al., 2022). Similarly, Kundu et al. (2022) used remote sensing techniques for water depth estimation during Hurricane Harvey. Their study integrated SAR backscatter analysis from Sentinel-1 with LiDAR-derived DEMs and aerial imagery.

Variable: Surge height (m)

Satellite altimeters are used to measure storm surge height, complementing tide gauge data (X. Li et al., 2023). X. Li et al. (2023) demonstrated that modern satellite altimetry, with improved spatial and temporal resolution, enhances surge monitoring. Their study applied altimetric data for typhoons in China. Satellite altimeters measure sea surface height anomalies (SSHA), where surge height is calculated as the difference between pre-storm and post-storm SSHA values:

$$H_{\text{surge}} = H_{\text{SSHA, post-storm}} - H_{\text{SSHA, pre-storm}} \quad (\text{B.3})$$

Where H_{SSHA} represents the Sea Surface Height Anomaly (m), measured along satellite ground tracks. The difference between pre-storm and post-storm SSHA indicates the surge height, as it reflects the deviation of the sea surface from the mean sea level caused by the storm. These estimates are typically validated against tide gauge measurements.

Despite its potential, Ji and Li (2020) noted that a major limitation of satellite altimetry for surge height estimation is its uneven spatial coverage, which does not always align well with the spatial extent of storm surge.

Variable: Forward storm speed (m/s)

Unlike tide gauges, which provide real-time water level data, satellites capture discrete snapshots, limiting its ability to monitor the full time progression of a surge event. The temporal resolution of most satellite missions is insufficient for direct surge duration measurement. For instance, Sentinel-1 revisits every 6 to 12 days (SentiWiki, 2024). Given that storm surges typically last only a few hours to a day, these revisit intervals do not align with the timescales required for precise duration estimation.

An alternative approach is to perform flood mapping over time, effectively analyzing surge height at different time steps, as discussed in the previous section. By comparing surge height across multiple images, it could be possible to estimate how long surge persists in an area. However, this method does not directly capture the duration of peak storm surge but rather the presence of flooding over time.

Variable: Wave height (m)

Synthetic Aperture Radar (SAR) has been used for wave height estimation (Pramudya et al., 2021). Pramudya et al. (2021) derived significant wave height (H_s) from Sentinel-1 SAR and validated it against buoy data in Hawaii and the U.S. West Coast. Their approach utilized the azimuth cut-off wavelength (λ_{co}) and the dominant wavelength (λ_p), which were both extracted from SAR image spectra (Pramudya et al., 2021). The significant wave height was then computed as:

$$H_s = C \frac{0.3608}{\beta \sqrt{8} \sqrt{\tanh(2\pi d / \lambda_p)}} \lambda_{co} \sqrt{\lambda_p} \quad (\text{B.4})$$

where C is a calibration constant, d is the water depth, and β is an empirical correction factor. The dominant wavelength (λ_p) is determined from spectral analysis of SAR images, while the azimuth cut-off wavelength (λ_{co}) is taken from how waves affect the motion of the satellite's radar signal (Pramudya et al., 2021).

Moreover, machine learning is increasingly explored for wave height retrieval, showing promise for improved accuracy Amani et al. (2022).

Variable: Wave period (s)

Wave period has traditionally been measured using in situ ocean buoys. However, buoy networks are spatially limited, predominantly located in the Northern Hemisphere, leaving large gaps in global wave period observations (Wang et al., 2021). Remote sensing, particularly satellite altimetry, offers an alternative. While altimetry can directly measure wave height it does not inherently retrieve wave period (Wang et al., 2021). Wang et al. (2021) developed a deep learning approach using a neural network to estimate mean wave period from satellite altimeter data. Their model utilizes significant wave height H_s , the gradient of H_s , and the standard deviation of H_s as input parameters, demonstrating agreement with buoy measurements (Wang et al., 2021).

Variable: Presence of channels (binary)

Detecting the presence of channels and ponds in mangrove forests involves identifying small permanent water bodies using remote sensing techniques. Pena-Regueiro et al. (2020) demonstrated that Sentinel-2 imagery effectively maps small water bodies in wetland environments, applicable to mangrove ecosystems. Their study, which tested Sentinel-2 across various locations and dates, identified the NDWI as the most reliable index for water body detection (Pena-Regueiro et al., 2020). The study found that an NDWI threshold of 0.30 yielded the highest accuracy (0.89), outperforming other indices, which achieved a maximum accuracy of 0.85 (Pena-Regueiro et al., 2020). Given that channels are typically more permanent features, a multi-temporal approach enhances detection reliability. By stacking images over longer timeframes, inconsistencies can be minimized.

Variable: Coastal slope (m/m)

Coastal slope can be effectively derived from remote sensing data using digital elevation models (DEMs). DEMs provide elevation data across large spatial extents and can be generated using aerial photogrammetry, LiDAR, and radar-based interferometry (A. Nelson et al., 2009).

Publicly available DEM products provide solutions for coastal slope estimation. These datasets are widely integrated into GEE, where slope can be computed using the gradient of elevation values over distance:

$$\text{Slope} = \frac{\Delta h}{\Delta x}$$

Where Δh is the elevation change and Δx is the horizontal distance.

B.5. Stepwise explanation of methodological flowchart

The following steps provide a detailed, step-by-step explanation of the methodological framework presented. Each step corresponds to a specific component of the framework and outlines its implementation for mapping and refining flood extent following a tropical storm, incorporating variables relevant to mangrove–flood interactions.

1. Area selection

First, an Area of Interest (AOI) is defined, representing the geographic region where flood detection will be performed. This region is used to spatially constrain all further analyses.

2. Date selection

The date of landfall of the tropical storm is specified to determine the appropriate temporal window for satellite imagery. For the post-storm image, a short date range, ideally within 6 days after the event, is selected, corresponding to the Sentinel-1 satellite's repeat cycle. For the pre-storm condition, rather than using a single image, a time stack of multiple images is selected from the same season, to ensure seasonal consistency and minimize variation due to vegetation changes. An average backscatter composite is computed over this stack to reduce the speckle noise inherent in radar imagery, caused by interference of multiple radar returns, which often appears as a grainy "salt-and-pepper" texture.

3. Polarization setting

The appropriate radar polarization is chosen, either VV (vertical transmit and vertical receive) or VH (vertical transmit and horizontal receive). VV polarization tends to be more sensitive to smooth surfaces such as open water, whereas VH polarization is generally more effective in detecting surface changes in vegetated or forested areas. The optimal choice depends on the land cover characteristics of the study area and should ideally be evaluated per case study.

4. Setting satellite pass direction

It must be selected whether the Sentinel-1 imagery is acquired from the ascending or descending satellite pass. Although both passes are available for each location, it is essential to use the same orbit direction for both the pre- and post-event imagery. This is because differences in viewing angles between orbits may affect the backscatter signal and thereby influence flood detection outcomes, potentially introducing inconsistencies.

5. Image pre-processing

Once all parameters have been set, the imagery is automatically preprocessed by Google Earth Engine. The following preprocessing steps are applied by default (Google Earth Engine, 2025):

- *Apply-orbit-file*: updates the metadata of the satellite orbit.
- *Border noise removal*: removes low-intensity noise and invalid data along the edges of Ground Range Detected (GRD) image footprints.
- *Thermal noise removal*: reduces discrepancies between sub-swaths.
- *Radiometric calibration*: computes the backscatter intensity using sensor calibration parameters.
- *Terrain correction*: uses the Shuttle Radar Topography Mission (SRTM) 30 m digital elevation model to account for topographic variation.
- *Logarithmic transformation*: converts the backscatter coefficient (σ^0) into decibel (dB) scale.

Additionally, one manual preprocessing step is applied:

- *Smoothing*: a focal mean filter is applied to reduce speckle noise. The smoothing is performed over a user-defined radius, depending on the spatial scale of the study.

6. Setting the change detection threshold

The change detection method is a widely adopted approach for flood mapping (Hamidi et al., 2023; Vanama et al., 2021). In this tool, flooding is detected based on the change in backscatter between a pre-event time stack and a single post-event image.

The method begins by calculating the ratio of change for each pixel: the backscatter coefficient of the post-storm image is divided by the mean backscatter coefficient of the pre-event time stack. This produces a raster in which each pixel represents the ratio of backscatter change.

A threshold is then applied to this change raster. This threshold must be adjusted depending on the study location, as a higher threshold is more conservative, detecting fewer flooded pixels but also reducing false positives, while a lower threshold is more sensitive but may include more false detections.

Once the threshold is applied, a binary flood map is generated in which all pixels with a change ratio above the threshold are classified as flooded (value = 1), and all others as not flooded (value = 0). The calculation is formalized below (Vanama et al., 2021):

$$RI = \frac{\sigma_{\text{after}}^0}{\sigma_{\text{before}}^0} \quad (\text{B.5})$$

$$\text{Flood Mask} = \begin{cases} 1 & \text{if } RI > T \\ 0 & \text{otherwise} \end{cases} \quad (\text{B.6})$$

Where:

RI	Ratio Image: The ratio of the post-flood to the pre-flood backscatter coefficient.
σ_{after}^0	Backscatter coefficient of the post-flood image.
σ_{before}^0	Mean backscatter coefficient of the pre-flood image time stack.
T	Threshold applied to the ratio image to classify flooded areas. Typically determined through trial and error (e.g., $T = 1.35$).
1	Pixel classified as flooded.
0	Pixel classified as not flooded.

Model refining and testing**1. Improving the flood extent layer**

After the threshold is applied, the resulting binary flood layer is refined using a set of post-processing steps to enhance the accuracy of the flood extent detection. These improvements are outlined as follows:

- **Removing permanent water bodies:**

To exclude areas that are permanently inundated and thus not associated with the storm-related flooding, the JRC Global Surface Water dataset is used. Specifically, areas where water is present for more than nine months per year are masked out from the flood extent layer.

- **Eliminating small isolated pixels:**

To reduce noise and remove falsely detected small patches, isolated pixels with fewer than a defined number of neighboring pixels are filtered out. The minimum number of connected neighboring pixels should be determined based on the characteristics of the study area.

2. Masking steep slopes:

Regions with slopes greater than five degrees are removed from the flood extent. It is unlikely that floodwaters would accumulate in such steep areas. Slope is calculated using the HydroSHEDS Digital Elevation Model (DEM), which is derived from the SRTM DEM at a resolution of 3 arc-seconds.

3. Calculating flooded area

From the flood extent map, the total flooded area is calculated by summing all pixels classified as flooded. Each pixel is multiplied by its surface area in square meters, based on the projection used. The resulting total area is then converted into hectares to provide a standardized and interpretable unit of measure for flood extent analysis.

4. Pre-storm date range tests

The time stack of pre-storm imagery can be evaluated for seasonality effects.

- Defining multiple pre-storm time ranges: one restricted to a single season, and one covering both rainy and dry seasons
- Applying the model to detect flood extents for both date ranges
- Comparing the results based on total flood extent and spatial distribution. The scenario limited to a single season is expected to perform better due to reduced backscatter variability

5. Dry season tests

Dry tests should be conducted during periods without known flooding events, covering both rainy and dry seasons. These tests help identify false positives.

- Selecting dates during both rainy and dry seasons across multiple years, ensuring that no major flooding was reported during those periods
- Running the model to detect flood extents
- Evaluate and compare the results in terms of flood area and spatial distribution
- If unexpectedly large flood extents are detected during dry-season periods, model parameters should be adjusted such as the threshold for change detection, smoothing radius, or the filter for removing small isolated pixels
- Areas consistently identified as flooded during dry-season tests in the dry season can be masked out, as such pixels are unreliable and may reduce model accuracy

6. Qualitative threshold sensitivity analysis

A sensitivity analysis can be conducted on the change detection threshold to refine model performance.

- Apply the model for several threshold values
- Compare outcomes based on total flood area and spatial distribution
- Compare the flood extents from the sensitivity analysis with published flood maps to select a threshold value that aligns best

Bathtub inundation flood map

The bathtub inundation model maps flood extent by overlaying a static water level on an elevation model, inundating all land below the set water level threshold (Kasmalkar et al., 2024; Sanders et al., 2024). Unlike process-based hydrodynamic models, it ignores key processes, often overestimating flood extent, by up to 200% (Sanders et al., 2024; Vousdoukas et al., 2016). It assumes all areas below the threshold flood regardless of hydraulic connectivity, it omits attenuation by friction (like mangroves), neglects water management systems including pumps, overlooks drainage, and does not account for multi-source flooding (Kasmalkar et al., 2024; Sanders et al., 2024). Despite these limitations, it remains widely used due to its simplicity and accessibility and is applied here purely as a comparative tool alongside SAR-derived flood extent. The bathtub inundation model is constructed as follows.

1. **Selection of the DEM:** The first step is to select an appropriate Digital Elevation Model (DEM) to represent surface elevation. A globally available DEM with sufficient spatial resolution (e.g., 30 m) and global coverage is ideal. DEMs are derived from interferometric synthetic aperture radar (InSAR), capturing elevation through phase differences between radar signals. These datasets operate in the microwave spectrum, enabling measurements even in cloudy or nighttime conditions.
2. **Pre-processing of elevation data:** DEMs may contain speckle noise due to radar-based data acquisition. A smoothing radius and connectivity filter are applied to reduce noise and remove small, isolated pixels.
3. **Setting the vertical reference level:** Ensuring compatibility between the DEM and floodwater height data requires alignment of vertical datums. For instance, if a DEM is referenced to mean sea level (MSL), but if another tidal datum is used (e.g., mean high water, MHW), adjustments must be made using local tide gauge data to align the water level and elevation references correctly.
4. **Determining the set water level threshold:** A water level threshold is selected to define inundation extent by marking all areas with elevations below this threshold as flooded. To account for spatial variability or uncertainty in flood height, multiple water level scenarios can be simulated, allowing for comparative analysis of potential inundation under different flood conditions.

Integration of EO datasets

1. Adding precipitation hotspot map

To assess the potential contribution of rainfall to the detected flood extent, a precipitation hotspot map can be added as a contextual layer.

- The CHIRPS daily precipitation dataset is used, offering global coverage at a spatial resolution of 0.05 degrees (approximately 5.5 km at the equator). It combines satellite-based infrared data with ground station observations.
- Daily precipitation values are summed over a user-defined number of days preceding the storm event to generate a cumulative rainfall map.
- A threshold can be applied to the cumulative map to identify areas of intense rainfall. The resulting hotspot map can then be overlaid with the SAR-derived flood extent to explore spatial correspondence between precipitation patterns and observed flooding.

2. Adding ecological variables

- *Mangrove extent layer*: The Global Mangrove Watch (GMW) dataset is used to provide global mangrove extent based on L-band SAR data. The dataset spans from 1996 to 2020 and has an overall mapping accuracy of 87.4% (Bunting et al., 2022). Version 3 of GMW is used, with a spatial resolution of 30 meters.
- *Mangrove biomass layer*: Above-ground biomass is assessed using the global biomass layer provided by Simard et al. (2019), which integrates SRTM digital elevation data and spaceborne LiDAR observations. The biomass layer has a spatial resolution of 30 meters.

3. Adding hydrodynamic variables

- *Storm track layer*: The storm track is obtained from the International Best Track Archive for Climate Stewardship (IBTrACS), developed under the World Meteorological Organization (WMO). This study uses version 4r01 (Gahtan et al., 2024), which provides global tropical cyclone track data and enables spatial visualization of storm trajectories across the study region.

4. Adding geomorphological variables

- *Channels and ponds presence layer*: The HydroATLAS v1.0 dataset is used to include hydrographic features. HydroRIVERS provides linear river networks at 500-meter (15 arc-second) resolution (Linke et al., 2019), while HydroLAKES provides polygon features of lakes at the same resolution (Lehner et al., 2022).
- *Land cover layer*: The National Land Cover Database (NLCD) provided by the U.S. Geological Survey (USGS) is used. It is derived from Landsat imagery with a spatial resolution of 30 meters. The most recent dataset from 2023 is used in this study (U.S. Geological Survey (USGS), 2024).

B.6. Earth Observation datasets in remote sensing tool

Table B.2: Overview of EO datasets used in the remote sensing tool.

Dataset	Spatial Resolution	Purpose
Sentinel-1 GRD (C-band SAR)	10 m	Flood extent detection using change detection of radar backscatter.
JRC Global Surface Water	30 m	Removal of permanent water bodies from the flood map.
HydroSHEDS DEM (SRTM)	3 arc-second (~90 m)	Derivation of slope to exclude steep areas unlikely to flood.
Global Mangrove Watch (GMW)	30 m	Mangrove extent layer mapped from L-band SAR.
Global Mangrove Biomass	30 m	Above-ground biomass layer of mangrove forests based on LiDAR and DEM data.
IBTrACS Storm Track (v4r01)	N/A	Tropical storm track to spatially link flood events with storm trajectories.
HydroATLAS: RIVERS	HydroR- 15 arc-second (~500 m)	River network data to assess presence of channels in mangrove area.
HydroATLAS: LAKES	Hydro- 15 arc-second (~500 m)	Lake network data to assess presence of ponds in mangrove area.
NLCD (National Land Cover Database)	Land 30 m	Land cover classification to contextualize flood impacts.
DeltaDTM	30 m	Used in bathtub inundation modelling based on elevation thresholds.
CHIRPS daily dataset	0.05° (~5.5 km)	Gridded precipitation dataset used for rainfall context in flood analysis.

Additional case study data

C.1. Case study maps

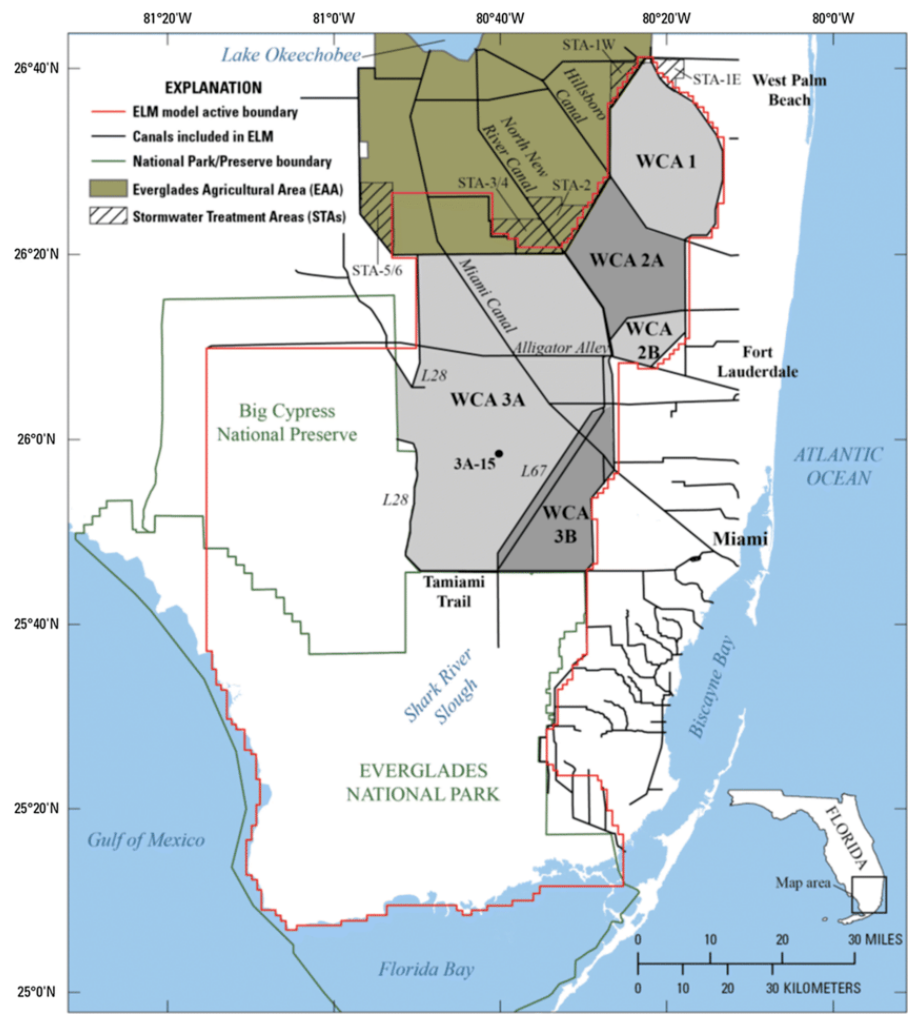


Figure C.1: Boundaries of the Everglades National Park, Water Conservation Area, and the Big Cypress National Preserve (Orem et al., 2020).

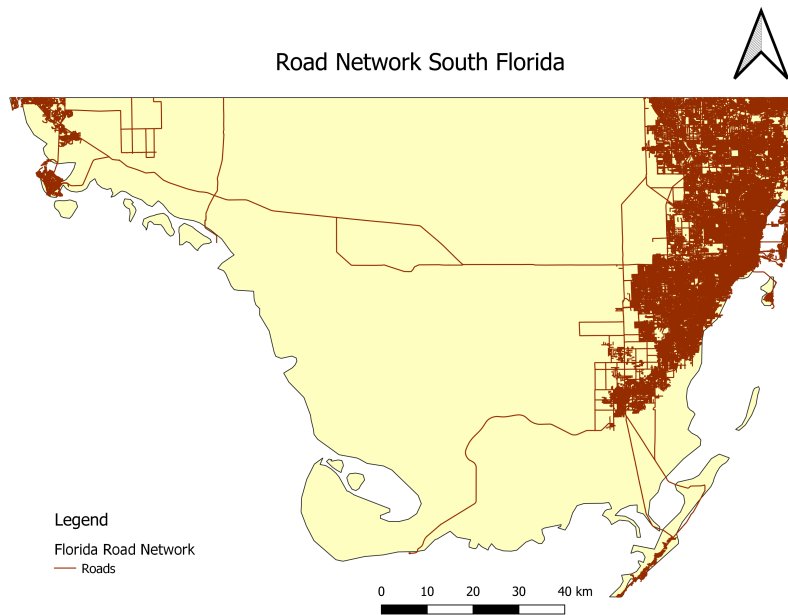


Figure C.2: Map showing the road network within the case study area (Meijer et al., 2018)

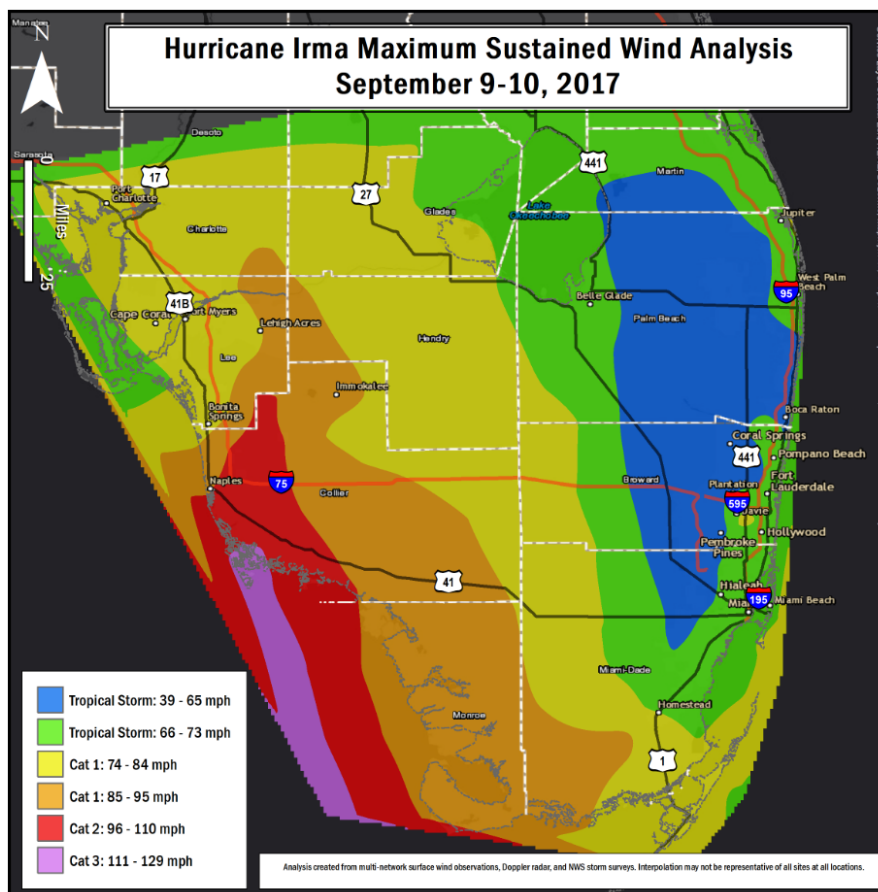


Figure C.3: Maximum sustained wind during Hurricane Irma across South Florida (National Weather Service, 2017). The map shows the storm's center and the surrounding area affected by varying wind speeds. Although the center did not cross most of the study area directly, the radius of intense winds contributed to winds, storm surge and inland flooding throughout.

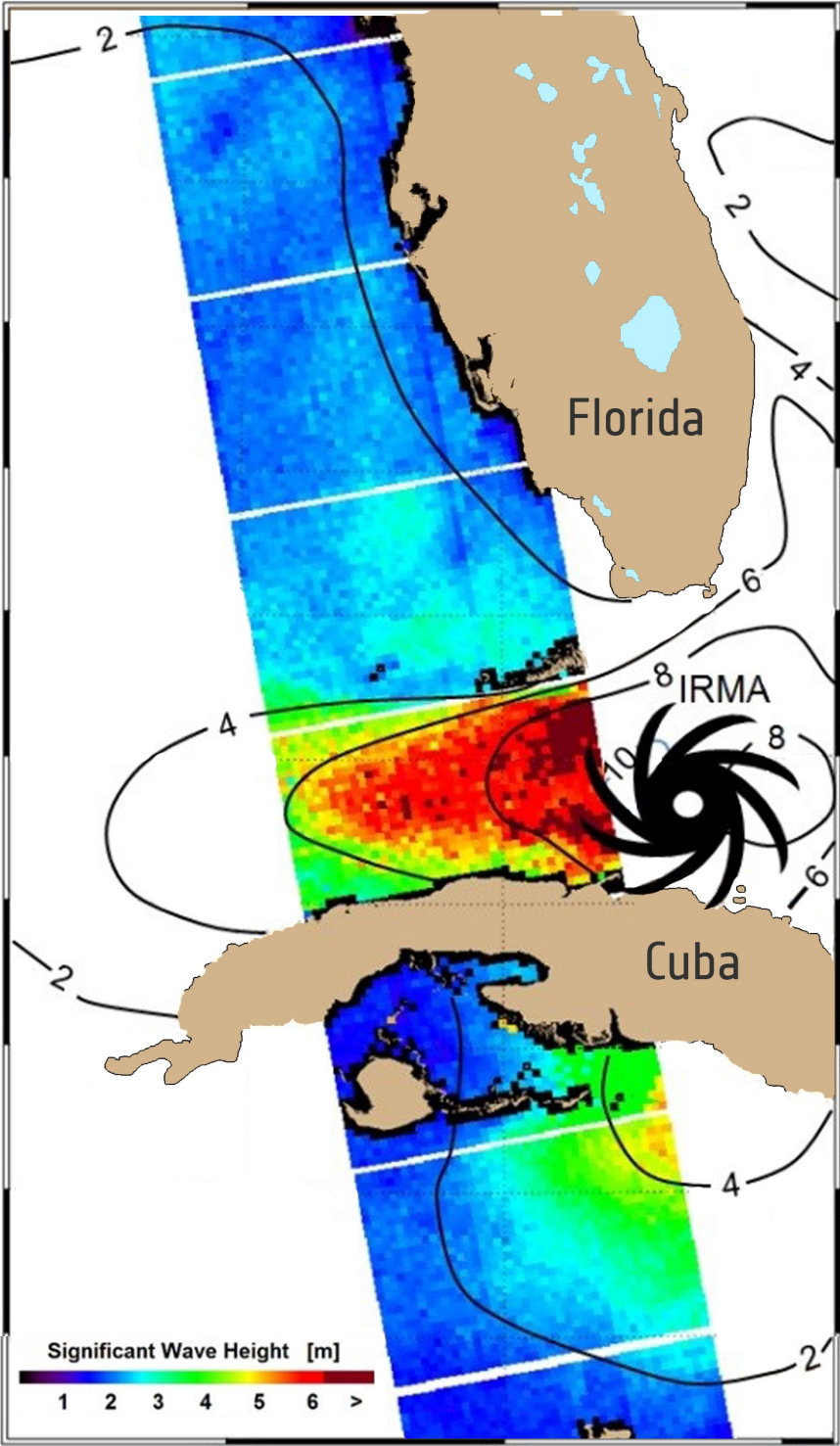


Figure C.4: Significant wave height during Hurricane Irma (September 10th, 2017), mapped by ESA (2017) using Sentinel-1 radar data.

C.2. Sentinel-1A SAR imagery footprints and information

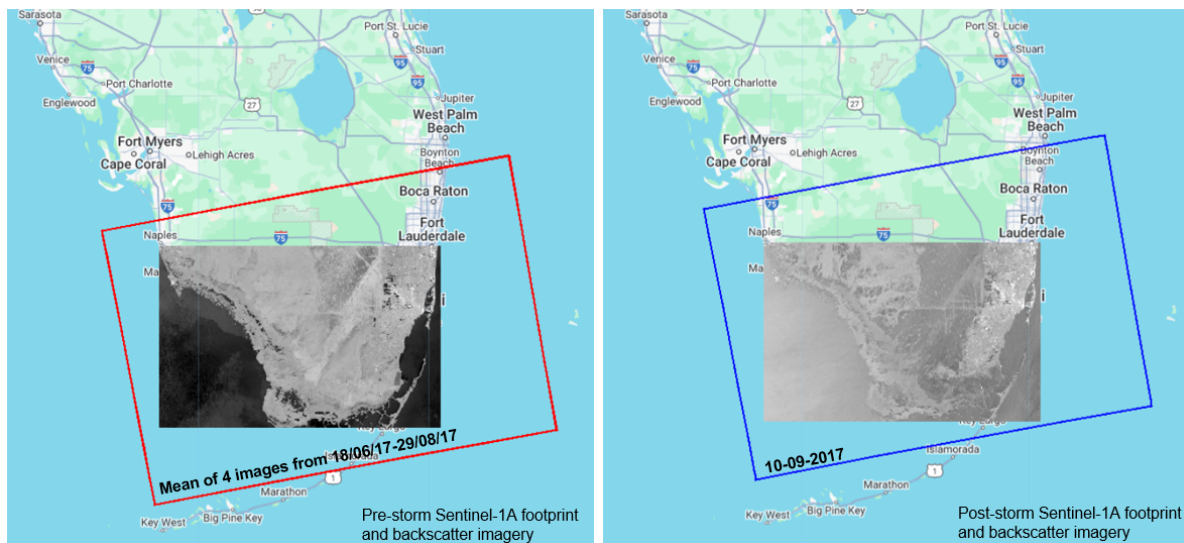


Figure C.5: Sentinel-1 SAR image footprints and backscatter imagery for pre- and post-flood conditions. The red (left) and blue (right) outlines indicate the footprints of the Sentinel-1 SAR image tiles used in the analysis. These footprints represent the spatial extent of individual image acquisitions. Within these footprints, the backscatter images are shown, clipped to the area of interest (AOI).

Table C.1: Sentinel-1 GRD imagery used for flood detection after Hurricane Irma.

Acquisition date	Image ID	Pre/Post Storm
2017-06-18	S1A_IW_GRDH_1SDV_20170618T232745	Pre-storm
2017-07-24	S1A_IW_GRDH_1SDV_20170724T232747	Pre-storm
2017-08-17	S1A_IW_GRDH_1SDV_20170817T232748	Pre-storm
2017-08-29	S1A_IW_GRDH_1SDV_20170829T232749	Pre-storm
2017-09-10	S1A_IW_GRDH_1SDV_20170910T232726	Post-storm
2017-09-10	S1A_IW_GRDH_1SDV_20170910T232751	Post-storm

Table C.2: Sentinel-1 GRD imagery used for pre-event time stack testing (same season).

Acquisition date	Image ID
2017-06-18	S1A_IW_GRDH_1SDV_20170618T232745
2017-07-24	S1A_IW_GRDH_1SDV_20170724T232747
2017-08-17	S1A_IW_GRDH_1SDV_20170817T232748
2017-08-29	S1A_IW_GRDH_1SDV_20170829T232749

Table C.3: Sentinel-1 GRD imagery used for pre-event time stack testing (mixed seasons).

Acquisition date	Image ID
2017-03-02	S1A_IW_GRDH_1SDV_20170302T232740
2017-03-26	S1A_IW_GRDH_1SDV_20170326T232740
2017-05-13	S1A_IW_GRDH_1SDV_20170513T232743
2017-06-18	S1A_IW_GRDH_1SDV_20170618T232745

Table C.4: Sentinel-1 GRD imagery IDs used for dry flood model tests (Part 1).

Test	Image ID
17-1 Pre	S1A_IW_GRDH_1SDV_20171004T232750
	S1A_IW_GRDH_1SDV_20171016T232750
	S1A_IW_GRDH_1SDV_20171028T232750
	S1A_IW_GRDH_1SDV_20171109T232750
17-1 Post	S1A_IW_GRDH_1SDV_20171208T233544
	S1A_IW_GRDH_1SDV_20171208T233609
	S1A_IW_GRDH_1SDV_20171215T232749
18-1 Pre	S1A_IW_GRDH_1SDV_20181104T232756
	S1A_IW_GRDH_1SDV_20181116T232756
	S1A_IW_GRDH_1SDV_20181128T232756
18-1 Post	S1A_IW_GRDH_1SDV_20181210T232755
19-1 Pre	S1A_IW_GRDH_1SDV_20191111T232803
	S1A_IW_GRDH_1SDV_20191123T232802
19-1 Post	S1A_IW_GRDH_1SDV_20191205T232802
	S1A_IW_GRDH_1SDV_20191210T233557
	S1A_IW_GRDH_1SDV_20191210T233622
17-2 Pre	S1A_IW_GRDH_1SDV_20171109T232750
	S1A_IW_GRDH_1SDV_20171121T232749
	S1A_IW_GRDH_1SDV_20171203T232749
	S1A_IW_GRDH_1SDV_20171215T232749
17-2 Post	S1A_IW_GRDH_1SDV_20180101T233543
	S1A_IW_GRDH_1SDV_20180101T233608
	S1A_IW_GRDH_1SDV_20180108T232748

Table C.5: Sentinel-1 GRD SAR image IDs used for dry flood model tests (Part 2).

Test	Image ID
18-2 Pre	S1A_IW_GRDH_1SDV_20181104T232756
	S1A_IW_GRDH_1SDV_20181116T232756
	S1A_IW_GRDH_1SDV_20181128T232756
	S1A_IW_GRDH_1SDV_20181210T232755
18-2 Post	S1A_IW_GRDH_1SDV_20190103T232754
19-2 Pre	S1A_IW_GRDH_1SDV_20191111T232803
	S1A_IW_GRDH_1SDV_20191123T232802
	S1A_IW_GRDH_1SDV_20191205T232802
	S1A_IW_GRDH_1SDV_20191217T232802
19-2 Post	S1A_IW_GRDH_1SDV_20191229T232801
	S1A_IW_GRDH_1SDV_20200103T233556
	S1A_IW_GRDH_1SDV_20200103T233621
19-3 Pre	S1A_IW_GRDH_1SDV_20190608T232756
	S1A_IW_GRDH_1SDV_20190620T232757
	S1A_IW_GRDH_1SDV_20190702T232758
	S1A_IW_GRDH_1SDV_20190714T232759
19-3 Post	S1A_IW_GRDH_1SDV_20190819T232801
17-4 Pre	S1A_IW_GRDH_1SDV_20170618T232745
17-4 Post	S1A_IW_GRDH_1SDV_20170717T233541
	S1A_IW_GRDH_1SDV_20170717T233606
	S1A_IW_GRDH_1SDV_20170724T232747
18-4 Pre	S1A_IW_GRDH_1SDV_20180613T232751
	S1A_IW_GRDH_1SDV_20180625T232752
18-4 Post	S1A_IW_GRDH_1SDV_20180719T232753
	S1A_IW_GRDH_1SDV_20180724T233548
	S1A_IW_GRDH_1SDV_20180724T233613
19-4 Pre	S1A_IW_GRDH_1SDV_20190608T232756
	S1A_IW_GRDH_1SDV_20190620T232757
19-4 Post	S1A_IW_GRDH_1SDV_20190719T233554
	S1A_IW_GRDH_1SDV_20190719T233619
	S1A_IW_GRDH_1SDV_20190726T232759